Using Lidar Technology and the STILT Model to Assess Air Pollution and Improve Estimates of Greenhouse Gas Emissions in Cities

Using Lidar Technology and the STILT Model to Assess Air Pollution and Improve Estimates of Greenhouse Gas Emissions in Cities

A dissertation presented

by

Yanina Débora Barrera

to

The School of Engineering and Applied Sciences

in partial fulfillment of the requirements

for the degree of

Doctor of Philosophy

in the subject of

Environmental Science and Engineering

Harvard University

Cambridge, Massachusetts

July 2019

Dissertation Advisor: Steven C. Wofsy Yanina Débora Barrera

Using Lidar Technology and the STILT Model to Assess Air Pollution and Improve Estimates of Greenhouse Gas Emissions in Cities

Abstract

Simulation of the planetary boundary layer (PBL) is key for forecasting air quality and estimating greenhouse gas (GHG) emissions in cities. Here, we conducted the first long-term and continuous study of PBL heights (PBLHs) in Boston MA, using a compact lidar (light detection and ranging) instrument. We developed an image recognition algorithm to estimate PBLHs from the lidar measurements and evaluated simulations of the PBL from eight numerical weather prediction (NWP) model versions, which showed different systematic errors and variability in simulating the PBLHs. The NWP model with the best overall agreement for the fully developed PBL had R^2= 0.72 and bias of only 0.128 kilometers (km). However, this model predicted a number of anomalously high carbon dioxide concentrations at ground stations, because it occasionally underestimated PBLH to a significant extent. We also developed a novel method that combines lidar data, vertical footprints from the Stochastic Time-Inverted Lagrangian Transport (STILT) model, and a high-resolution anthropogenic carbon dioxide (CO_2) emissions inventory to detect, identify, and estimate transboundary air pollution within the nocturnal residual layer (RL). Using our novel method, we identified 42 transboundary air pollution episodes within the nocturnal RL in Boston during a 5-month study period in 2014. A quantitative index for transboundary air pollution was obtained as mean pressure-weighted column CO_2 enhancements (ΔCO_2) contributions in Boston from northeastern states, as simulated by a high-resolution model. Results from this work were used to evaluate the

performance of models used to estimate air pollution and GHG fluxes. Such evaluation is critical to track progress on emission reduction targets and guide city, state, and regional policies.

Table of Contents

Acknowledgements

I would like to thank Thomas Nehrkorn, Jennifer Hegarty, Maryann Sargent, Joshua Benmergui, Elaine Gottlieb, Steven C. Wofsy, Phil DeCola, Lucy Hutyra, and Taylor Jones for their contributions to this work. I would like to thank engineers John Budney and Bruce Daube for their help maintaining the miniMPL network in Boston, Massachusetts, and Mineola, New York. This work was funded by the NASA Carbon Monitoring System (NASA NNX12AP10G and NASA NX12AM82G), the National Science Foundation (NSF) Collaborative Research Awards 1265614 and 1302902, the NSF Major Research Instrumentation Program (AGS-1337512), and the Environmental Defense Fund (1046-000000-10800).

List of Abbreviations

GHG	Greenhouse gases
CO_2	Carbon dioxide
CMS	NASA's Carbon Monitoring System
Lidar	Light detection and ranging technology
NRB	Normalized relative backscatter
miniMPL	Mini micropulse lidar
PBL	Planetary boundary layer
RL	Residual layer
PBLH	Planetary boundary layer height(s)
RLH	Residual layer height(s)
SVD	Singular value decomposition
FDG	First derivative Gaussian
NWP	Numerical weather prediction
WRF	Weather and Research Forecasting model
NAM	North American Mesoscale system
NARR	North American Regional Reanalysis product
GDAS	Global Data Assimilation System
LPDM	Lagrangian particle dispersion model
STILT	Stochastic Time-Inverted Lagrangian Transport model
HYPSLIT	Hybrid Single-Particle Lagrangian Integrated Trajectory model
ACES	Anthropogenic Carbon Emissions System

Chapter 1

Using image processing to estimate the planetary boundary layer heights from lidar measurements in Boston, MA

The planetary boundary layer (PBL) defines the mixing height of air pollutants in the lowest layer of the atmosphere. It is the turbulent domain that connects the surface environment to the large-scale atmosphere and serves as a locus for vertical and horizontal transport. The air motions in the PBL are not well-resolved in numerical weather prediction (NWP) models; hence its height, wind speed, and other properties are simulated using a variety of parameterizations. It is challenging to accurately simulate the PBL and to verify PBL heights (PBLHs) retrieved from NWP models. In studies that compare atmospheric measurements of PBLH against NWP simulations, the strongest agreement is typically found during summer months[1,2], with larger systematic errors of PBLHs during spring and winter seasons[1-5]. These errors in PBL simulations can have significant impacts on assessments of ground-level air pollution and greenhouse gas fluxes[3,6]. It is critical therefore, to verify NWP simulations using observations of the PBL in order to flag good and bad days for assessing emissions or performing atmospheric transport studies.

Previous methods for obtaining information from the PBL have included radiosondes[7-8], meteorological masts[9-10], aircraft[11], sodar[12-13], wind profilers[14-15], etc. Most of the information has been limited to non-continuous data in rural environments where observations can be made without risk to aviation or disturbance to people. Most of the aforementioned methods are difficult to deploy in cities and require expensive instrumentation. Radiosondes, for example, are typically deployed twice a day at 00Z and 12Z at widely spaced sites, and thus provide information with low temporal and spatial resolution.

Recent advances in lidar technology provide a more feasible tool for estimating the PBL in urban domains at lower costs and more portable configuration. In this study, we use observations from a Mini Micropulse Lidar (miniMPL) sensor that was purchased from the Micro Pulse LiDAR division of Hexagon Geosystems (originally developed by Sigma Space Corp.) to observe aerosol loading in the atmosphere and within the PBL. A total of three sensors were available in this study located in Boston (MA), Mineola (NY), and Lewisburg (PA), which are all part of the Northeast Urban Network under the National Aeronautics and Space Administration (NASA) Carbon Monitoring System (CMS).

Inversion modeling to assess urban emissions is typically conducted during the day, when the highest air pollution levels are typically observed. In this study, we investigate the growth of the PBL using miniMPL data from morning to afternoon hours (9 to 21 UTC). In Boston, aerosol loading is expected to increase from night to day, with an increase in anthropogenic activity such as traffic and heating/cooling. *Masri et al. 2016* determined the source types for particulate matter with an aerodynamic diameter less than 2.5 microns (PM2.5) for daily air samples collected in Boston from the years 2002-2010. They quantified sources from traffic, sea salt, road dust, oil combustion, and wood burning, with traffic (21%) and wood burning (19%) being the largest. Additionally, it was found that roughly 48% of total PM2.5 mass in these air samples was associated with regional air pollution[17] (see Chapter 3 of this dissertation). These aerosol loadings are detected by our miniMPL sensors, which measure the backscattering of light from particles in the atmosphere.

The PBL responds to surface friction, heat fluxes, and evapotranspiration on time scales less than 1-hour, and its height can range from less than 100 meters to several kilometers in a given day[18-20]. During the morning hours, the PBL grows and vertically mixes air pollution from ground surface emissions, as well as entraining residual air from the previous day in the

nocturnal PBL[7] and the residual layer (herein referred to as "RL"). In order to detect these atmospheric changes, we use image processing and fuzzy logic to identify the PBL's growth and estimate its height using miniMPL data. Because lower emissions are expected at night, as Boston does not rely on energy-intensive industries[16], we typically observe the growth of the PBL as an upward propagation of aerosol loading in miniMPL measurements, followed by a steady period, between 9 to 21UTC.

Background

Atmospheric scientists use NWP models to forecast air quality. For example, the U.S. Environmental Protection Agency (EPA) uses The Community Multiscale Air Quality (CMAQ) Modeling System coupled with an NWP model or meteorological model, to investigate the transport of air pollutants from one state to another with the ultimate goal of assessing public health and environmental impacts. The scales of boundary layer turbulence are too small to be resolved in these NWP models, so they simulate the PBL using parameterization schemes, sometimes with urban-adapted parameters, leading to uncertainty in understanding ground-level air pollutant concentrations. For example, a study estimated that CO_2 concentrations could be overestimated by 40% in the day and 60% at night[3] if the PBL was not simulated correctly in the STILT model. Extensive studies[25-30] have focused on the interactions between ground-level air pollution and the evolution of the PBL. However, fewer studies have focused on reducing model-data mismatch of PBL heights in urban domains using high-resolution simulations[25]. In order for federal or state agencies accurately to assess the effects of air pollution on human population, it is critical to verify PBL simulations from NWP models with continuous *in-situ* observations on the ground.

Several previous studies have used lidar observations to investigate the PBL. For example, a number of studies aimed to investigate transition zones between the PBL and the free atmosphere[26-27], as the nocturnal PBL transitions into the convective layer in the morning hours, or as the daytime PBL reaches its maximum height and the formation of the RL may start. These studies incorporated various image-processing techniques such as gradient analysis of the lidar backscattering profile and wavelet covariance transforms[23-24] to estimate PBLHs. However, there is as yet no universal method to identify PBL height; each method comes with its advantages and disadvantages[3]. In our study, we developed an image-recognition algorithm to identify heights in Boston, MA, using miniMPL measurements. Our algorithm performs well in our study area and appears to have general applicability elsewhere.

Sampling Site, Measurements, and Data Processing

The miniMPL sampling site in Boston, MA, (42.350N, 71.104W), is located approximately 32 meters above ground level on a rooftop of a building at Boston University (Figure 1), that stands between the Charles River to the Northwest and a major interchange of the I-90 highway to the Southeast; it is surrounded by apartment buildings of similar height. The miniMPL sampling site in Mineola, New York (40.750N, 73.640W), is located in west Long Island near the Jericho Turnpike, and is surrounded by residential neighborhoods and local traffic, and two bodies of water: Long Island Sound and the Atlantic Ocean. The miniMPL units have been operating at the Boston site since September 2012, and the Mineola site, since September 2014 until the present day. All miniMPL instruments were developed by Sigma Space Corporation, now part of Hexagon Systems.

Figure 1. View of the Boston University sampling location and the miniMPL enclosure.

The laser and electronics are all located inside the box in a 24cm x 30cm x 48cm enclosure. To keep the unit safe from weather and temperature fluctuations, the miniMPL is located inside a larger enclosure unit with temperature control that includes both air conditioning and heating (shown in Figure 1). The compact miniMPL units continuously take measurements with little need for on-site maintenance. However, due to the occasional higher frequency of temperature fluctuations, which cause “stripping” effects in miniMPL profiles, a fan was installed inside the enclosure for more well-dispersed temperature distribution. The miniMPL emits light at a 532-nanometer wavelength at an angle of 180 degrees and records the backscattering of light from particles in the atmosphere.

Figure 2. The miniMPL sensor developed by Sigma Space Corp.

The miniMPL shown in Figure 2 is an aerosol backscattering lidar and a miniaturized version of the standard MPL used in the NASA global lidar network (MPLNET). An extensive description of this lidar instrument can be found in Ware et al.[4]. The miniMPL sensors are rated as eye-safe at 0 meters, and on that basis the Federal Aviation Administration has approved their use in Class A air space of Boston and New York (permit renewals are required annually) .

Raw lidar backscattering profiles are first corrected by removing deadtime, as there is a lag time between when detector resets. Measurements are then corrected by subtracting background bias determined from the signal at long return times (very high altitudes), from which there should be zero backscatter. Then, the signal is divided by the recorded laser energy (μJ) to cancel out any fluctuations in energy. Lastly, an afterpulse correction is applied to account for stray light that may be bouncing around within the lidar enclosure while never entering the atmosphere.

Figure 3 below shows the raw signal from backscattering of light at 180º detected along the y-axis and the range (up to 20 km vertical) along the x-axis, as corrections applied in sequential order: (1) deadtime correction, (2) background correction, (3) energy pulse

correction, (4) afterpulse correction, and (5) overlap correction. The raw backscattering signals in the atmosphere above roughly 2.5 km are reduced from 1.5 to nearly zero at 3 UTC after the first four aforementioned corrections are applied to the miniMPL measurements at the Boston sampling location (shown in Figure 3). Lastly, at low altitudes less than 100% of the incoming light is focused on the detector since miniMPL has a finite focal distance. The lidar data are then divided by tabulated overlap values for each altitude. However, because the miniMPL has a coaxial design these overlap corrections are minimal and signal changes are not shown in Figure 3.

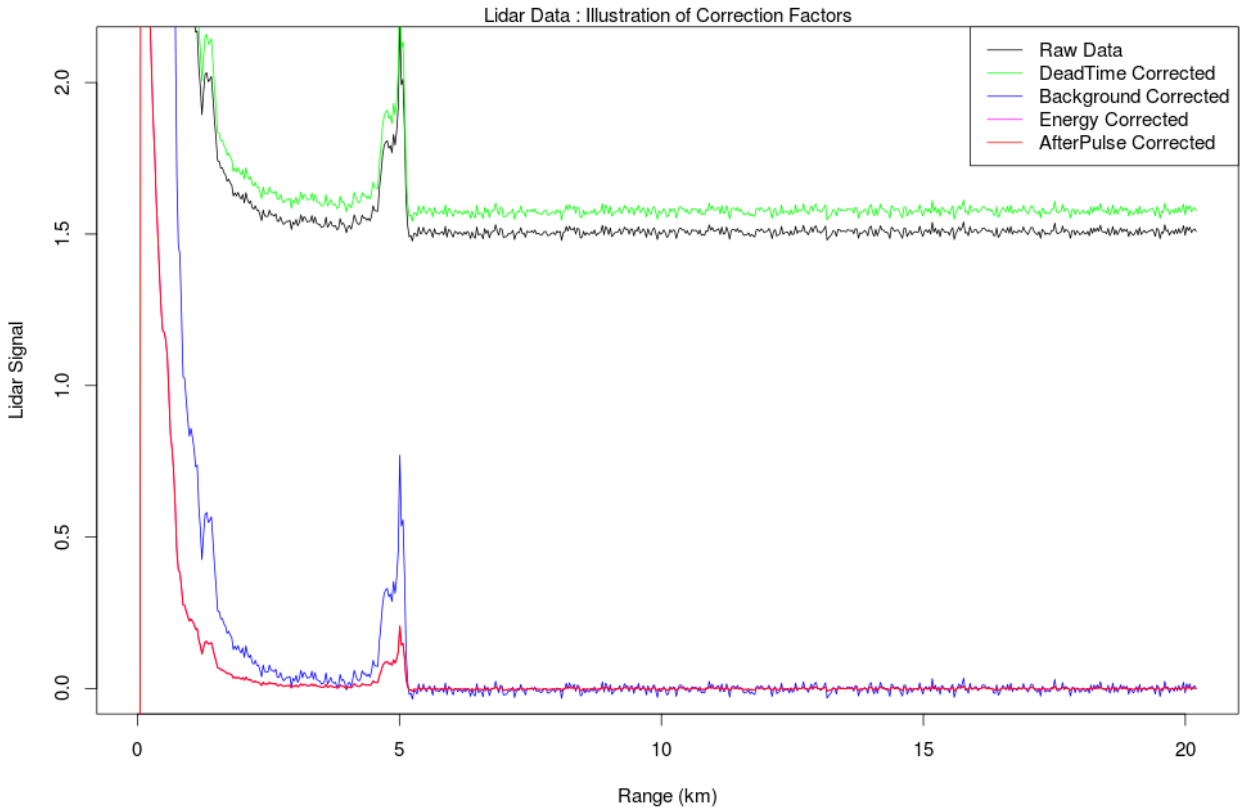

Figure 3. Changes in miniMPL signal after applying the following corrections: (1) deadtime correction, (2) background correction, (3) energy correction, and (4) afterpulse correction.

After correcting the raw signals, we obtained the lidar normalized relative backscatter (NRB) signals which represent the backscattering of light (in photon counts km^2/ μs μJ). All miniMPL NRB data were averaged over 5-minute bins at a vertical resolution of 30 meters for each day. An example of a daily NRB profile at our Boston sampling location is shown in Figure 4, which is retrieved after applying all the correction steps (Figure 3). The color scale highlights the intensity of NRB per kilometer, representing the backscattering of light from aerosols in the atmosphere. The red and white colors indicate more backscattering of light (~0.3-0.4 NRB km^{-1}) and the blue, black, and grey colors indicate less backscattering of light (~0.0-0.15 NRB km^{-1}). Daily lidar NRB profiles analyzed during the NASA CMS study period from September 2013 to November 2014. In order to identify PBL heights and image recognition algorithm was developed to further analyze Lidar NRB profiles.

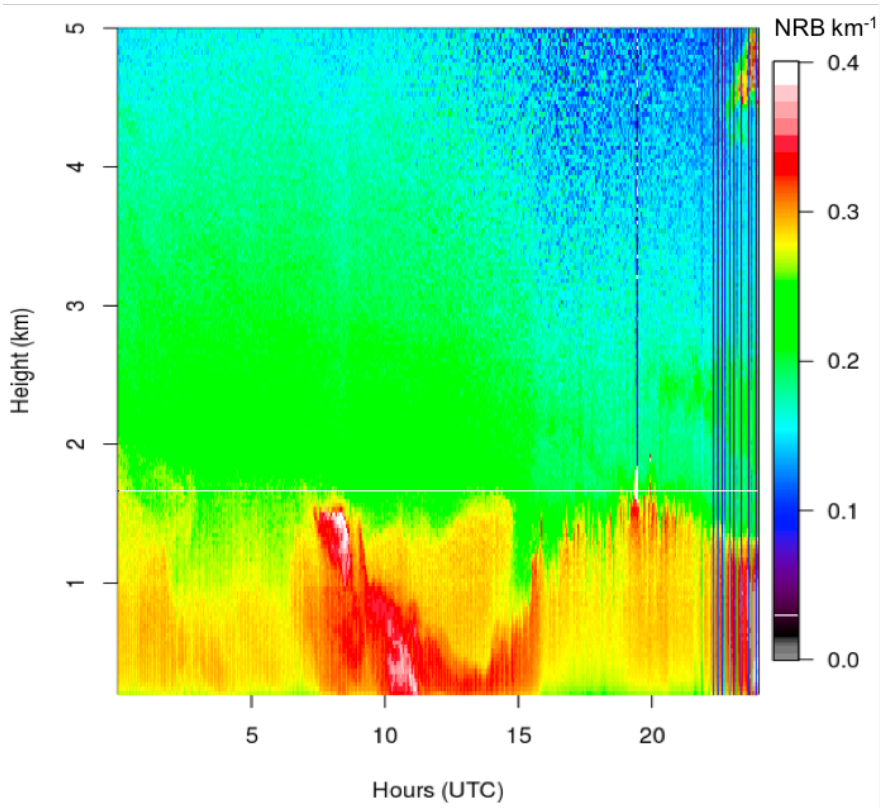

Figure 4. The lidar NRB profile for September 25, 2012, from 0 to 24 UTC at our Boston site,

(Continued)

after corrections are applied. The color scale reflects the lowest (grey/purple/blue) to highest (green/orange/red/white) backscattering of light at 180º, ranging from 0.0 to 0.4 NRB km^{-1}. On this day we observed enhanced backscattering signals in the residual layer overnight, that became entrained in the growing PBL starting at 13 UTC (8AM, local standard time).

Detecting the PBL using lidar measurements and wavelet filtering

In this study, the daytime PBL was defined by observing aerosol loading from surface emissions that is mixed into the convective layer between 9 to 21UTC. Signal changes were detected in aerosol loading vertically dispersed from the lower part of the atmosphere, where anthropogenic and biogenic emissions are occurring, into the residual layer or the free atmosphere. PBL growth is driven by buoyancy generated by warming and moistening of the surface from incoming solar radiation and evapotranspiration. Larger lidar NRB signals were anticipated in the growing PBL with an increase in anthropogenic activity or surface emissions that contribute to an increase in aerosol loading. Once the PBL is fully developed in the afternoon hours and right before the PBL begins to collapse at sunset, a residual layer begins to form. The RL that contains pollutants from the previous day or earlier. Both layers typically contain larger NRB signals in comparison to the free atmosphere.

Many signal processing methods exist to detect shifts or to denoise data in order to retrieve signals of interest. Here, several image processing techniques, including discrete wavelet filtering[28-29], image thresholding[30], and singular value decomposition[31] are applied to the lidar NRB profiles in order to identify atmospheric structures of interest: the planetary boundary layer and the residual layer. Discrete wavelet filtering is often used for denoising, pattern recognition, and signal filtering. Since lidar measures the backscattering of light from aerosol

loadings which take places within the PBL, wavelet filtering or transforms are commonly used to retrieve PBLHs from lidar data[1, 25-26]. We first tried processing our lidar NRB profiles with the Haar wavelet function, as described by *Lewis et al., 2014*[1], and then explored using other discrete wavelets such as the first derivative Gaussian (FDG), as many of our structures exhibit rapid sigmoidal fluctuations. A side-by-side comparison of the FDG and Haar wavelet functions is shown in Figure 5. Performing wavelet filtering or wavelet convolutions provides localized signal denoising of our time series of our 5-minute averaged lidar NRB profiles. The wavelets were adjusted to a dilation of 8 in order to capture signal changes in the vertical structures for our time series of NRB data from our miniMPL measurements.

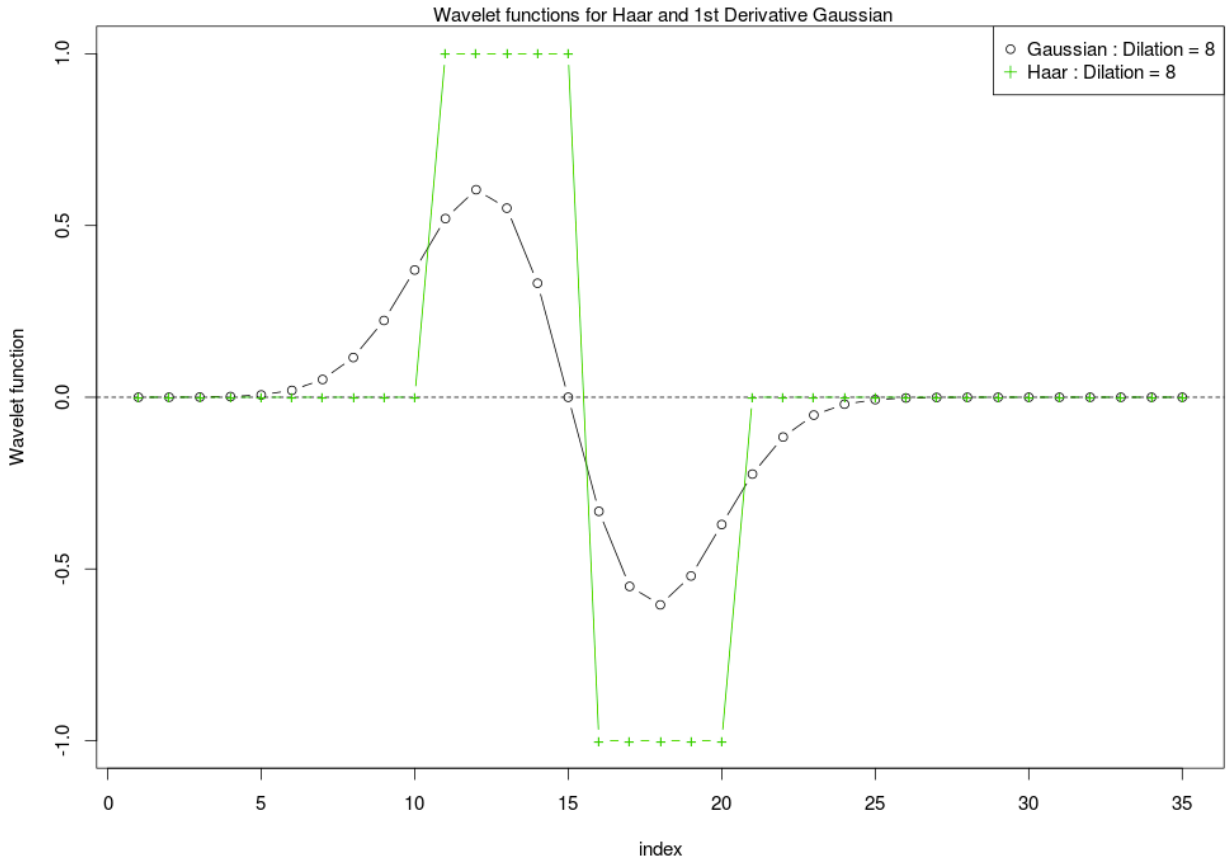

Figure 5. First derivative Gaussian vs. Haar wavelet functions with a dilation of 8.

Figure 6 is an example of the miniMPL NRB profile on September 25, 2012, at one time point (12:27:35 UTC). Processing lidar profiles using wavelet filtering helped detect shifts in NRB signals throughout the day, retrieving the most prominent atmospheric structures. Throughout our analysis, the FDG wavelet filtering seemed to heighten atmospheric structures in comparison to the Haar wavelet. In Figure 6, the first largest signal, representing the steep slope at the top of the PBL, occurs around 0.4 km, a typical height for the growing PBL in the morning hours. The second largest signal around 1.5 km, appears to indicate the top of the residual layer. Although some noise was still present after processing the lidar data, the wavelet filtering was an effective method for denoising lidar NRB profiles and identifying atmospheric layer boundaries from the maxima of the FDG wavelet filtered profiles.

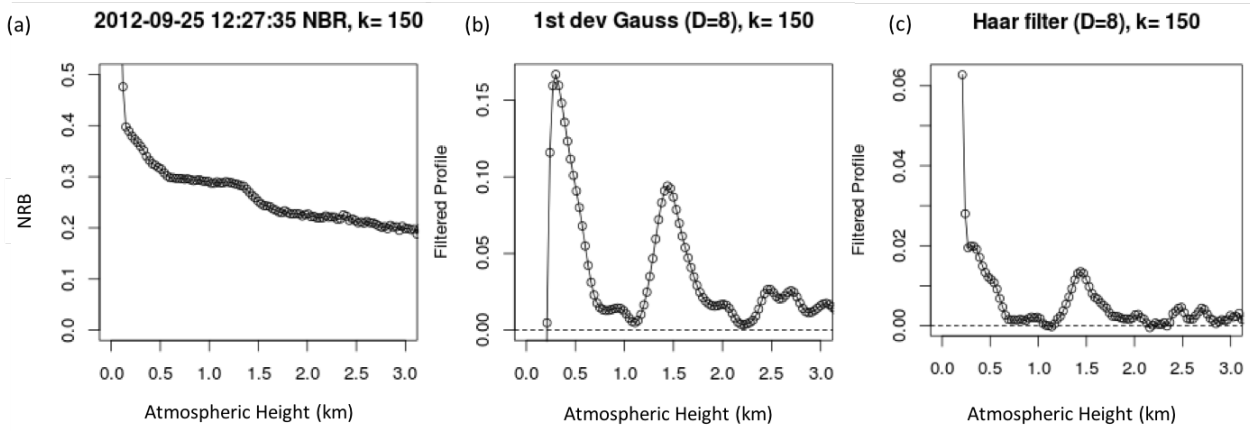

Figure 6. The NRB signal for September 25, 2012, at 12:27:35 UTC was processed to detect signal changes using FDG and Haar wavelets filtering.

The post-processed lidar images using the FDG vs. Haar wavelet filtering for the entire day on September 25, 2012, are shown in Figure 7 below. As expected, both wavelet functions enhance signal changes in the NRB profiles, heightening atmospheric structures such as the

boundaries between the PBL, the RL, and the free atmosphere. On this day, the growth of the PBL occurs roughly from 13 to 21 UTC and the RL is identified roughly between 1.5 to 2.0 km in the lidar NRB profile after wavelet filtering is performed. In the remainder of our study, the first derivative Gaussian function was selected as the primary wavelet, as the PBL and RL signals are more heightened in the post-processed daily lidar NRB profiles.

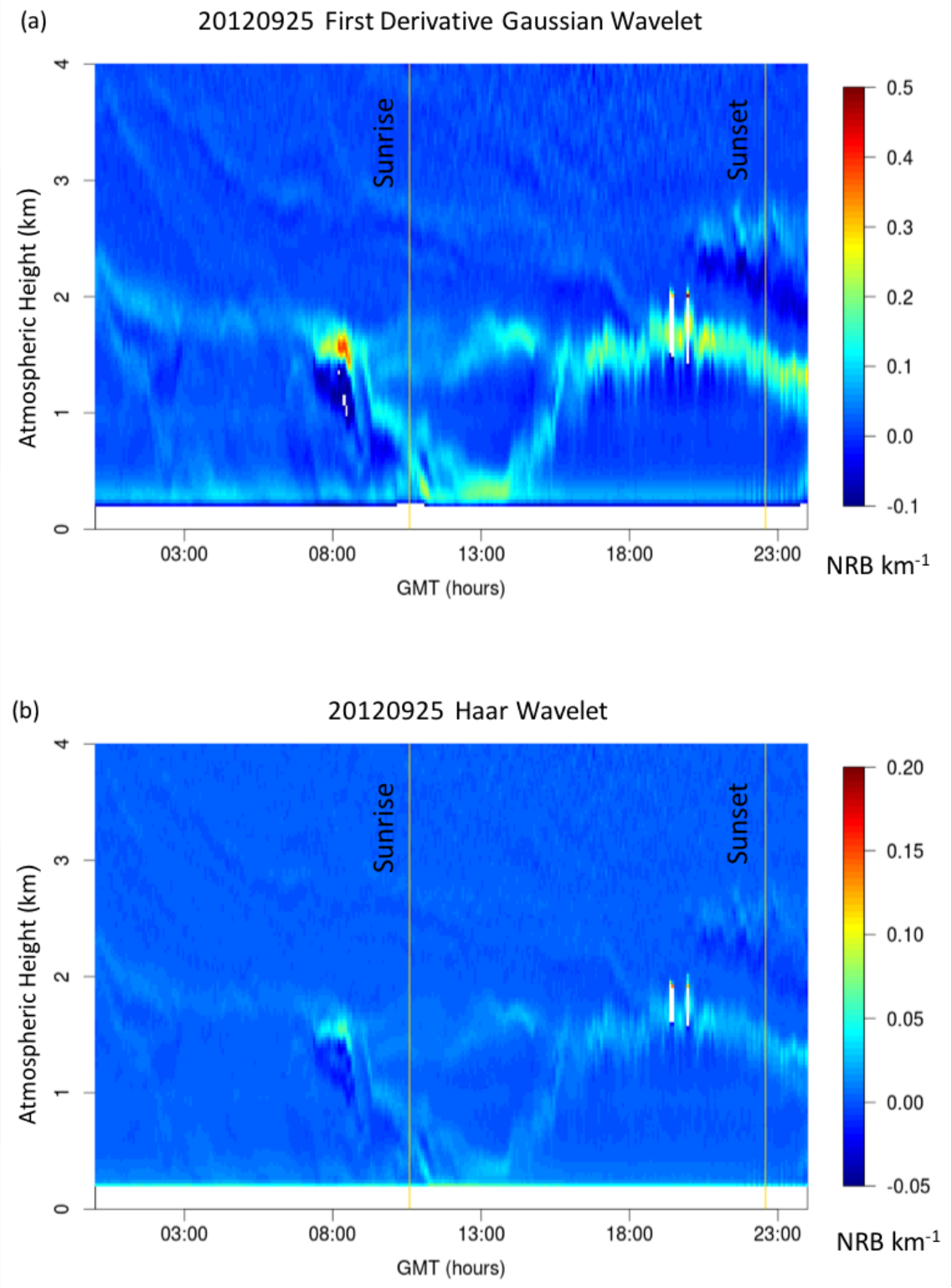

Figure 7. The post-processed lidar NRB profile, after applying wavelet filtering using FDG and Haar wavelets on September 25, 2012, at our Boston sampling site.

Developing an image recognition algorithm to estimate PBL and RL heights

Here we describe how we used our image-recognition algorithm to determine PBLHs from miniMPL data from 9 to 21 UTC. The miniMPL sensor used in this study had a blind zone below approximately 150 meters above ground level (magl), due largely to the afterpulse. At times, especially in the late afternoon hours, our image-processing algorithm had difficulty distinguishing the PBL from other aerosol signals, in particular, the residual layer and sea breeze/marine layer. Sea breezes in the afternoon hours, identified by the occurrence of easterly winds after 16 UTC in the Weather and Research Forecasting (WRF) model, were often associated with large aerosol backscatter signals from the marine layer. The sea breeze front can lift the land based PBL from the surface, resulting in a very complex atmospheric structure (see Chapter 2 for more discussion). The associated aerosol signals, at times, were stronger than the fully developed PBL or collapsing PBL. Additionally, rain was screened out in this analysis (precipitation greater than zero millimeters in the assimilated meteorology from the WRF model). Therefore, our image-processing algorithm focused on identifying the growth phase of the PBL, when the PBL exceeded 200 meters above ground level and was at least 100 meters below the RLH, for the hours between 9-21 UTC.

Enhanced NRB signals in the RL typically arise as a pollution signal from the previous day(s) PBL. Pollutants remain aloft in the RL after the PBL begins to collapse due to the cooling of the earth's surface after sunset, and these aerosols can be advected to our region over night and during the next day. The height and aerosol content of the RL typically exhibits slow variations throughout the night and day especially during the morning hours as air within the RL and nocturnal PB is entrained in the convective layer. These entrainment process can create complex structures difficult to differentiate using lidar data. Here we detected the RL in lidar

NRB profiles by applying singular value decomposition (SBD), after processing the daily lidar NRB profiles with FDG wavelet filtering (see Figure 7), exploiting the persistence and relative slow variations of the RL on most days.

In linear algebra, SVD is a numerical technique that uses matrix decomposition. SVD looks at subsets of data (separating the matrix into three sub matrices) and arranges the data so that the most important large-scale information is associated with the patterns corresponding to the first singular values. The resulting product is a matrix that is an approximation of the original matrix but includes only the large-scale patterns and structures. Here, an entire day of lidar NRB profiles is our image matrix. After performing SVD, we used the first three singular values that contain the largest amount of information of light intensity in our Lidar NRB profile. In Boston, the lidar sensor typically shows a signal change from the RL to the free atmosphere (i.e. more to less backscattering of light from aerosols in units of NRB km^{-1}). SVD was used to detect the RL in NRB profiles, as it typically has the largest signal from 0 to 24 UTC.

Since PBH can approach the top of the RL in the afternoon hours, when the PBL is fully developed, the RL becomes difficult to distinguish from the PBL; it may be fully entrained and cease to exist. We used fuzzy logic to identify the RL when it was at least 100 meters above the fully developed PBLH (Figure 6c) in the afternoon hours before 21UTC. Our image-recognition algorithm was effective in retrieving PBLHs and RLHs for approximately 32% to 68% of the days each month during our CMS study period from September 2013 to November 2014), with the exception of August 2014 when our lidar unit was down for maintenance (see Table 1 below). The lowest rate of retrievals of PBLHs and RLHs occurred during the month of December, and the highest rates during May and July of 2014.

Table 1. Total days of Lidar-retrieved PBLHs and RLHs for each month of the CMS study period in Boston, MA, using our image-recognition algorithm.

Month	Lidar Algorithm PBLH retrievals
Sep 2013	15 days
Oct 2013	14 days
Nov 2013	13 days
Dec 2013	11 days
Jan 2014	16 days
Feb 2014	14 days
Mar 2014	14 days
Apr 2014	18 days
May 2014	21 days
Jun 2014	18 days
Jul 2014	21 days
Aug 2014	6 days
Sep 2014	13 days
Oct 2014	10 days
Nov 2014	18 days

Our image-recognition algorithm included the following five primary processing steps:

Step 1: Process lidar NRB profiles using first derivative Gaussian wavelet filtering.

The 5-minute averaged lidar NRB profile on September 25, 2012 (see Figure 4 above) was processed using first derivative Gaussian (FDG) wavelet filtering (see Figure 8 below). Using this image recognition method, atmospheric structures are heightened, hence, allowing us to identify the growth of the PBL, which we expected to occur between 9-21 UTC. In particular, the top of the residual layer is highlighted, bounding the layer with pollution signals

arising from primary or secondary aerosols in the previous day(s) PBL. Because our miniMPL sensor contains a blind zone of roughly 150 meters, the nocturnal PBL cannot be seen here.

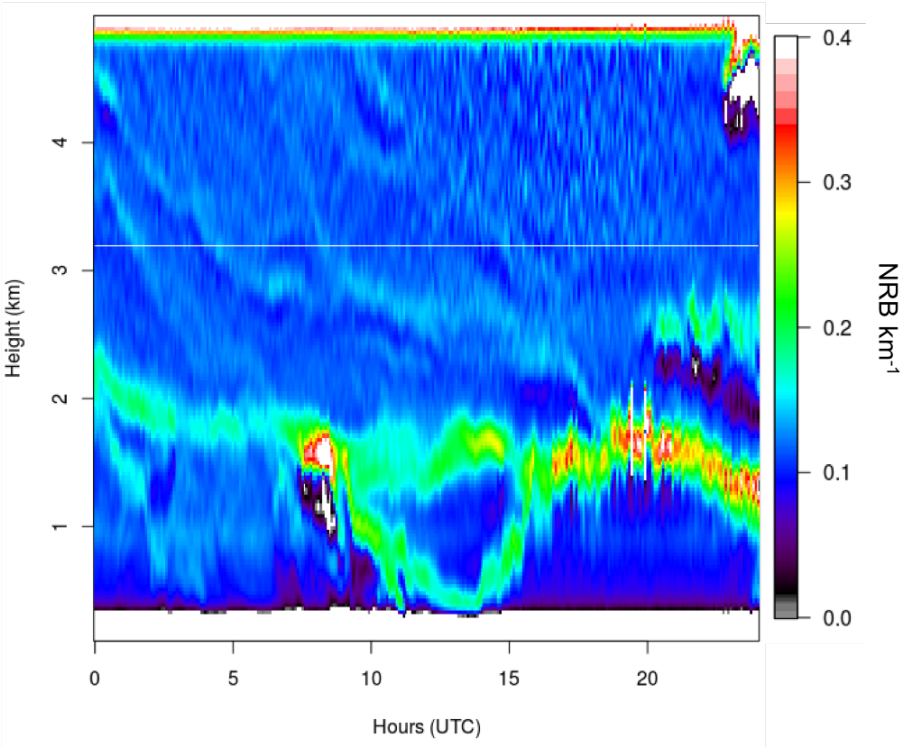

Figure 8. FDG wavelet filtering of the lidar NRB profile for September 25, 2012, in Boston, MA. The highest backscattering signals (0.3 to 0.4 NRB km-1) are showing in colors red and white and the lowest backscattering signals (0.0 to 0.15 NRB km-1) are show in grey, black, and dark blue colors. Our image-recognition algorithm does not process lidar NRB profiles 200 below magl.

Step 2: Image thresholding of the FDG wavelet filtered profile.

In order to identify the height of the atmospheric structure, image thresholding was applied to the lidar image after processing with wavelet filtering. In Figure 9 below, a comparison of image thresholding in color and greyscale is shown for the post-processed NRB profile (shown in Figure 8 above). The FDG NRB image was broken down to its RGB

components and a threshold was applied in order to replace each pixel with a different color. To identify atmospheric structures of interest such as the PBL in lidar profiles, image thresholding is useful. It allowed us to detect the edges of our structures and to detect repeated segments of colors in atmospheric structures. These were heightened after processing the lidar profiles with wavelet filtering, making it possible for heights to be retrieved along the edges of these structures. Image thresholding was incorporated in our image-recognition algorithm to retrieve PBLHs/RLHS from miniMPL measurements.

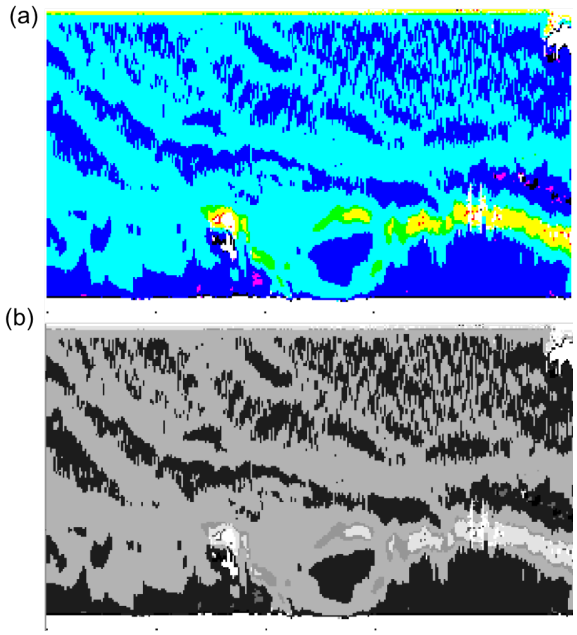

Figure 9. Color (a) and grayscale (b) image thresholding of the FDG wavelet filtered NRB image/profile for September 25, 2012, at the Boston sampling location.

Step 3: Perform singular value decomposition (SVD) on the FDG wavelet filtered profile.

To test the performance of SVD with our miniMPL data, we performed SVD on the NRB image (Figure 10a), after it was processed using FDG wavelet filtering (Figure 10b), for an example day on August 21, 2013. Here, we show the SVD-processed image by reproducing our

image matrix using the first singular value (Figure 10c) and the first three singular values (Figure 10D). The RL can be seen as a generalized RL, with a relative constant height of roughly 1.9 km (Figure 10c). Using the first three singular values, however, variations of the RL throughout the day (~1.6-1.9 km) are captured (Figure 10d). Therefore, we included the first three singular values of SVD in our image-recognition algorithm.

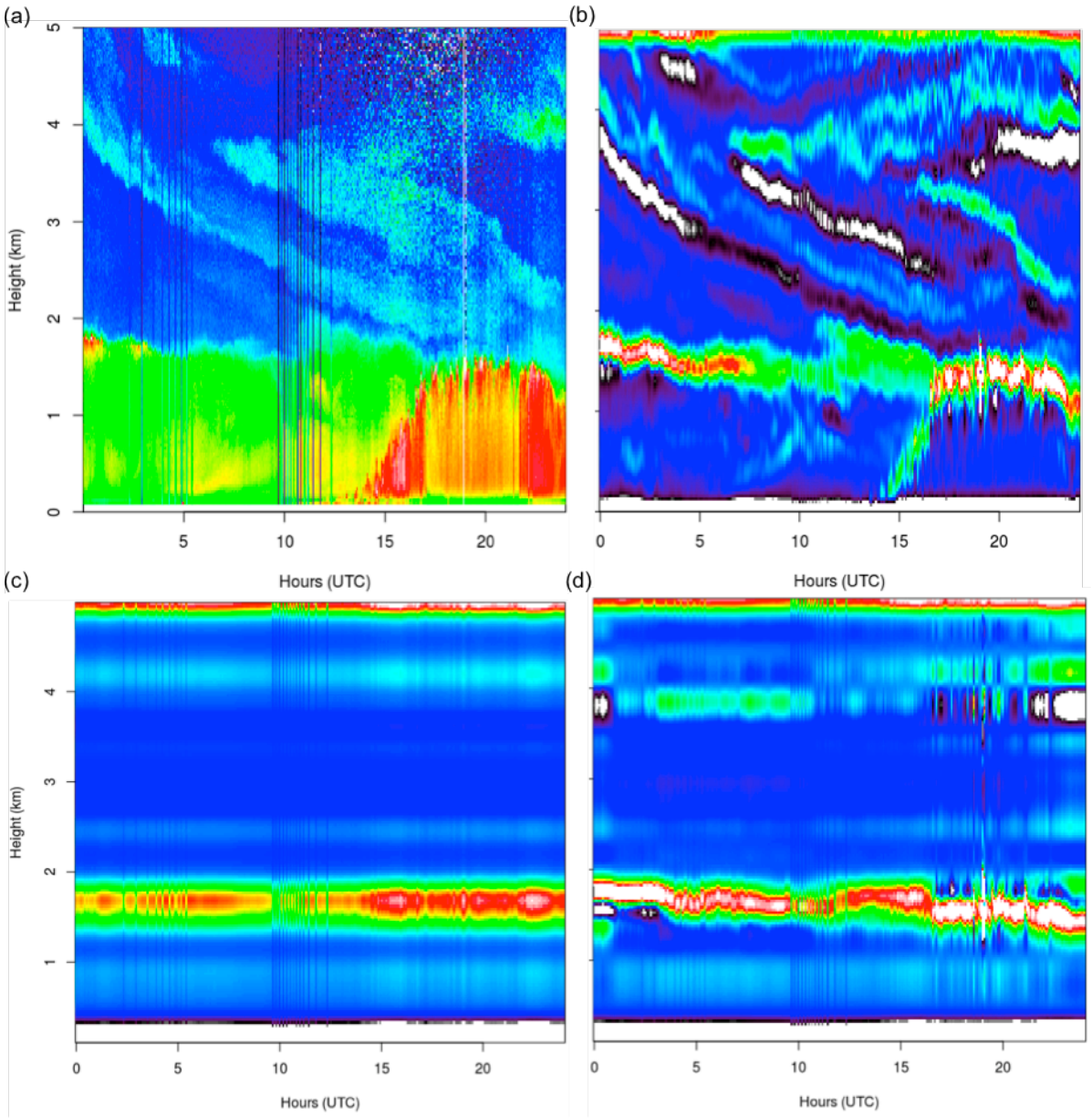

(Continued)

Figure 10. SVD image processing was used on lidar NRB profiles (a), after performing FDG wavelet filtering (b), to retrieve RLHs on August 21, 2013. We compared the image matrix reconstructed via SVD using the first singular value (c) and the first three singular values (d).

We continued to process the FDG wavelet filtered NRB profiles for the remainder of the CMS study using SVD. Referring back to our sample case on September 25th, 2012, the SVD product image (Figure 11) heightens the RL and its fluctuations, between approximately 1.2-1.9 km and at an NRB value of approximately 0.18-0.35. Note the collapse of the RL around 22 UTC. While measuring the backscattering of aerosol loadings in the atmosphere with the miniMPL, the RL signal may be mixed with the collapsing PBL signal occurring once cooling takes place after sunset. However, this process is not relevant in our study as we focus on retrieving growing PBL heights from 9-21 UTC at our Boston sampling location.

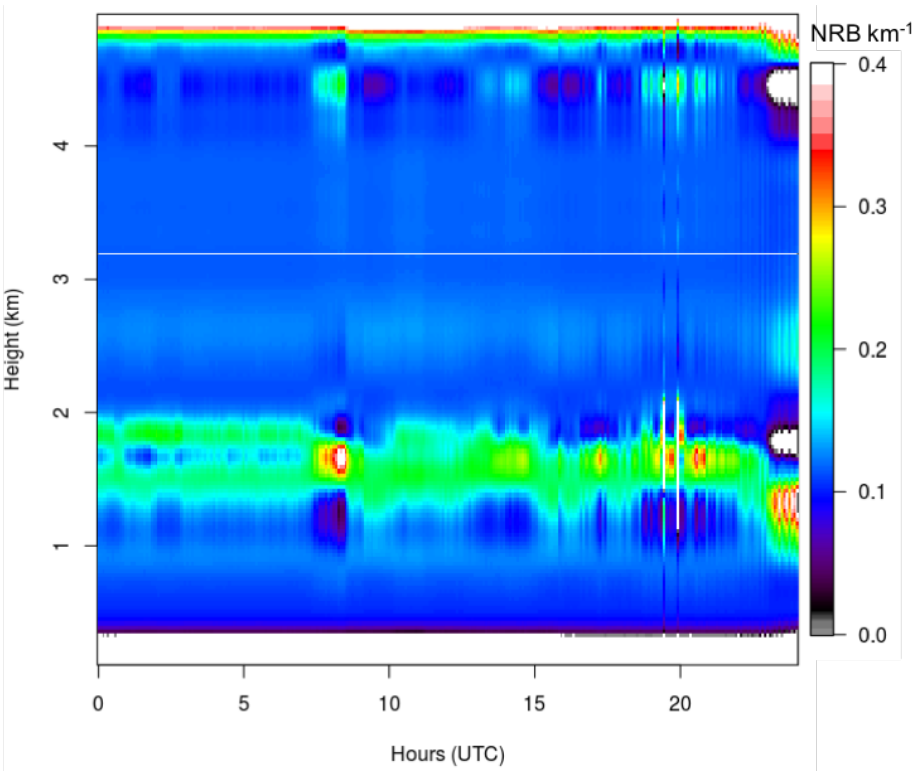

(Continued)

Figure 11. The RL is heightened using the first three singular values in SVD to reconstruct the image matrix of our FDG wavelet filtered NRB profile (see Figure 8 above) from miniMPL data on September 25, 2012, at our Boston sampling location. Note: all miniMPL profiles were evaluated above 200 meters, where there is a blind zone in lidar measurements.

Our image-recognition algorithm used the SVD function that is integrated into the R statistical programing software. The SVD function breaks down our 2-D image matrix (our daily miniMPL NRB profile) into three matrices: left singular vectors (u), right singular vectors (v), and the diagonal (d) of singular values. In our study, we found that the first three singular values in (d) of our 2-D matrix, were sufficient for detecting the generalized RL and some of its fluctuations throughout a day in the first derivative Gaussian wavelet filtered image of the lidar NRB profiles.

Step 4: Retrieve RLHs/PBLHs along structure edges using repeated segments function.

After processing the miniMPL profile with FDG wavelet filtering, SVD, and image thresholding, each atmospheric structure detected in the post-processed image product was evaluated to identify RLHs and PBLHs. In Figure 12 below, the atmospheric structures were retrieved by using a repeated segments function to identify gray scale colors repeated in lidar profiles after performing image thresholding (discussed in Step 2). The repeated segments function finds segments of each vertical sounding in our time series where, the grey scale exceeds a “key value” (Figure 9b). We selected a key value of 140 which represents a light grey color in our grey scale image. Two vertical soundings are compared in our grey scale image, in order to retrieve the RGB value at the initial and next nearest height. After collecting heights

where the RGB exceeds are key value, atmospheric layers are captured in our miniMPL profiles.

For example, on September 25, 2012, layers nos. 3 through 7 are shown. These layers were retrieved from the greyscale image thresholding product shown in Figure 9b. In this example, layer no. 6 is indicative of the growing PBL that is expected from 9-21 UTC. In order to retrieve the growing PBLHs with our image-recognition algorithm, we used fuzzy logic. In our logic, we included conditions such as: (1) anticipating the starting height of the growing PBL between 9 to 13 UTC, (2) evaluating heights above 200 meters due to the blind zone in our miniMPL sensor, and (3) limiting heights to roughly 100 meters below the retrieved RLHs that were retrieved using SVD (discussed in Step 4). The RLHs were retrieved by applying a locally weighted scatter plot smoothing (herein referred to as “lowess”) of the retrieved RL from the SVD matrix (discussed in Step 3) and is further discussed in the next step for the growing PBLHs. In Figure 12 below, we show the SVD and lowess retrieved RLH (solid black line) in order to compare to atmospheric structures retrieved by the repeated segments function.

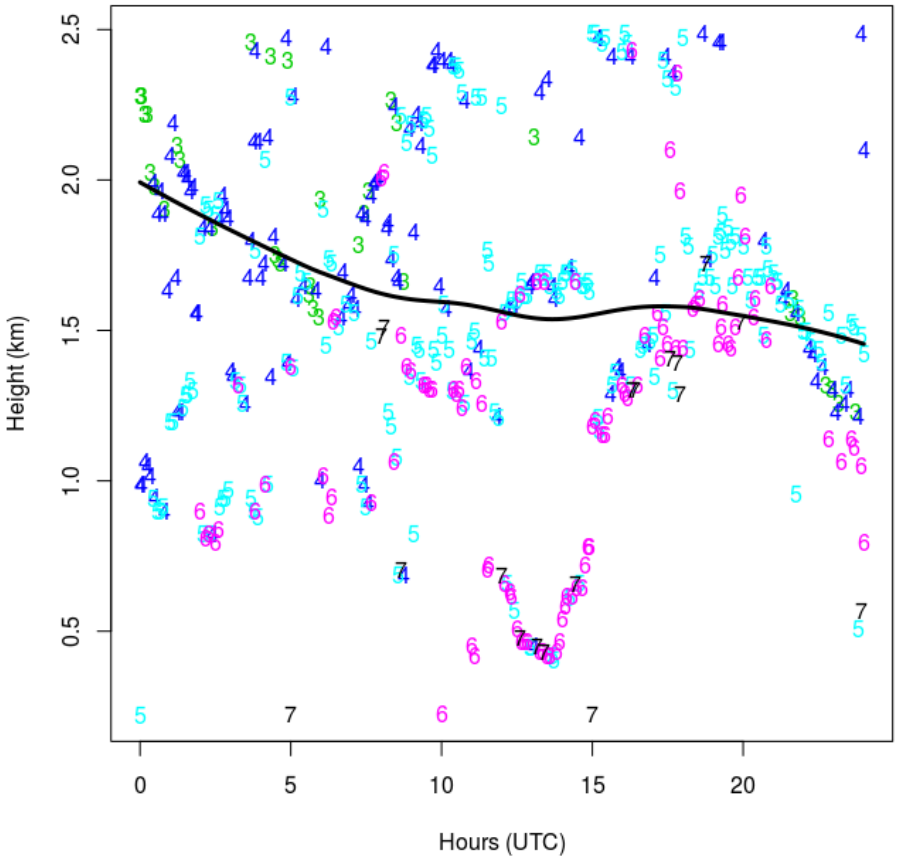

Figure 12. Atmospheric layers are retrieved from the greyscale image thresholding product by using the repeated segments function. On September 25, 2012, we retrieve up to 7 layers where, the RGB value exceeds our "key value" in our grey scale image.

Step 5: Use lowess or an error function model fit to retrieve the growing PBLHs.

After our image-recognition algorithm detected the PBL in the corresponding atmospheric layer, either a lowess or an error function model was applied to retrieve the height variation of PBLH over time. For the September 25, 2012 case, the starting growth of the PBL is detected around 13 UTC in atmospheric layer no. 6 (shown in Figure 12 above). A lowess function locally-weighted the time series of our scatter plot that contains heights of retrieved atmospheric layers, which is discussed in Step 4. Here, we used the lowess function from the R

statistical programming software, using a smoothing span of 10%. At times, the lowess function did not effectively retrieve the growing PBLHs and thus, a second method was applied using an error function model fit on the detected PBL. A side-by-side comparison of the lowess vs. error function model fit for September 25, 2012, is shown below. The retrieved PBLHs using our image-recognition algorithm are shown as black dots in Figure 13. The representation of PBLH for each day is provided by the resulting lowess or error function fit.

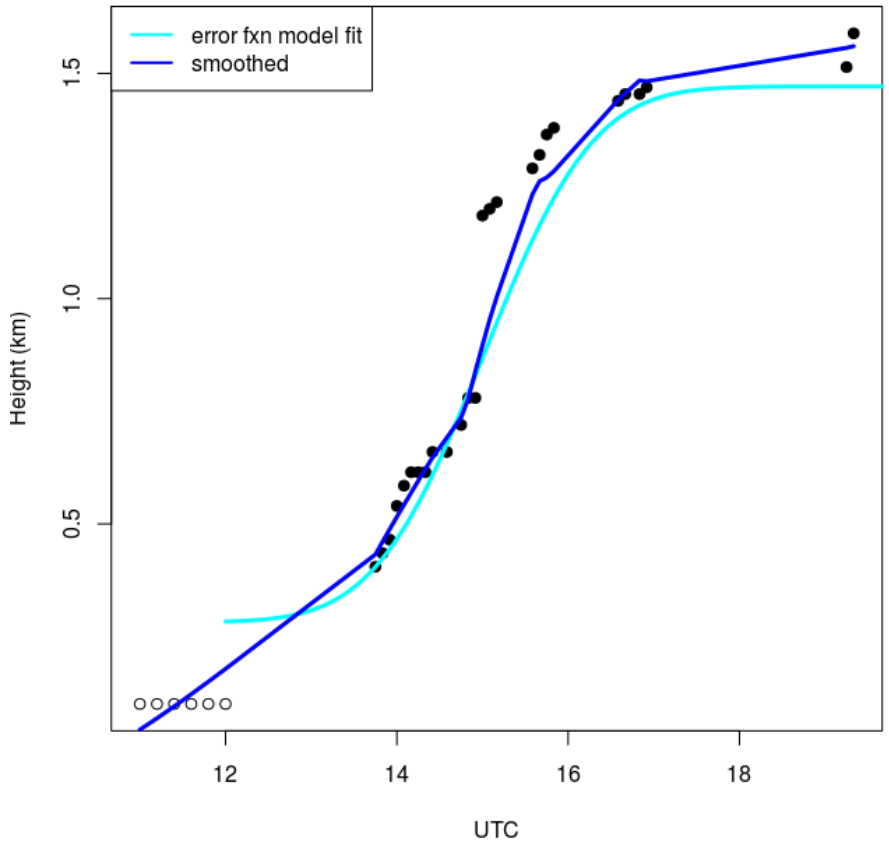

Figure 13. The lowess vs. error function model fit of the detected growing PBL using our image-recognition algorithm on September 25, 2012, at our Boston sampling location.

Chapter 2

Using lidar to evaluate PBL simulations from numerical weather prediction models and improve estimates of CO_2 fluxes in LPDMs in Boston, MA

The *Intergovernmental Panel on Climate Change Task Force on National Greenhouse Gas Inventories* (IPCC TFI) has focused on developing and refining GHG inventories at national scales. But recently, the Paris Agreement and Lima-Paris Action Agenda have recognized the critical role of subnational entities, especially cities. Over the past several years, cities and states have pledged to take action in reducing greenhouse gas emissions with the pending withdrawal of the U.S. from the Paris Climate Accord[6]. Emission reduction efforts to mitigate GHG emissions require the costly transformation of our current energy infrastructure. Therefore, a framework to monitor and verify GHG emission reduction efforts is key to establish accurate baselines at urban and subnational scales and to implement effective policy strategies. These recent shifts in policies highlight the importance of developing and validating models that can accurately distinguish regional pollution from a city's or state's air pollution, enabling assessment of progress towards the reduction of emissions.

Accurate simulations of the PBL height are critical to determining GHG emissions from observations[35]. The PBL responds to surface forcing on timescales of less than 1-hour[18] and spatial scales of 0.1-10 km and may be perturbed by mesoscale circulations (e.g. sea breeze), posing strong challenges to simulations using NWP models. At the smaller spatial scales (>1km) the urban boundary layer interacts strongly with the surface layer, which is driven by surface roughness and can extend up to few hundred meters[18]. Our miniMPL sensor provides long-term continuous observations with high vertical range resolution of 30 meters, and temporal resolution of 30 seconds, and therefore the backscattering of aerosols is an effective tracer for assessing the fluctuations in the urban boundary layer, and often the PBL-surface layer interface. We used our miniMPL sensor to assess NWP simulations by distinguishing good

from bad days in performance of atmospheric transport models and helping select the best PBL parametrizations for a particular region. Previous studies have shown lidar observations to be helpful in assessing NWP models such as WRF in cities[6,36-37]. Recent advances in remote sensing technology, including lidar, have allowed us to take continuous measurements of the atmosphere in urban domains.

Here, we use lidar data from our miniMPL and the PBL heights retrieved from our image-recognition algorithm (discussed in Chapter 1) to evaluate simulations from a suite of NWP models in Boston, Massachusetts. The NWP models investigated included: four configurations of a forecast model (Weather and Research Forecasting, WRF) model, two operational products (the North American Mesoscale, NAM, and Global Data Assimilation System, GDAS), and one reanalysis product (the North American Regional Reanalysis, NARR). We also evaluated the performance of two Lagrangian Particle Dispersion Models (LPDMs), the Stochastic Time-Inverted Lagrangian Transport (STILT), coupled to the WRF model meteorological fields, and the Hybrid Single-Particle Lagrangian Integrated Trajectory (HYSPLIT), coupled to NAM meteorological fields, that were used to estimate carbon dioxide (CO_2) fluxes in Boston[6]. Our work shows how a simple, robust lidar can help estimate GHG emissions in cities.

Sampling site and measurements.

Observations of carbon dioxide were measured with a Picarro cavity ringdown spectrometer at our Boston miniMPL sampling location (42.350N, 71.104W), as well as at four other stations in Massachusetts and New Hampshire[6]. The Picarro instruments at each site also measured CO, H_2O, and CH_4. Sites at Boston University (location of the miniMPL) and Copley Square sites sample at 29 magl and 215 magl, respectively, providing observations of the vertical gradient of CO_2 concentrations. The Copley site is typically within the afternoon PBL but at

times, can remain above the nocturnal PBL. Data from stations outside of the city were used to calculate CO_2 concentrations entering the urban domain and were subtracted from the urban data to define CO_2 enhancements in the urban core[6]. The Northeast Measurement Network is shown below in Figure 14; the two background sites primarily used for this study are at Harvard Forest and Martha's Vineyard in Massachusetts. At the Boston University sampling location, a miniMPL instrument measured the backscattering of light from particles in the atmosphere at an angle of 180 degrees.

A second miniMPL instrument in Mineola, New York (40.750N, 73.640W), is located in west Long Island near the Jericho Turnpike and surrounded by residential neighborhoods and local traffic, and two bodies of water: Long Island Sound and the Atlantic Ocean. The lidar units have been operating at the Boston site since September 2012 and the Mineola site since November 2014. Specifications of the miniMPL sensors are discussed in Chapter 1.

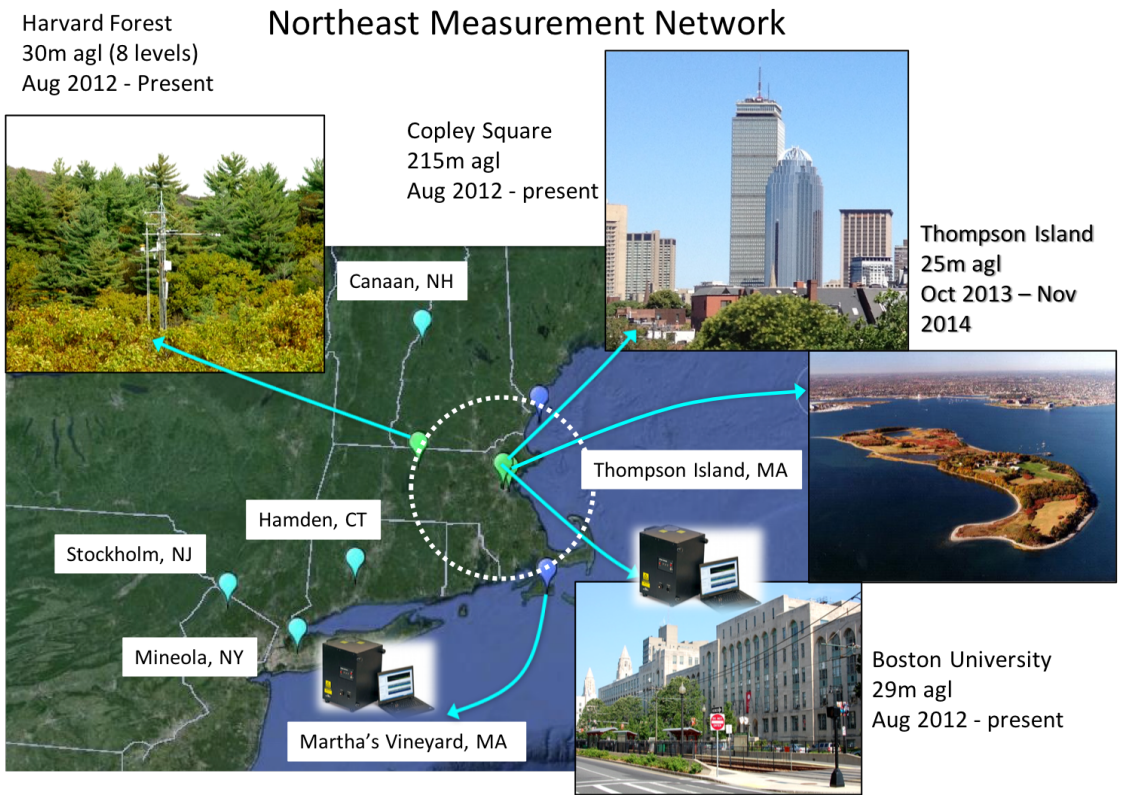

Figure 14. The Northeastern Measurement Network includes urban (Boston University and Copley Square stations) and background sites (primarily Martha's Vineyard and Harvard Forest). The 90-km radius shows our NASA CMS study area in the greater Boston area.

Numerical Weather Prediction Model Setup.

In the first phase of our NWP analysis, three configurations of the forecast model WRF[30,31], using different options for PBL parameterizations and urban canopy treatment, were employed to compute the PBL heights and compare simulations against miniMPL-retrieved PBLHs in Boston, MA. Each of the WRF configurations included a single-layer urban canopy model[38] to account for the effect of the urban landscape (buildings, roads etc.) on the fine-scale meteorological circulation. For the Boston site, we compared three different WRF configurations:

1) BOS_v341: WRF v. 3.4.1 using second-order MYJ PBL scheme and urban roughness lookup tables. Used for Boston methane study by McKain et al.[45];
2) BOSDC_NUDAPT: WRF v. 3.6.1 using MYJ PBL scheme and urban roughness database. Used for Boston carbon dioxide study by Sargent et al.[6];
3) BOSDC_TOPOW: a variant of (2), which differs only in use of the first-order YSU PBL scheme with the topographic wind correction[46] enabled.

All three configurations were compared over a two-month (June 20 – August 31, 2013) period, while the NUDAPT and TOPOW configurations were compared for an eight-month period (June 20, 2013 – February 28, 2014). The BOS_v341 includes four nested grids (27, 9, 3, and 1 km grid spacing), with physics options corresponding to those of the Turb-U configuration used in the Salt Lake City study by Nehrkorn et al[47]. The two v. 3.6.1 runs (BOSDC_NUDAPT and BOSDC_TOPOW) used a different set of four nested grids covering the entire northeast corridor, with grid spacing of 36, 12, 4, and 1.33 km (Figure 15). A total of 40 vertical levels were used with average vertical spacing of 250 meters, from 250 meters to 2.0 km, and 500 meters, from 2.0 km to 5.0 km. In addition, an updated WRF version (v3.6.1 vs. v3.4.1) and city-specific urban parameter database from NUDAPT-44 (BOS_v341 used lookup tables based on land-use category) was used in these runs. The innermost nested grids at 1 km or 1.33 km, respectively, from WRF contain the highest resolution and were utilized to compare PBL simulations in Boston.

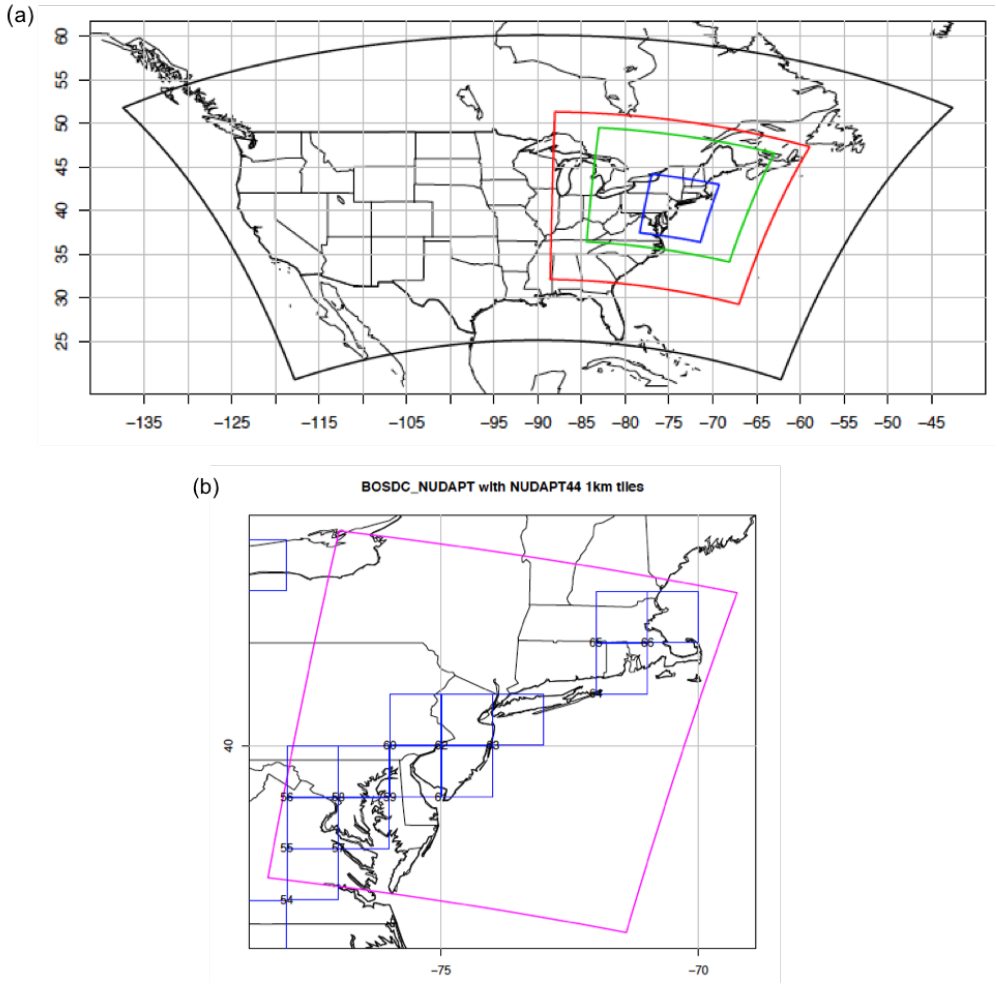

Figure 15. Four nested domains with the smallest in the horizontal direct at of 36, 12, 4, and 1.33 km (a), for the BOSTON_NUDPAT WRF runs and close-up of innermost WRF domain for Boston-DC WRF corridor runs (b). Overlaid in blue are the tiles of available urban parameter data (1-km resolution) from BOSTON_NUDPAT.

In the second phase of our NWP study, miniMPL-retrieved PBLHs were also compared from September 2013 through November 2014 with the following models: Advanced Research WRF (WRF-ARW) at 27 km, NARR at 32 km (Mesinger et al.[48]), NAM at 12 km (Janjic et al.[49]) and GDAS at 0.25-degree grid (Kleist et al.[50]). PBL simulations were compared directly with PBLHs retrieved at our Boston miniMPL sampling location. For both phases of our NWP analysis, if precipitation or sea breeze was detected in WRF meteorological simulations, those

time periods were removed from the study. We used the nearest grid point to retrieve the modeled PBLHs from each NWP at our Boston sampling location, consistent with the first phase of our NWP study.

MiniMPL-retrieved vs. NWP model simulations of PBL heights.

We assessed the heights of PBL simulations from several NWP model configurations by comparing them to miniMPL PBLHs derived from our image-recognition algorithm (discussed in Chapter 1). Because inversion modeling studies are typically conducted in the daytime hours, when transport errors are less and air pollution levels are the highest, PBLHs were compared from 9 to 21 UTC, which includes the growth of the PBL.

The two v.3.6.1 configurations (BOSDC_NUDAPT and BOSDC_TOPOW) performed better than the older v.3.4.1 configuration during the summer period (Figures 16a). BOSDC_NUDAPT showed the best performance during all three periods. Overall, the models performed inconsistently during sea breeze occurances, which are regular events in Boston. Agreement between NWP model simulations and miniMPL retrievals of PBLH showed some improvement when the days with sea breezes were omitted from the analysis (Figure 16a, 16b, and 16c), especially during the fall and winter months. In the summer, biases in PBLH are not significantly reduced after 16 UTC. During the late afternoon hours (18-21 UTC), the WRF model simulated the PBL collapsing early in comparison to the miniMPL-retrieved PBLH. These results highlight that sea breeze conditions are not resolved well, even with higher resolution models (1 km or 1.33 km). More computing power would be required and thus, additional research needs to be conducted, as many cities such as Boston, MA, and Mineola, NY, are located near the coast.

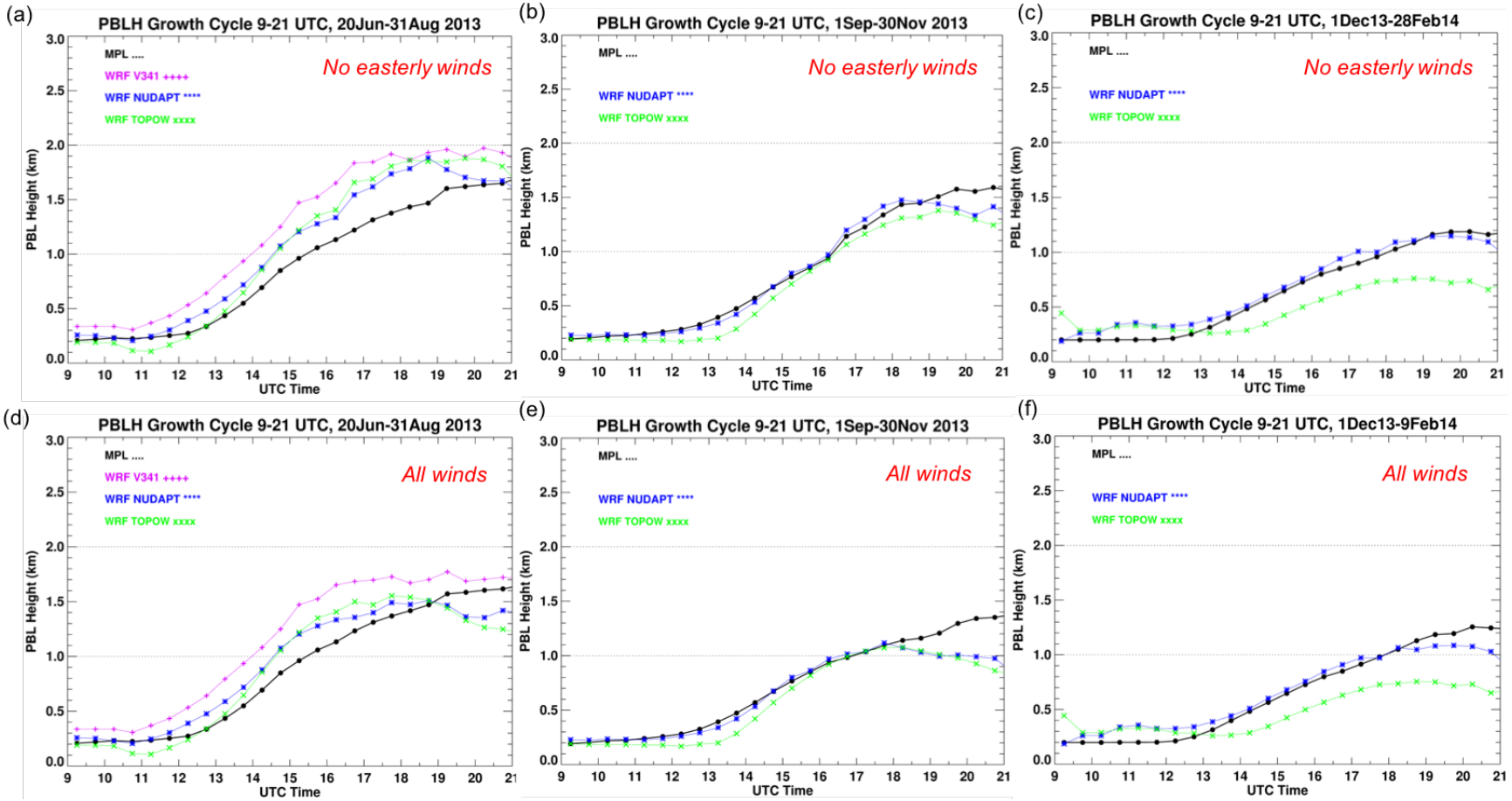

Figure 16. Three WRF versions BOSDC_NUDAPT (v.3.6.1) vs. BOSDC_TOPOW (v.3.6.1) and the older v3.4.1, with miniMPL-retrieved PBL heights from 9-21 UTC for three periods, with no easterly winds starting at 16 UTC (top panel) and all winds (bottom panel).

In the late afternoon, simulated WRF PBLH decayed more quickly than miniMPL-retrieved PBLHs in Boston, MA. This may be due to miniMPL data biasing the PBLH high, as enhanced NRB signals persist from aerosols that remain aloft once turbulent mixing is reduced and the RL begins to form shortly before sunset. However, we attempted to minimize this bias by limiting the peak PBLH to 100m below the RL in our image processing algorithm. Additionally, WRF simulations may overestimate the speed of the PBL collapse in the late afternoon. Results reported by Hegarty et al.[38] highlight that the PBLHs derived from 8pm local time radiosonde data often agreed with PBLH derived from standard MPL technology, while the WRF PBLHs were lower than both the MPL and radiosonde data (viz. their Figure 5). We also found similar results while comparing WRF BOSDC_NUDAPT to miniMPL-retrieved PBLH at our Mineola, NY, sampling site.

In the second phase of our comparison, we analyzed PBL simulations from two forecast models (WRF BOSDC_NUDAPT and WRF-ARW), two operational products (GDAS and NAM), and one reanalysis product (NARR) and compared with miniMPL-retrieved PBL heights from September 2013 through November 2014 for Boston. Results are shown in Figure 17 where, data are color coded by day of period, ending from fall to fall (in red orange). The two forecast models (WRF BOSDC_NUDAPT at 1.33 km and WRF ARW at 27 km) fell closest to the 1:1 line. The operational product NAM strongly deviates from the 1:1 line, when comparing PBL heights to miniMPL data: the forecast model, WRF ARW at 27 km, agrees better with the miniMPL data than the operational product, NAM at 12 km, in Boston. Overall, the WRF BOSDC_NUDAPT model (1.33 km resolution, MYJ PBL scheme) agreed the best with PBL heights retrieved from our image-recognition algorithm processing miniMPL data, followed by WRF ARW (see Figure 18).

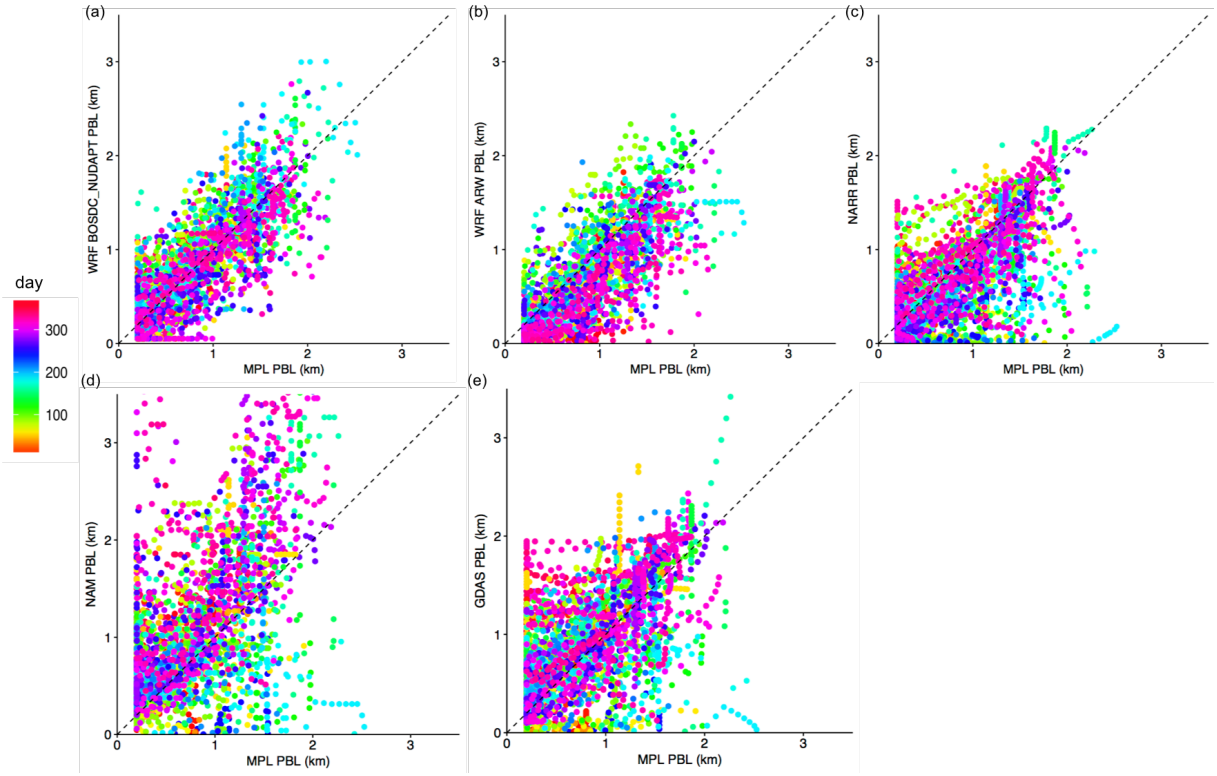

Figure 17. NWP PBL simulations versus miniMPL-retrieved PBLH for each day from 9-21 UTC in Boston, during our CMS study period (starting September 2013 and ending November 2014).

Figure 18 shows the mean percent errors (MPE) of PBLH for each NWP mode, by hour of the day during each season. Because the PBL has a strong diurnal cycle during well-mixed conditions, systematic errors in the NWP models caused errors in the PBLH diurnal cycle. Overall, the forecast models had small mean percent errors at all times. The operational and reanalysis products had large errors before the daytime PBLH develops (morning hours) and smaller errors after the daytime PBLH develops (afternoon hours). It is important to note, however, that the miniMPL unit may bias PBLH high in the morning hours if the nocturnal RL or PBL is being entrained. This potential bias was deemed likely to dissipate by midday, as all data were analyzed above 200 meters agl. The heights of the PBL were biased low during all seasons in NARR and WRF ARW (Figures 18h and 18i). PBLHs were biased low in the afternoon hours for all seasons in NARR, during spring in NAM, and during fall in WRF

BOSDC_NUDAPT (Figures 18f, 18g, and 18j). The WRF BOSDC_NUDAPT model produced the best overall agreement with the miniMPL diurnal cycle of PBLHs. Lastly, although the operational product from NAM shows the largest systematic errors overall, it less often showed a low bias in PBLH compared to the other models.

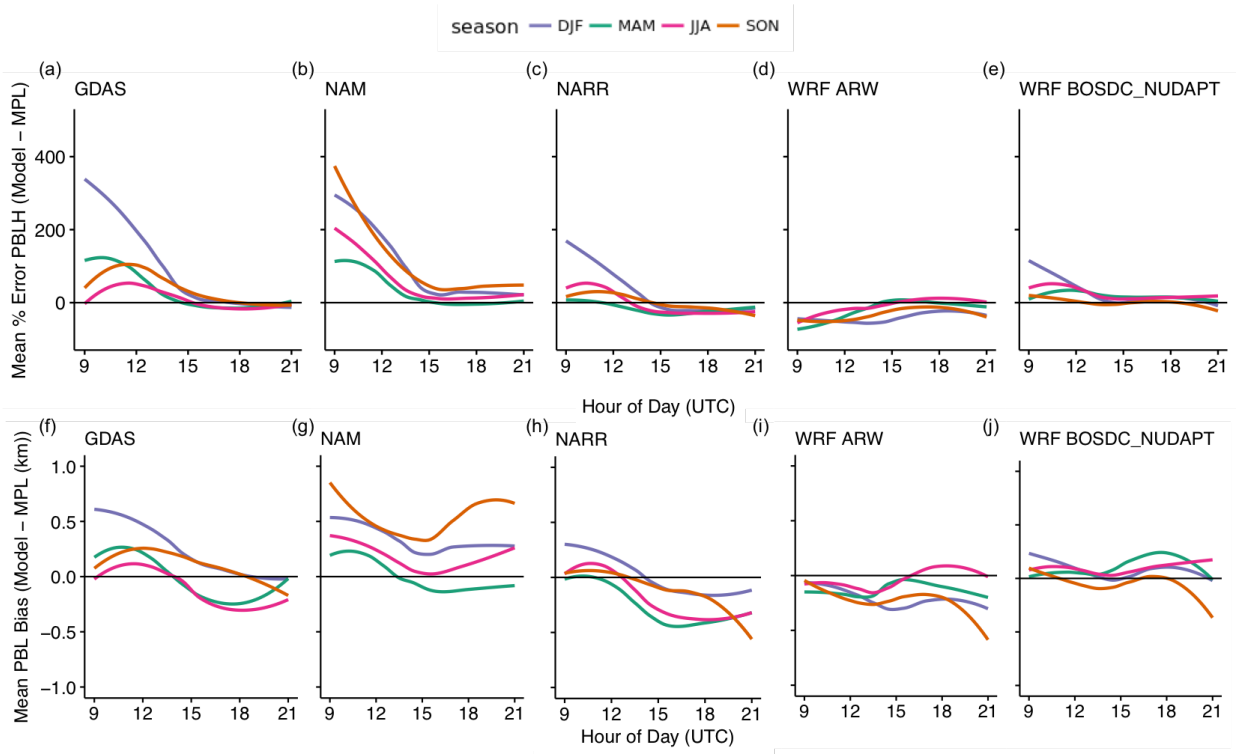

Figure 18. The PBL growth (9 - 21UTC) from NWP models as mean percent error (a-e) and bias (f-j), in comparison to the miniMPL measurements in Boston, MA from September 2013 to November 2014, for each metereological season: fall (Sept-Nov), winter (Dec-Feb), spring (Mar-May), and summer (June-Aug).

Inversion modeling studies often only use afternoon observations, when the PBL is well-developed and PBLH errors are expected to be smaller. To get a model evaluation metric applicable to these studies, we compared the daily maximum PBLH of the NWP models with the miniMPL. Figure 19 shows the mean bias and RMSE once the PBL is fully developed (daily

maximum PBLH) for each season. PBLH errors are strongly autocorrelated in time within each day (Figure 17 above). The forecast models performed the best, where WRF BOSDC_NUDAPT PBL simulations showed the best agreement in estimating the daily maximum PBLH throughout our study period (Table 2), with good correlation (R^2=0.72), RMSE of 0.424 km and relatively low bias of 0.128 km. WRF BOSDC_NUDAPT showed RMSE and bias similar in magnitude to those reported by other studies which evaluated WRF PBLH[41-44]. During the winter months, models either systematically underestimated (NARR, WRF-A2W) or overestimated (GDAS, NAM, WRF BOSDC_NUDAPT) the daily maximum PBLH (Figure 18a). All models systematically underestimated the time at which the fully developed PBL depth occurs in miniMPL data, with discrepancies from -0.469 to -1.735 hours.

Table 2. The daily maximum PBLH and time when the maximum PBLH occurred (NWP simulations vs. miniMPL retrievals), compared to miniMPL data at the Boston site.

NWP Model	Grid	Daily Maximum PBLH (NWP vs. MiniMPL)	Time of Daily Maximum PBLH (NWP vs. MiniMPL)
WRF BOSDC_NUDAPT	1.33 km	R^2= 0.72, RMSE= 0.424km, Bias= 0.128km	R^2= 0.80, RMSE= 2.82hr, Bias= -0.469hr
WRF ARW	27 km	R^2= 0.61, RMSE= 0.423km, Bias= -0.062km	R^2= 0.77, RMSE= 2.92hr, Bias= -0.485hr
NAM	12 km	R^2= 0.47, RMSE= 0.915km, Bias= 0.470km	R^2= 0.57, RMSE= 4.76hr, Bias= -1.735hr
NARR	27 km	R^2= 0.60, RMSE= 0.517km, Bias= -0.250km	R^2= 0.67, RMSE= 3.97hr, Bias= -1.556hr
GDAS	0.25 deg	R^2= 0.43, RMSE= 0.521km, Bias= 0.061km	R^2= 0.45, RMSE= 5.38hr, Bias= -1.429hr

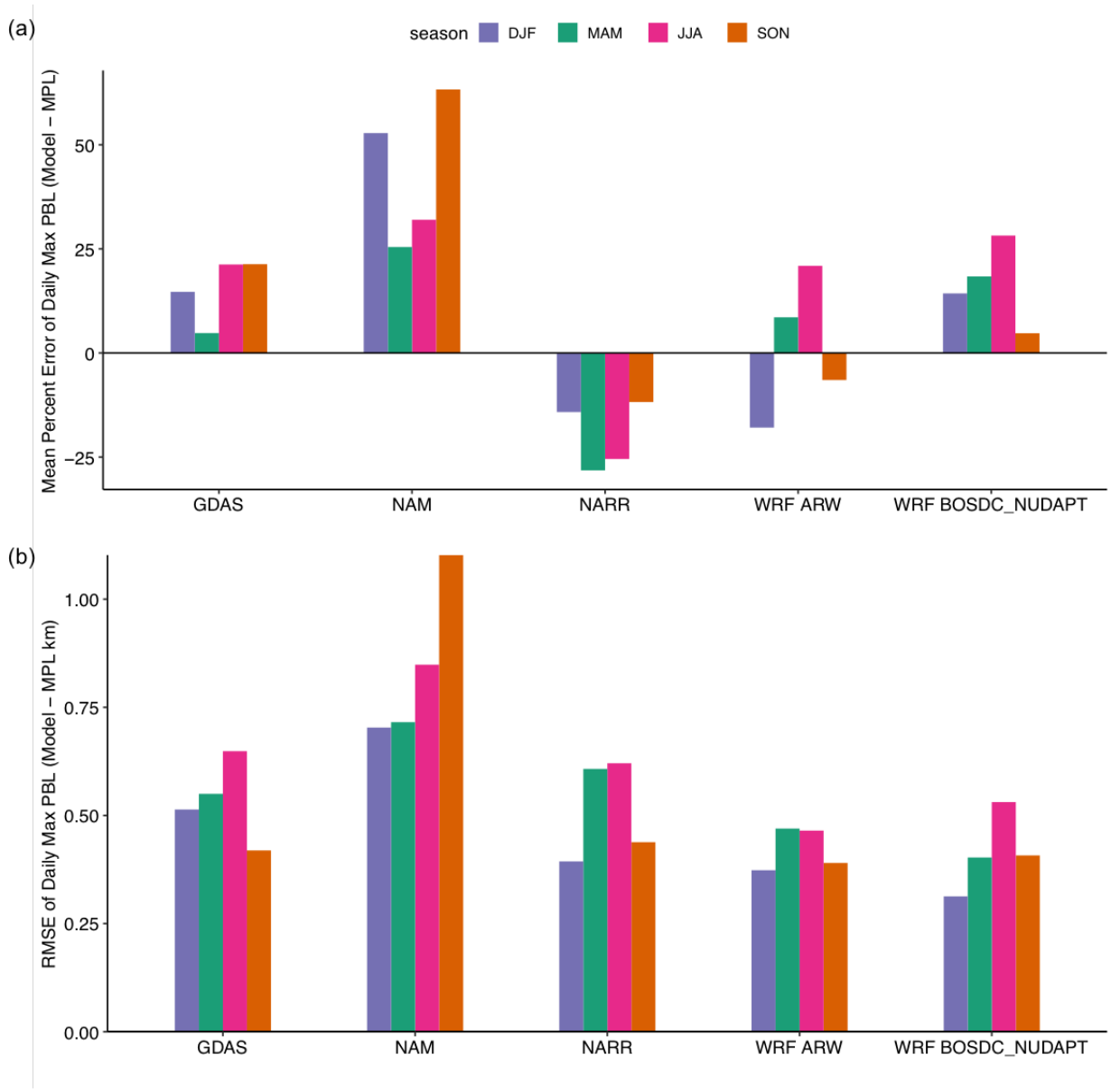

Figure 19. (a) Mean percent errors and (b) root mean square errors are shown for each NWP model in order to evaluate systematic errors of the fully developed PBL at our miniMPL sampling site in Boston, for four meteorological seasons: fall (Sept-Nov), winter (Dec-Mar), spring (Apr-May), and summer (Jun-Aug).

Seasonally, systematic errors varied for each NWP model and from one NWP model to another. In Table 3 below, results show that mean percent error was lowest for GDAS in the

spring, NAM in the spring, and NARR and both WRF models in the fall during the CMS study period. The bias remained the highest for the NAM model (-0.703 to 1.10 km) and lowest for WRF BOSDC_NUDAPT (0.313 to 0.531 km). Overall, NAM often overestimated the PBLH and NARR underestimated the PBLH in Boston. These results highlight the fact that that errors in PBL simulations vary from one season to another.

Table 3. The mean percent error in daily maximum PBLH (fully developed PBL) for each season, compared to miniMPL PBLH at the Boston site from September 2013 through November 2014.

Model	Season	Mean Error	RMSE
GDAS	DJF	14.7%	0.513 km
GDAS	MAM	4.79%	0.550 km
GDAS	JJA	21.3%	0.649 km
GDAS	SON	21.3%	0.419 km
NAM	DJF	52.8%	0.703 km
NAM	MAM	25.5%	0.715 km
NAM	JJA	32.0 %	0.848 km
NAM	SON	63.3 %	1.10 km
NARR	DJF	-14.2%	0.394 km
NARR	MAM	-28.2%	0.608 km
NARR	JJA	-25.5%	0.621 km
NARR	SON	-11.8%	0.438 km
WRF ARW	DJF	-17.9%	0.373 km
WRF ARW	MAM	8.57%	0.470 km
WRF ARW	JJA	20.9%	0.465 km
WRF ARW	SON	-6.50%	0.390 km
WRF BOSDC_NUDAPT	DJF	14.3%	0.313 km
WRF BOSDC_NUDAPT	MAM	18.4%	0.403 km
WRF BOSDC_NUDAPT	JJA	28.2%	0.531 km
WRF BOSDC_NUDAPT	SON	4.75%	0.407 km

Observations from our miniMPL lidar provided us with the capability to flag good from bad days when performing inversion modeling with any of these transport models. In Figure 20 below, scatter plots and correlation statistics of the daily maximum PBL heights (or fully developed PBL) simulated from NWP models and retrieved from miniMPL data in Boston are presented for each season of the CMS study period. Overall, the forecast models (WRF BOSDC_NUDAPT and WRF ARW) resulted in the most consistent agreement with the miniMPL daily maximum PBLH, followed by the reanalysis product (NARR) and the operational product (GDAS). The operational product from NAM disagreed with the miniMPL-retrieved daily maximum PBLH for most seasons, with the largest PBLH differences in the summer and fall seasons (Figure 20c). For each NWP model, the strongest correlation with miniMPL-retrieved daily maximum PBLH varies by season. WRF BOSDC_NUDAPT agreed best during the summer (R^2 = 0.77), WRF ARW (R^2 = 0.70) during the winter, NAM during the winter (R^2 = 0.67), NARR during the winter (R^2 = 0.73), and GDAS during the summer (R^2 = 0.62). Overall, the largest bias and mean error (RMSE) in daily maximum PBLH from NWP models occurred during the summer and fall months. The operational product from NAM biased the PBLH the most during our study CMS study period: 0.527 km in the winter, 0.213 km in the summer, 0.193 km in the spring, and the largest bias of 0.736 km in the fall. The operational product from GDAS and forecast model WRF BOSDC_NUDAPT, however, biased the daily maximum PBLH the least for all seasons.

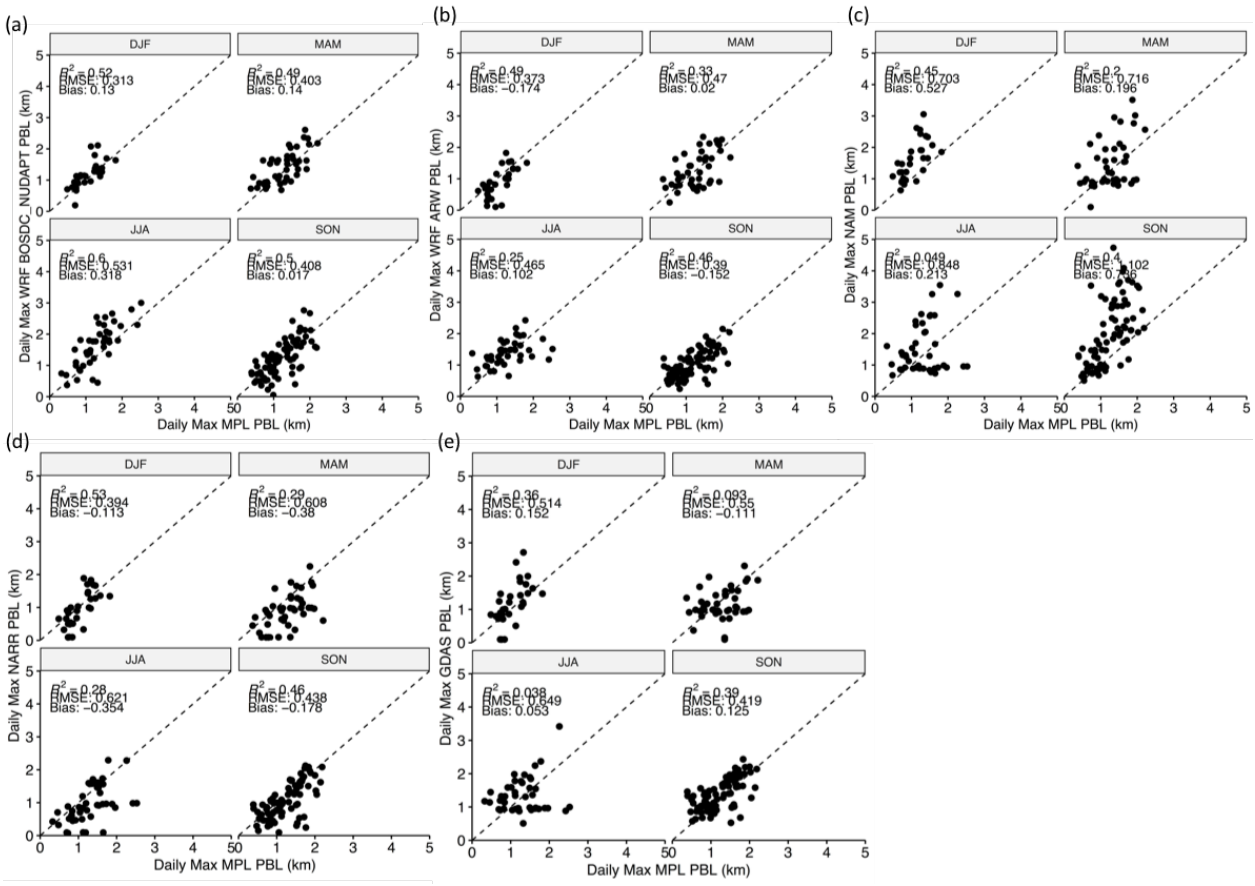

Figure 20. NWP vs. miniMPL daily maximum PBLH for the CMS study period in Boston.

Comparisons of NWP vs. miniMPL time (UTC) of daily maximum PBL height quantized to the nearest hour between the hours of 9-21 UTC for each season of our CMS study period are shown in Figure 21. The time of the daily maximum PBLH retrieved from the miniMPL data agreed the best with the forecast models (WRF BOSDC_NUDAPT and WRF ARW) for all seasons, with closest agreement during summer (R^2=0.87, R^2=0.84) and larger errors in winter (R^2=0.63, R^2=0.56). During the summer months, all NWP models agreed the best with the time at which the PBL is fully developed in the miniMPL measurements. The largest mean bias for the time of daily maximum PBLH occurred during the fall and spring months: -0.924UTC for WRF BOSDC_NUDAPT in the fall, -1.10UTC for WRF ARW in the fall, -2.42UTC for NAM in the spring, -1.93UTC for NARR in the spring, and -1.709 UTC for GDAS in the fall. Lastly, the

operational (NAM and GDAS) and reanalysis (NARR) products showed the largest mean errors in time of daily maximum PBLH. These results highlight that in NWP model simulations the fully developed PBL in Boston occurs too soon in comparison to the miniMPL data.

Any PBL scheme or model will vary seasonally and by location. However, various studies have shown that the YSU PBL scheme best simulated PBLHs in urban domains[36-37,39-40]. In the *Kretschemer et al., 2014*, study, the WRF YSU scheme produced the best correspondence of PBLHs with daytime radiosonde data resulting in a ~10% bias during the day, in comparison with the WRF MYJ scheme that resulted in a ~20% bias during the day. Our miniMPL-retrieved PBLHs, however, could not be compared against radiosonde data because the soundings are only at 00Z and 12Z, out of phase with the fully developed PBL (18Z to 21Z), and the closest sounding is 80 miles away in Chatham, Massachusetts and surrounded by the Atlantic Ocean. In that setting, the marine boundary layer can come in to play, making it more challenging to compare against the lidar-retrieved PBL height at our urban site. Alternatively, in collaboration with Thomas Nehrkorn at AER, we attempted to derive PBLH from the aircraft communications addressing and reporting system (ACARS) profiles at the Boston Logan International Airport. Unfortunately, this was not successful, as the sampling characteristics were too different from a true vertical profile to be useful (even when we just use the WRF-simulated values, interpolated to the times and locations of the ACARS observations, the derived WRF PBLH do not match those from WRF at the airport sites).

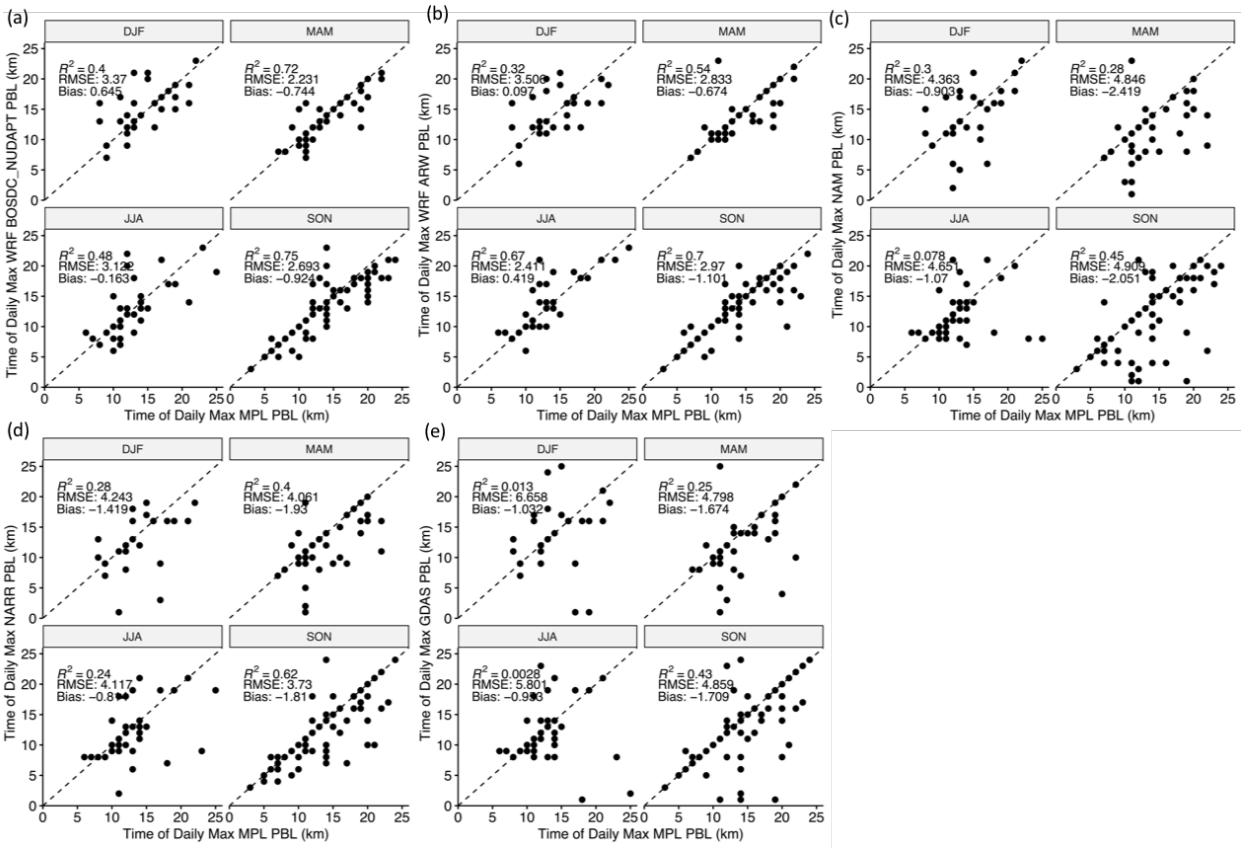

Figure 21. NWP vs. miniMPL time of daily maximum PBLH for the CMS study period in Boston.

Using lidar data to improve estimates of CO_2 fluxes using LPDMs in Boston, MA

In this study, we also compared the performance of two LPDM models, the STILT model coupled to WRF meteorological fields and the HYSPLIT model coupled to NAM meteorological fields that were used to estimate CO_2 fluxes in Boston[6]. The miniMPL data was used to better understand the impact of simulated PBLH on estimated CO_2 concentrations, as calculated by these two inverse model frameworks. As described in detail in *Sargent et al., 2018,* wind direction and local CO_2 flux were considered in determining background CO_2 concentrations. We used three background stations (Harvard Forest, MA, Martha's Vineyard, MA, and Canaan, NH), with wind directions within +/- 40^o angle of the station assigned to each

boundary site (shown in Figure 14). To account for changes in CO_2 with altitude, we created a vertically-resolved background curtain which combined the Picarro CO_2 measurements with eddy flux measurements and Carbon Tracker data. At the Harvard Forest site, eddy flux measurements were utilized to adjust measured CO_2 concentrations at 29 meters to their expected value at 200 m, the top of the surface layer. In our boundary curtain, CO_2 concentrations at Harvard Forest exponentially increased from the observed value at 29 meters to the flux-corrected PBL value between 29 and 200 meters. Above 200 m at all sites, we constructed CO_2 profiles using monthly mean vertical gradients from Carbon Tracker, adjusted to match the 200m value extrapolated from the 29 m data. The background curtain was thus pegged to observations at the surface to remove Carbon Tracker bias but utilized to account for changes with altitude. Particles released by our LPDM models at the urban sites exit the 90-km domain at a range of heights, typically from 200 magl to 700 magl. The boundary CO_2 concentration for each Lagrangian particle was then determined based on the altitude at which the particle exited the study region, and all particle contributions were averaged.

The forecast model WRF was coupled with STILT and the forecast model NAM coupled to HYSPLIT (run in "STILT" mode). Both were run backwards in time to give the adjoint (inverse) model. Both inverse models were combined with a prior high-resolution bottom-up CO_2 inventory[38] to estimate CO_2 fluxes in the Boston[6] area from enhanced (over background) concentrations observed at the surface and at 215m. The sum of modeled CO_2 enhancements in the urban core and concentrations at the boundary of the study region (90-km radius circle around Boston) were compared to observed CO_2 concentrations measured at our Boston miniMPL sampling location. These comparisons focused on afternoon hours, during which time the PBL is well-developed (Figure 18 shows significantly better NWP model PBLH performance from 16-21 UTC than from 9-16 UTC).

There were significant differences in the CO_2 enhancements calculated using the WRF-STILT and NAM-HYSPLIT frameworks. These differences were highly correlated with differences in PBLH between the two models. The CO_2 simulated by the models is much more sensitive to errors in PBLH when the PBL is low (<500m) than when the PBL is high (>800m) because the footprint and associated concentration enhancement are inversely proportional to PBLH. In Figures 18 and 19, the bias and errors of both WRF models were significantly lower than those of NAM. However, WRF ARW and BOSDC_NUDAPT simulations more often estimated the PBL height to be lower than 500m (51.7% and 33.7% of PBL simulations) than did NAM (26.4% of PBL simulations), giving rise to ourliers that strongly biased results. Other lidar studies used to evaluate PBL simulations from the WRF model using the YSU PBL scheme found low bias in PBLH also[3]. In Figure 22, CO_2 enhancements (CO_2 [urban] - CO_2 [background]) in Boston are shown for afternoon hours (11am-4pm EST) from November 2-16, 2014. The grey bars indicate the days on which lidar PBLH data was available. The blue and red lines show WRF-STILT and NAM-HYSPLIT model predictions and the black line, observed CO_2 enhancements. The red and blue dots indicate when the model PBL height was too low by 40% or more, as compared to the lidar-retrieved PBL height. These erroneously low model PBLHs produced very high CO_2 enhancements in the WRF-STILT framework that were not present in the NAM-HYSPLIT framework. Although NAM did not have the best overall agreement with miniMPL PBLH, it less often showed a low bias in PBLH, to which STILT and HYSPLIT are particularly sensitive. The lidar therefore enabled us to understand the source of unrealistic model CO_2 enhancements in WRF-STILT, demonstrating the relative advantages and disadvantages of the various models.

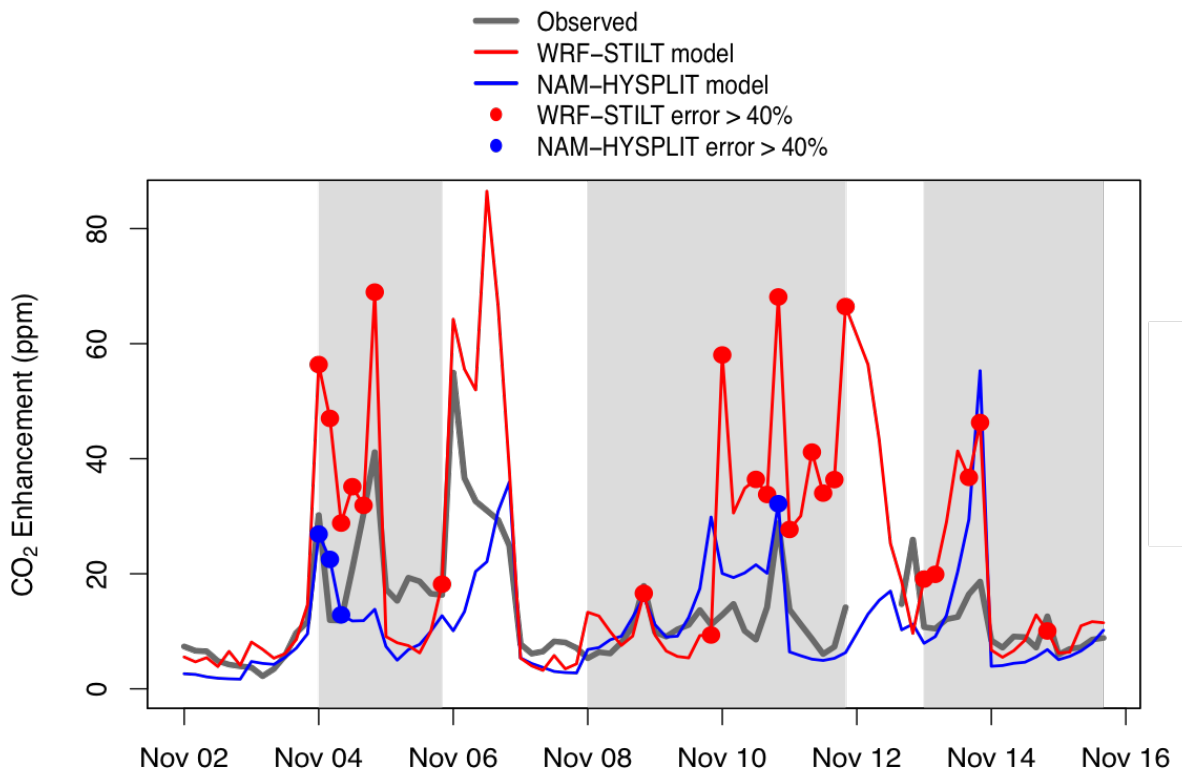

Figure 22. Enhancements (CO_2 [urban] - CO_2 [background]) of carbon dioxide in Boston for the afternoon hours (11am-4pm EST) during the period of November 2-16, 2014. The performance of the WRF-STILT model (red line) was evaluated against NAM-HYSPLIT model (blue line) where, the model PBL height was too low by 40% (blue and red dots). Anomalously high CO_2 concentrations were predicted by the WRF-STILT model when the PBL was too low due.

Chapter 3

Detecting and identifying transboundary air pollution within the nocturnal residual layer in Boston, MA

Often, a residual layer (RL), representing relict air from an earlier PBL, lies above the present PBL and below the free atmosphere[7-9]. In the evening, about 30 minutes before sunset, the surface cools; turbulence is reduced, and moisture and air pollutants from earlier in the day are trapped in this layer[18]. The RL is typically neutrally stratified, with potential temperature similar to the decayed PBL[53]. Air pollutants in the RL can be readily dispersed horizontally and, to some extent, vertcially[18]. The stable nocturnal PBL overlies the surface and accumulates emissions during the day and night[18]. It experiences weak and sporadic turbulence, and the thickness of the stable nocturnal PBL slowly adjusts with shallow, often thermally forced, circulations (e.g. the land breeze, in Boston). Since the winds in the RL are not affected by friction at the surface, winds can accelerate under horizontal pressure gradients, therefore, air pollutants trapped in the RL can move long distances[18, 54-55].

Inversion models are usually applied to estimate urban emissions based on ground-level air pollutant observations when the growth of the PBL is well underway (mid-morning hours) and when the PBL is well-developed, before turbulent mixing collapses (afternoon hours)[3,6,32]. In other words, inversion models often estimate ground-level air pollutant concentrations while the development of the PBL is well underway (mid-morning hours) and before turbulent mixing collapses (afternoon hours). The three major advantages for conducting inversions in the day during well-mixed PBL conditions are that transport errors are reduced[3,6]; entrainment fluxes are minimized[26], and air pollution emissions are the highest[56]. Inversion modeling studies are rarely focused at night. Local pollution accumulates close to the ground in the stable layer and long-range transport of pollution from distant sources lies overhead in the RL, from which can be entrained later on[3]. Few studies have focused on the RL[8,10-12] because it does not interact with

the surface (unless it is entrained in the PBL the next day) and there are very few measurements. As shown below, the miniMPL lidar provides a powerful new way to measure pollution transport in the nocturnal RL.

Evaluating air pollution that crosses political or jurisdictional boundaries (herein referred to as “transboundary”) is crucial to set emission reduction standards and implement effective environmental policies. The U.S. EPA has historically set air quality regulations to protect public health under the Clean Air Act (CAA), including assessment of regional air pollution. Most recently, New York and five other States sued the federal government in order to prompt the EPA to enforce the CAA “good neighbor” provision in the 2016 Cross State Air Pollution Rule (CSAPR). The “good neighbor” provision aims to control pollution emissions from upwind states, in order to protect the public from health effects caused by high ozone levels in downwind states. On August 21, 2018, the EPA proposed the “Affordable Clean Energy Rule” to replace the 2015 Clean Power Plan. This rule aims to shift the power from the federal government to states, in order to regulate their carbon dioxide emissions from power plant generators. By enabling older coal burning power plants to continue, or even increase power plant operations, this rule change will increase long-range transport of pollution.

Here we establish a framework and novel methodology to asses transboundary air pollution, using lidar observations of the nocturnal RL in Boston, Massachusetts. We primarily exploit the power of three tools: (1) information from STILT model footprints[51] along a vertical column, (2) miniMPL measurements, and (3) the high-resolution 1 km x 1 km Anthropogenic Carbon Emissions (ACES) inventory[52] developed by *Connor Gately et. al, 2017*. Each STILT footprint quantifies the sensitivity of simulated concentrations at each altitude at the receptor location to upwind emission sources[69]. Firstly, we estimated RL heights using lidar data and our image-recognition algorithm (discussed in Chapter 2) and from an analysis of vertical footprints

from the STILT model. Secondly, we identified transboundary air pollution episodes by detecting enhanced backscattering of light from aerosols in lidar data and investigating source regions influencing the air over our Boston sampling location using the STITL model. Thirdly, the influence of transboundary air pollution and the location of responsible sources were assessed by estimating mean atmospheric column CO_2 concentration enhancements at 10 receptor levels, by convolving STILT footprints with the ACES inventory. We estimate the influence of CO_2 emission sources located within northeastern states in Boston during the CMS study period from September 2013 to November 2014, using fossil-fuel derived CO_2 as an index for co-emitted pollutants. The column CO_2 enhancements have not been observed to date but could be readily obtained using solar viewing spectrometers[70-71].

Background

Air trapped within the RL is often entrained in the next day's growing PBL. If the RL contains pollutants from distance sources, pollutant concentrations on the ground can be affected. Several studies have shown that the convective boundary layer is coupled to the RL during entrainment processes[18,53,56-57,68]. These entrainment processes can either increase or decrease air pollution on the ground. Most commonly, studies have shown that ozone[20,20,59-63] and fine particulate matter[56,50-53] detected in the RL are be associated with an increase in concentration the next day in the PBL. However, for carbon dioxide, either an increase or decrease in CO_2 levels have been observed within the entrainment zone[26,67]. CO_2 levels can be lowered in the morning PBL due to the mixing of lower CO_2 levels from the RL and free atmosphere[26,67]. Formation of nocturnal low-level jets can also activate dynamical and chemical processes between the nocturnal PBL and RL that can increase pollution levels the next morning in the convective layer[54,64-68].

In the morning hours, incoming solar radiation may also trigger photochemical reactions in the RL forming reactive gases and aerosols[18-19]. A study conducted within the RL and free atmosphere domain, found higher aerosol number concentrations in the summer versus winter months that were associated with regional air masses and photochemical reactions, the effect of which was to increase the formation of secondary aerosols in the RL[56]. The RL aerosols can play a large role in increasing PM2.5 concentrations, up to 40% on the ground, in comparison to the upper half of the PBL (> 1100 meters) during mid-afternoon hours[64,52].

According to a recent analysis, almost 50% of fine particulate matter pollution in Boston is regional in origin[17], making Boston a prime study area for detecting and estimating transboundary air pollution. Additionally, we hypothesize a link between the vertical profile of backscattering of light from aerosols in lidar measurements and mean atmospheric column CO_2 concentrations. Measurements of CO_2 column concentrations from the ground are currently becoming feasible using very stable, compact instrumentation[70-71]. CO_2 is the primary GHG emitted from sources such as traffic and power plants and pollutant such as aerosols, nitrogen oxides (NOx), and hydrocarbons are co-emitted. *We hypothesize that lidar measurements of air pollution at night within the RL provide an effective means of detecting, and potentially quantifying, transboundary air pollution sources at a city or state level.*

Identifying and estimating the RL heights in the lidar data and the STILT model.

MiniMPL measurements at our Boston sampling location were utilized to estimate the residual layer heights (RLHs) during the CMS study period. In Chapter 1, the image processing steps to retrieve the RL from miniMPL data are described in detail. Wavelet filtering was primarily used in our image recognition algorithm to detect changes in NRB for each lidar profile. The wavelet filtered NRB profile for the entire day was then processed using image

thresholding, singular value decomposition, and fuzzy logic, with the aim of identifying our atmospheric structures of interest: the PBL and RL. In the afternoon, as the RL begins to form, the RL signal can blend with the PBL signal once the PBL is fully developed. Fuzzy logic was applied in our image-recognition algorithm, which limited the peak PBLH to about 100 meters below the RLH during the late afternoon hours. In Figure 23 below, the miniMPL NRB profile for June 1, 2013, is shown with the retrievals of PBLHs and RLHs using our image-recognition algorithm. The RLHs varied between roughly 1.5-2.1 km. Large backscattering signals were observed in the nocturnal RL early in the evening and again in the morning hours before sunrise. Our image-recognition algorithm proved to be robust for identifying the RL and aerosol loading in daily miniMPL profiles from 0-24 UTC.

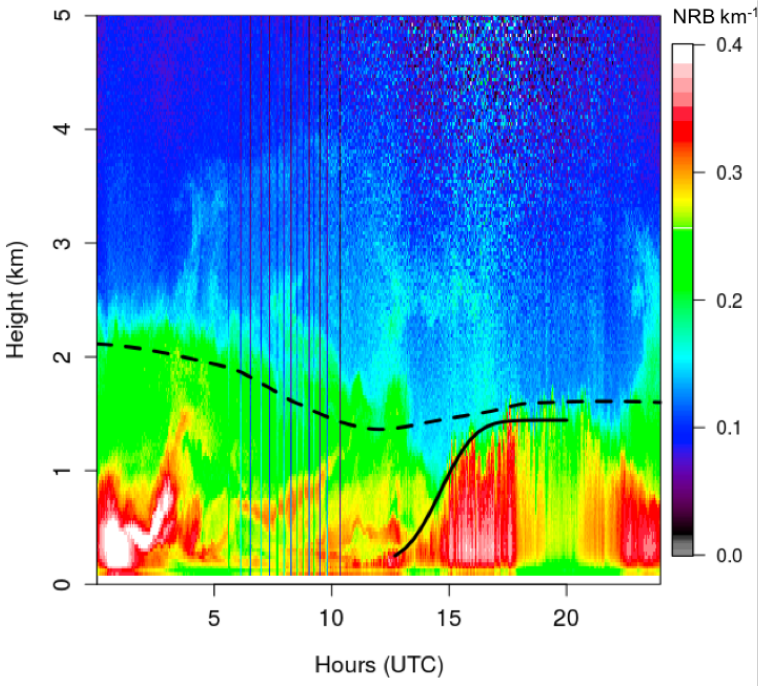

Figure 23. The miniMPL NRB profile for June 1, 2013, in Boston with retrieved PBL heights (solid black line) and RL heights (black dashed line) with the algorithm described in Chapter 1. Note periods of strong backscattering in the RL early in the evening (0-6 UTC) and early in the morning (10 – 12 UTC) (Local Standard Time = UTC – 5).

After retrieving RLHs from miniMPL data, we analyzed vertical footprints from the STILT-WRF model in order to verify that our inferred RL indeed represents the residual layer. NWP models often do not report the residual layer, as that requires very fine vertical resolution aloft near the RL in the model. No standard methodology exists for estimating the RL heights from NWP models. Therefore, we created a novel method using the coupled STILT-WRF model to identify the RL at our miniMPL sampling location in Boston, Massachusetts, to compare with the lidar. The Lagrangian particle dispersion model was set up to release an ensemble of 500 particles at 10 receptor heights above our Boston sampling site (279, 529, 779, 1029, 1529, 2029, 2529, 3029, 4029, and 5029 magl). Lagrangian particles were transported based on wind fields and PBL and urban parametrizations using the WRF BOSDC_NUDAPT configuration, which showed the strongest agreement with miniMPL-retrieved PBLH (see Chapter 2). In order to identify residual layer air over Boston, Lagrangian particles were released every 3 hours (0, 3, 6, 9, 12, 15, 18, and 21 UTC) and followed backwards in time for up to 72 hours, signifying 3-day “aged” air. The interaction of these Lagrangian particles with the surface was used to produce a footprint that quantifies the impact of upwind surface fluxes on changes in atmospheric concentration at the receptor.

We estimated the top of the RL as the height of the lowest receptor for which the sum of its footprints (over all map locations and back trajectory times in a 24-hour period) is near zero, i.e. the Lagrangian particles do not touch the ground in the first 24 hours and thus, the air at that height was above the previous day's (or “aged”) PBL. The “footnearfield1” product of the STILT model is the gridded footprint that aggregates particle footprints on lat/lon/time grid starting inside the highest resolution innermost grid (1.33 km x 1.33 km). These products were created by Thomas Nehrkorn and Jennifer Hegarty at Atmospheric Environmental Research (AER) for the NASA CMS study. These products were utilized to ascertain which periods of enhanced

NRB signals in miniMPL data (shown in Figure 23) were indicative of transboundary air pollution in Boston.

For example, a transboundary air pollution episode is detected on November 23, 2014, as can be seen by inspecting the enhanced backscattering signals in miniMPL data (Figure 24a) and running the STILT model, and by looking 24 hours backwards in time, starting at 6UTC and a receptor height of 1529 magl. The STILT model showed sensitivity to emission sources located in New York and Pennsylvania at our Boston sampling location (Figure 24c). Starting at a receptor height of 2029 magl, however, the footprint sum approaches zero (Figure 24d). An evaluation of all 10 receptor heights of the STILT footprints, showed that the footprint zeros out at approximately 2.0 km (Figure 24b) at night (0 UTC, 3 UTC, and 6 UTC), which indicates the top of the nocturnal RL and agrees with the lidar data for that time. The coupled WRF-STILT model accurately captures the isolation of RL by following where the Lagrangian particles no longer feel the influence of the surface, which can be considered to be in the free atmosphere.

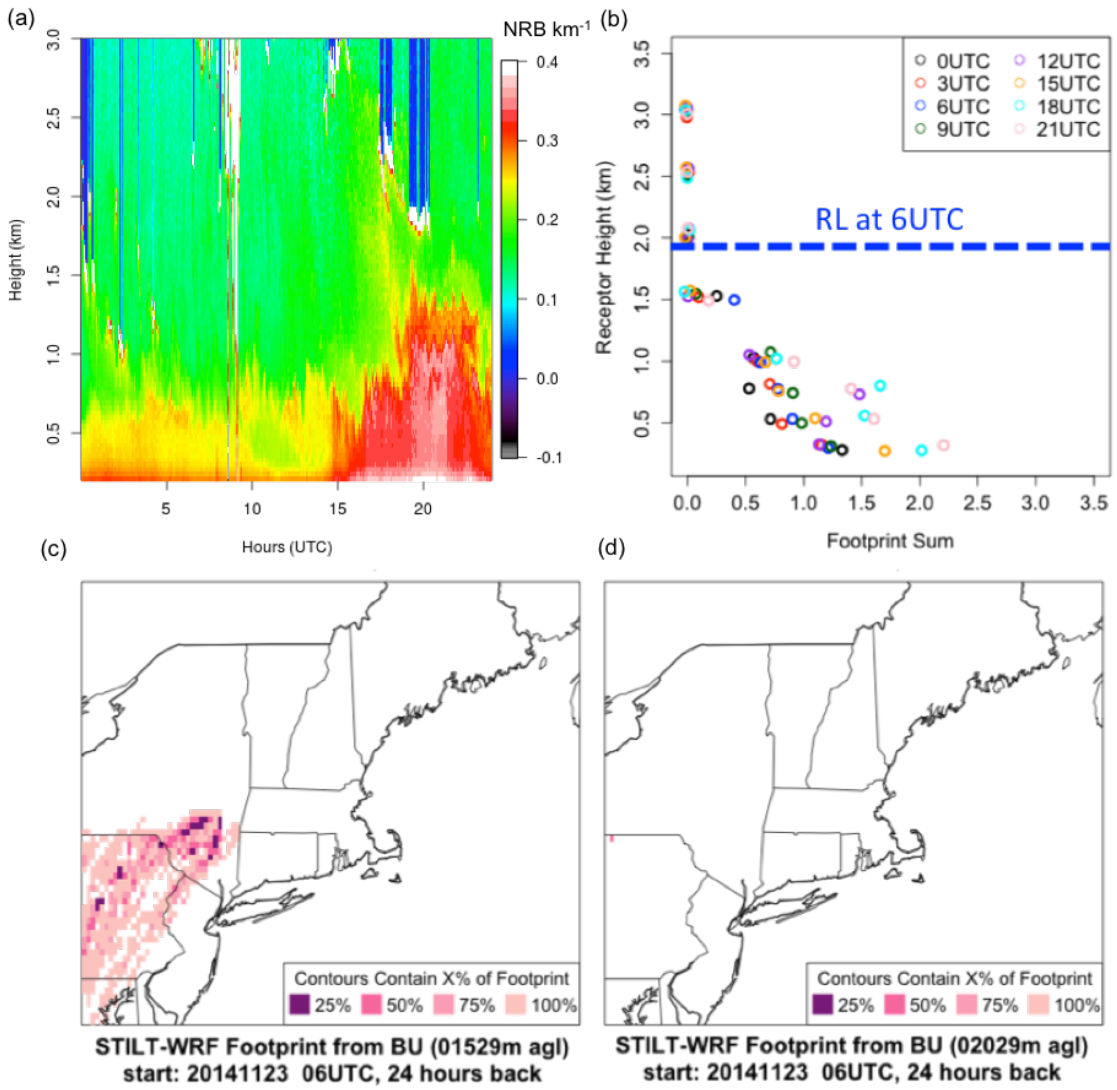

Figure 24. MiniMPL profile for November 23, 2014 (a) showing large backscattering signals throughout the night, STILT model footprints at receptor heights of 1529 magl (c) and 2020 magl (d) where, particles were released at 6 UTC from our miniMPL Boston sampling location, and the generalized RLH retrieved (b) from evaluating STILT footprints at 10 receptor levels at 6 UTC, within the nocturnal RL, where the foot sum zeros out (blue dashed line).

To verify the heights of the RL, the STILT-retrieved RLHs were compared with miniMPL-retrieved RLHs in Boston. Overall, we found strong agreement between STILT-retrieved and

miniMPL retrieved RLH. For example, a vertical footprint analysis using the product from STILT is shown in Figure 25b for September 25, 2012. This day is fairly complicated, as enhanced NRB signals (> 0.3) were detected throughout the night and day in the lidar profile (Figure 25a). The sum of the STILT footprints was plotted versus receptor height, followed 24 hours backwards in time, starting at 9, 3, 6, 9, 12, 15, and 21 UTC. By this approach, the top of the RL was identified between roughly 1.5 to 2.5 km where, the footprint sum goes to zero (mostly, around 2 km), indicating that the particles traveling backward in time did not touch the surface during the previous day. The miniMPL-retrieved RL height similarly varied between roughly 1.5 to 2.1 km. Results show the effectiveness of our method in identifying the RL using the STILT model. It is important to note, however, that the RL exhibits fluctuations throughout the day. Our STILT-retrieved RLH is generalized yet effective for evaluating air pollution within the RLH, as it separates the lower atmosphere from the free atmosphere and provides a secondary verification tool of RLHs retrieved from our miniMPL image-recognition algorithm.

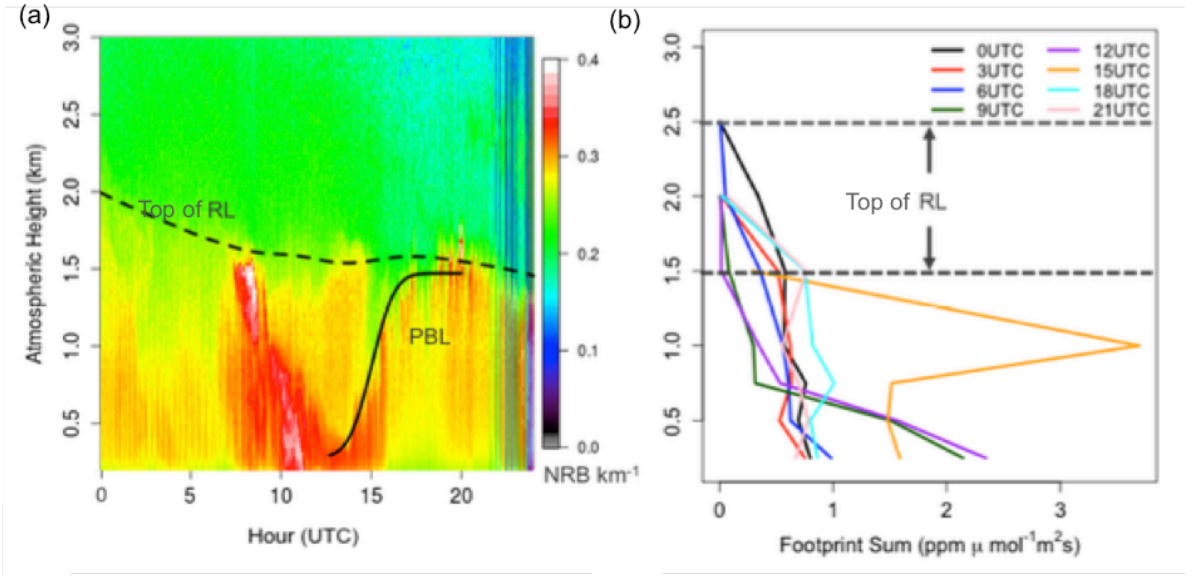

Figure 25. MiniMPL vs. STILT retrieved top of the RL in Boston for September 25, 2012. The top of the RLH varied from 1.5 to 2.0 km (dashed line) according to the lidar image-recognition

(Continued)

algorithm (a), and 1.5 to 2.5 km (dashed lines) according to the STILT model footprint sum analysis (b). Note that the RL extends to the surface during most hours.

Detecting transboundary air pollution episodes in lidar data.

In Boston, high aerosol backscatter in the nocturnal RL is very likely to be due to aerosols that originate regionally rather than locally[17]. If clouds or fog are present though, the miniMPL may detect large NRB signals that need to be distinguished from aerosol pollution. We visually screened NASA's GOES infrared imagery downloaded from the Plymouth State Weather Center at https://vortex.plymouth.edu. This infrared imagery is effective for cloud screening, as it measures the temperature of the ground (darker colors for warmer temperatures) and clouds (lighter colors for lower temperatures) in the infrared spectrum. This type of screening could readily be automated for long term measurements.

Large backscattering signals detected in cloud-screened lidar data were then investigated within the nocturnal RL in Boston. As an example, we show a notable transboundary air pollution episode detected within the nocturnal RL that persisted for nearly 5 days, between November 19th and 23rd, 2014. In Figure 26, 2 out of the 5 days are shown where, NRB signals (0.3 to 0.4 NRB km^{-1}) are present within the nocturnal RL. During the last day of the episode, on November 23, 2014, the largest enhancements in NRB data occur both at night within the RL and the next day within the PBL. Aerosols from both the nocturnal PBL and RL were entrained during the growth of the PBL and is illustrated at approximately 15 UTC on November 23, 2014.

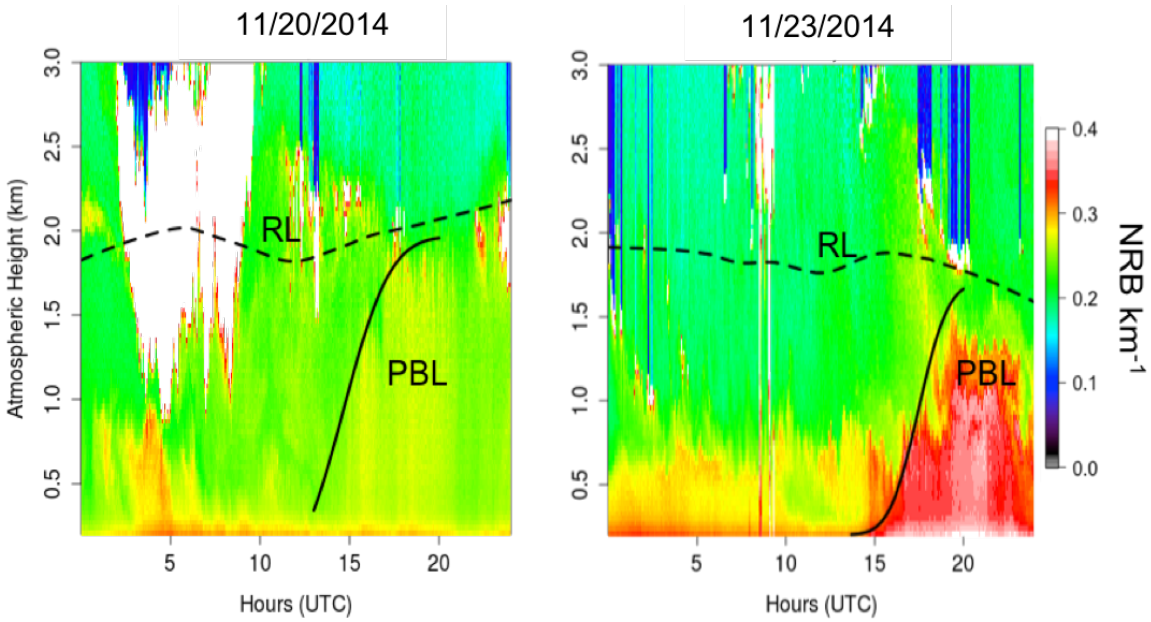

Figure 26. Lidar profiles for Nov 20th and 23rd, 2014, detecting enhancements (>0.3) at night.

To obtain a quantitative index of impacts of emission sources outside the Boston area, the CO_2 emissions from the ACES inventory were convolved with vertical STILT footprints at 10 receptor levels to compute the combustion-related CO_2 column enhancements. The ACES inventory provides estimates of annual and hourly CO_2 emissions from fossil fuel combustion at high-resolution (1 km x 1 km) from nine different sectors across 13 northeastern U.S. states. The states are as follows: Connecticut, Maine, Massachusetts, New Hampshire, Rhode Island, Vermont, New Jersey, New York, Pennsylvania, Delaware, Maryland, Virginia, and West Virginia. Emission sectors include residential, commercial, industrial, on-road, non-road mobile, marine, oil and gas, and rail sectors, and point sources, which includes electric power generation, industrial facilities, as well as aircraft take-off and landing operations. Since each footprint quantifies the sensitivity of simulated concentrations at each altitude at the receptor location to upwind emission sources[40], the resulting product is a vertical profile of CO_2 enhancements from emissions sources in northeastern U.S. at the Boston sampling location. The ACES-STILT products provide a temporal resolution on an hourly scale, which is important

since diurnally varying dynamical processes within the nocturnal and daytime PBL, as well as the RL, affect concentrations of CO_2 on the ground.

Figure 27 shows another example. On February 15, 2014, enhanced NRB signals (> 0.3) were detected within residual air at night at 6UTC in miniMPL data (Figure 27). These enhanced signals continued throughout the morning hours, including the period when the nocturnal PBL and RL are entrained in the growing PBL. Likely, air pollution from these entrainment processes affected ground-level air pollutant concentrations in Boston. In the service of further investigation, the STILT footprints at every receptor height or along the atmospheric column were summed and convolved with the ACES inventory 72 hours backwards in time, starting at 6UTC within the nocturnal RL at our Boston sampling location. A map of the emission sources regions and associated CO_2 enhancements for February 15th is shown below in Figure 28. The largest emission source regions (~3.0×10^{-5} ppm per km^2 grid cell) are located in New York where, natural gas and fuel oil no. 2 power plants are located near Lake Ontario and NYC. Additional CO_2 enhancements are attributed to traffic on Interstate 90 that extends from Boston to NYC and Interstate 95 from NYC to Philadelphia. During this transboundary air pollution episode, the elevated NRB signal represents emissions from nearly the entire Northeastern U.S. region located to the west and southwest of Boston. It is important to note that the enhanced NRB signals detected by the miniMPL sensor occur below ~0.8km and thus, within the nocturnal RL and possibly within the nocturnal PBL in Boston.

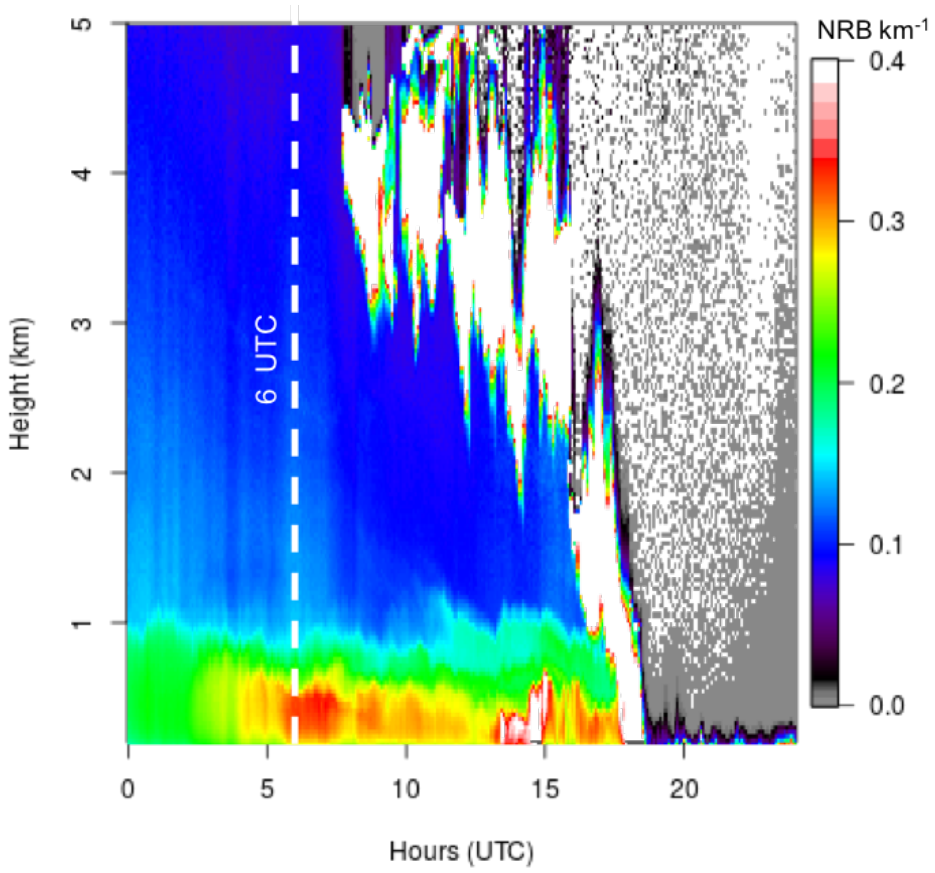

Figure 27. Large NRB enhancements (>0.3) detected in miniMPL measurements within the nocturnal RL at 6UTC (white dashed line) in Boston on February 15, 2014. The vertical NRB profile is attenuated in the lower part of the atmosphere due to low-lying clouds at approximately 17 UTC.

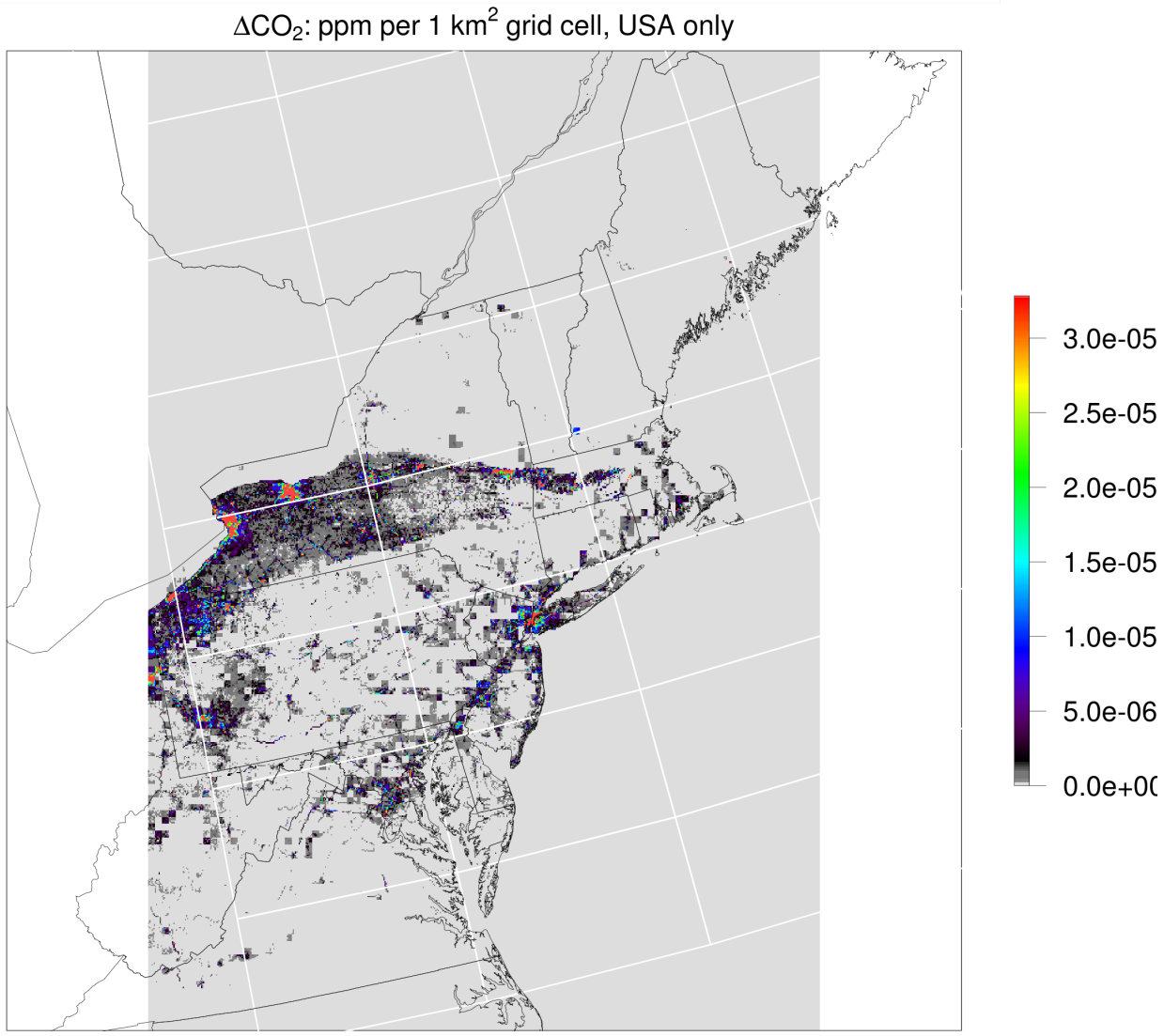

Figure 28. Contributions from upwind sources to the pressure-weighted column mean CO_2 enhancements (ppm) based on ACES-STILT for February 15, 2014, 72 hours backwards in time starting at 6UTC from the Boston site.

Using lidar NRB signals and the ACES-STILT framework, as in the above examples, we examined data from five months in 2014, including February, May, July, September, and November. Each month represents a meteorological season and for each month, transboundary air pollution was assessed using the ACES-STILT framework. Transboundary air pollution was assessed using carbon dioxide as a tracer and an index of pollution influence.

We computed column CO_2 enhancements at the Boston sampling location for each day where, enhanced NRB signals were detected in lidar profiles within the nocturnal RL (see Appendix Tables A1, A2, and A3 for a list of detected transboundary air pollution episodes). An example of one transboundary air pollution episode for each meteorological season using lidar profiles is included in the Appendix (Figures A11, A13, and A15), along with a map of emission sources contributing to CO_2 enhancements estimated using the ACES-STILT framework (Appendix Figures A12, A14, and A16). Where large NRB signals (> 0.3) were identified in lidar profiles at 6UTC, we estimated the total contribution of CO_2 enhancement from each northeastern state (pressure-weighted in parts per million (ppm)). The largest CO_2 enhancements occurred in the winter and summer. In the February 2014, northern states such as Maine, Vermont, and New Hampshire showed the largest influence (CO_2 enhancements) at our Boston sampling location (Table 4). In July 2014, emission sources located in New York and Pennsylvania showed the largest influence. The enhanced backscattering signals measured by the lidar in these time periods support the view that aerosol pollution may be associated with the estimated CO_2 enhancements in Boston.

Table 4. Winter 2014 transboundary air pollution episodes detected within the nocturnal RL by evaluating lidar NRB signals and ACES-STILT CO_2 enhancement (ppm) in Boston.

Winter 2014 Atmospheric Column Average of CO_2 Enhancements (ppm) by State in Northeastern U.S.

ACES –STILT, 72 hours backwards in time starting at 6UTC

Date	NRB	MA	ME	VT	NH	NY	PA	MD	VA	WV	DE	CT	RI	NJ	DC
Feb 4	>0.3	3.24e-03	7.04e-02	2.63e-03	1.75e-02	9.27e-03	4.89e-04	0.00	0.00	0.00	0.00	3.17e-05	0.00	0.00	0.00
Feb 15	>0.3	3.36e-01	5.06e-04	5.65e-04	1.19e-03	4.08e-01	1.67e-01	1.74e-02	9.98e-03	1.24e-02	6.74e-03	8.09e-03	1.55e-03	3.70e-02	1.13e-03
Feb 18	>0.3	3.57e-01	4.98e-04	7.12e-03	6.84e-02	5.93e-05	0.00	0.00	0.00	0.00	0.00	0.00	0.00	0.00	0.00
Feb 19	>0.3	2.34e-02	0.00	1.15e-02	5.31e-03	8.63e-02	1.01e-01	9.61e-03	8.18e-03	2.27e-02	8.03e-05	2.22e-03	7.43e-04	1.97e-03	7.70e-05
Feb 20	>0.3	6.64e-02	0.00	3.8e-02	4.36e-02	1.93e-01	1.71e-01	2.92e-01	1.46e-02	1.16e-02	2.71e-03	2.09e-02	4.75e-03	3.97e-02	5.41e-04

Assessing transboundary air pollution in Boston using the ACES-STILT framework.

After investigating for transboundary air pollution in lidar measurements, the ACES-STILT framework was used to explore the impact of emission sources from states within the northeastern U.S., throughout the atmospheric column in Boston. In Figure 29, CO_2 enhancements (ΔCO_2) from each state are plotted against atmospheric height (Z) in meters above ground level for particle releases starting at 0, 3, 6, 9, and 12 UTC, for 72 hours backwards in time, for an example day July 23, 2014. Results show that during the night (0, 3, 6, and 9 UTC), most of the CO_2 enhancements originate from emission source regions in Pennsylvania, New York, New Jersey, and Massachusetts. Depending on the state, enhancements peaked at various heights in the atmospheric column. For example, Pennsylvania's ΔCO_2 peaked at approximately 2.4 ppm at 2029 magl and at 12UTC, at approximately 3.1 ppm at 1529 magl at 6UTC within the nocturnal RL. New York peaked both at lower (279 magl) and higher (2029 magl) atmospheric heights whereas, New Jersey and Massachusetts CO_2 enhancements peaked at lower atmospheric heights (< 529 magl). This result is not surprising as states located further away from Boston, such as Pennsylvania, showed larger enhancements at higher altitudes (> 1029 magl). The further away the emission sources are, the higher in the atmosphere a signal can be detected within the nocturnal RL in Boston. The nocturnal RL is later entrained with the nocturnal PBL during the growth of the PBL next day, influencing air quality on the ground.

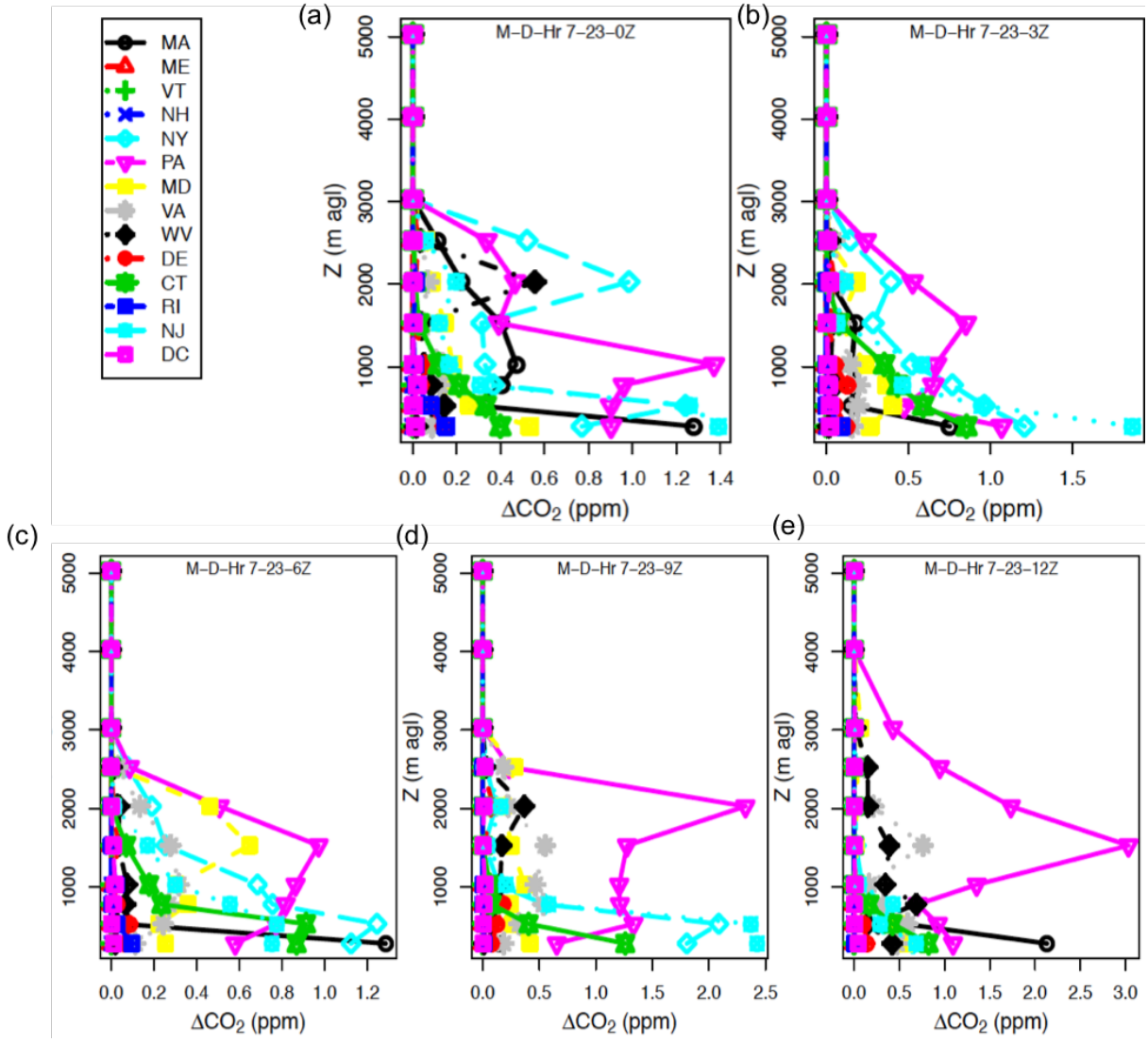

Figure 29. ACES-STILT CO_2 enhancement (ppm) by northeastern state vs. height (magl) for November 23, 2014, starting at 0 UTC (a), 3 UTC (b), 6 UTC (c), 9 UTC (d), and 12 UTC (e) at each receptor height in Boston.

In order to test our hypothesis that the nocturnal RL is more important for transporting air pollution at night, we conducted transboundary air pollution analyses at night (6 UTC) and day (18 UTC) during well-mixed conditions in the PBL. In July 2014, Virginia, New York, Pennsylvania, and Connecticut mostly influence CO_2 concentrations at our Boston sampling

location at night within the nocturnal RL (see Figure 30). In the day (18 UTC), by contrast, combustion CO_2 enhancements are primarily influenced by local emissions in Boston or within Massachusetts (Figure 31). For example, in July 2014, the mean column ΔCO_2 at 6 UTC from New York (0.170 ppm) and Pennsylvania (0.167 ppm) are higher than Massachusetts (0.117 ppm) at our Boston sampling location. Since inversion modeling studies are typically performed during well-mixed conditions in the PBL (18 UTC), it is very likely that regional pollution influence is missed, being relegated to the "background" influence.

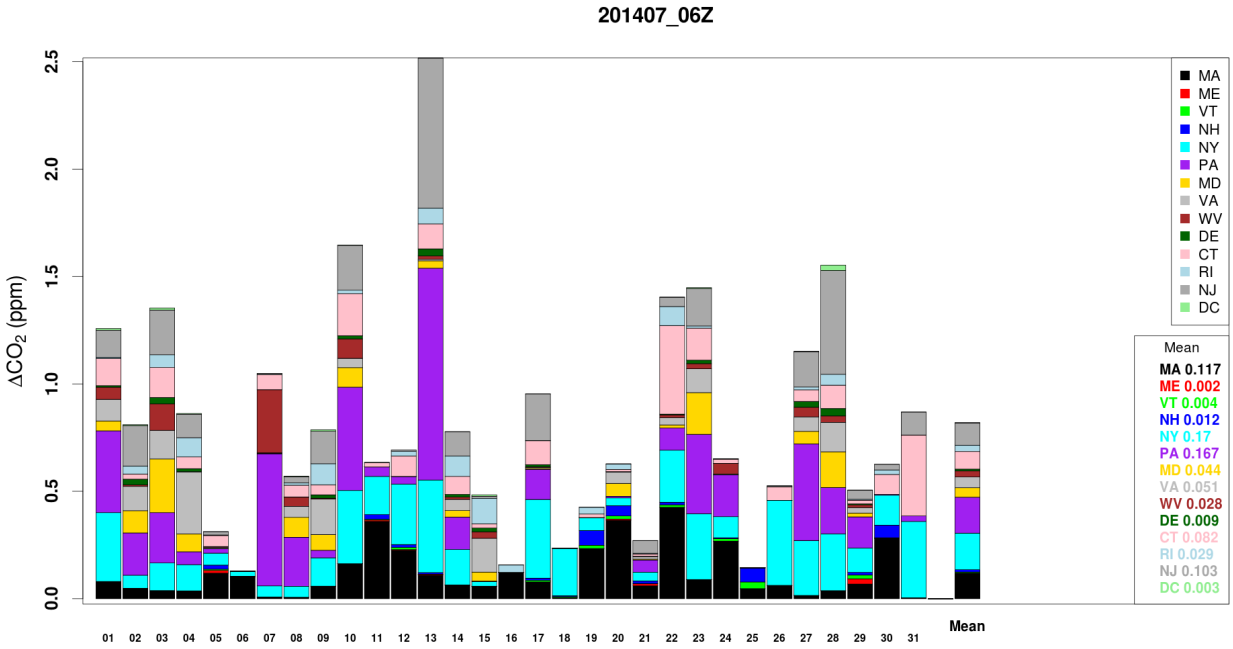

Figure 30. Nighttime (06Z) mean column CO_2 enhancement (ppm) contributions by state for July 2014 using ACES-STILT at our Boston sampling location. Note the dominance of transboundary pollution sources versus local emissions on most days. These are pressure-weighted mean contributions to the total column, both daily and monthly, as contrasted to the concentration enhancements at altitude, which are usually larger for the more distance sources.

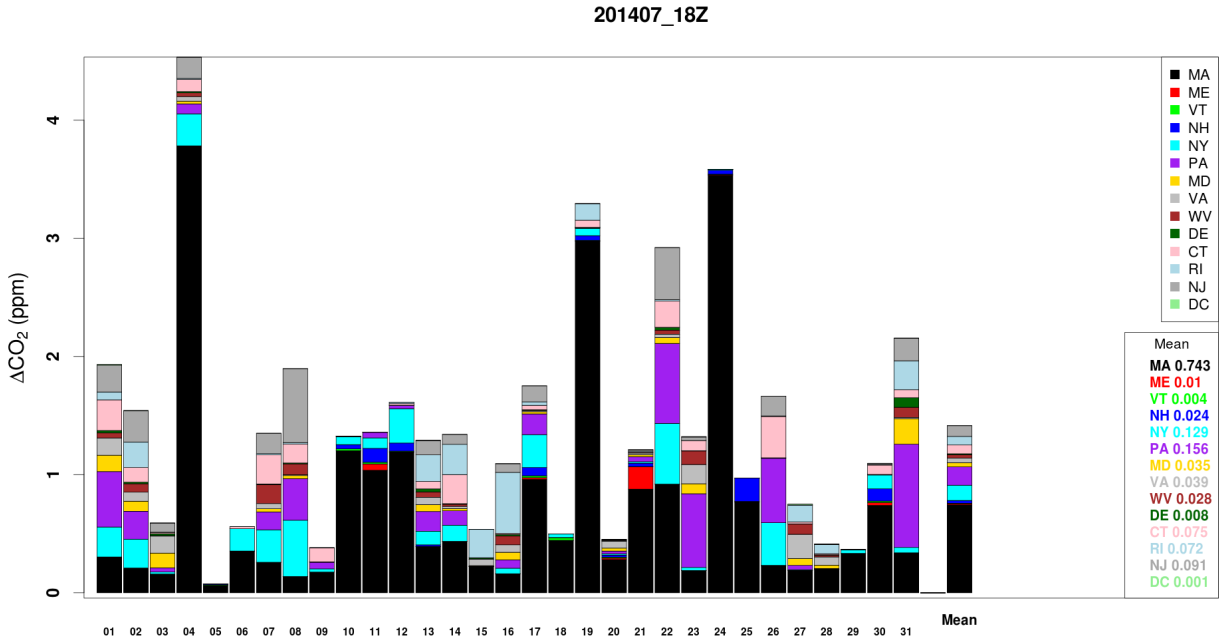

Figure 31. Midday mean column CO_2 enhancement (ppm) contributions by state for July 2014 using ACES-STILT starting at 18 UTC at our Boston sampling location. Note the dominace of local emission sources on most days, in contrast to nighttime findings. But transboundary air pollution is still significant midday.

Attempting to verify our results with additional observations, we also compared the pressure-weighted mean column CO_2 enhancements from ACES-STILT against CO_2 observations at the Copley station during an episode detected in miniMPL measurements on July 22nd and 23rd, 2014. The Copley station is approximately 215 magl and at times, is expected to be higher than the nocturnal PBL which is influenced by local surface emissions. However, due to the urban heat island effect, which increases the PBL "dome", and to the influence of the building structure, the Copley station data show high ΔCO_2 values indicating that it is in fact be coupled to the surface at night. For example, in Figure 32, at 6 UTC the anthropogenic CO_2 enhancement is about 7ppm (top panel) and observed CO_2 concentrations at the Copley station is about 387ppm (bottom panel). On July 23, 2014, when evaluating the

evening and night hours from 0 to 12 UTC, the ACES-STILT retrieved CO_2 enhancements increase by about 1-2ppm, mostly from out of state, but the CO_2 concentrations observed at Copley Station increased by about 22pm. We infer that the total column measurements or aircraft data, rather than data from a tall building, are needed to measure transboundary air pollution influence on CO_2 at night at the Copley sampling site.

Enhanced NRB signals (>0.3) were detected in miniMPL at our Boston sampling location during a transboundary air pollution episode in July 22nd and 23rd of 2014 (Figure 33). Our ACES-STILT analysis, as northeastern states contributed to approximately 85.7% of mean column CO_2 enhancements in Massachusetts within the nocturnal RL at 6 UTC (see Figure 30 above). ACES-STILT indicates that regional air pollution dominated the nighttime signal in Boston, resulting in incorporation of the co-emitted pollutants such as particulate matter into ground-level air pollution the next day. Note that the backscattering signals of aerosol loadings in miniMPL data during this transboundary air pollution episode extends from the surface to the top of the RL. In addition, even larger backscattering signals (NRB ~ 0.4) are seen at 12 UTC on July 22nd. This signal is occurring during the entrainment zone, when pollution from both the nocturnal RL and PBL are entrained in the growing PBL.

Total column CO_2, CO, and CH_4 measurements are now being routinely made in Boston using an EM27/Sun Spectrometer. In the future, these measurements combined with lidar data should allow us to quantitively link CO_2 and co-emitted air pollutants from distant sources to air quality in the city. Additionally, using CO_2 concentrations from the NOAA Tall Tower Network that samples the air above ~300-400 meters can help test our new methodology using lidar and the ACES-STILT framework, as well as providing a vertical profile of background CO_2 concentrations.

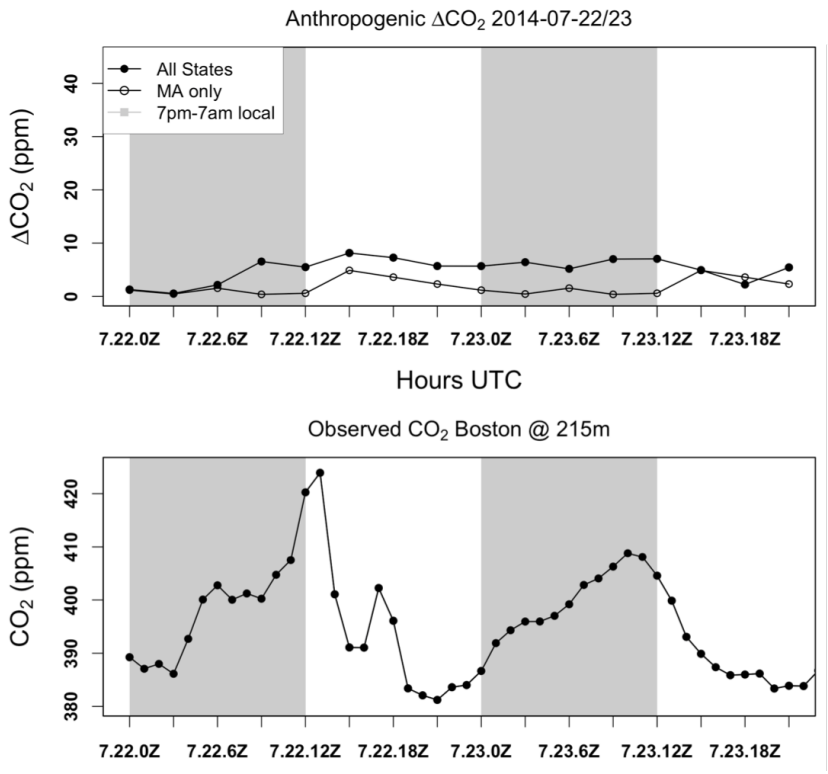

Figure 32. Observed CO_2 concentrations at Copley station (215 magl) and enhancements from northeastern states using ACES-STILT at the lowest level (279 magl) from July 22-23, 2014.

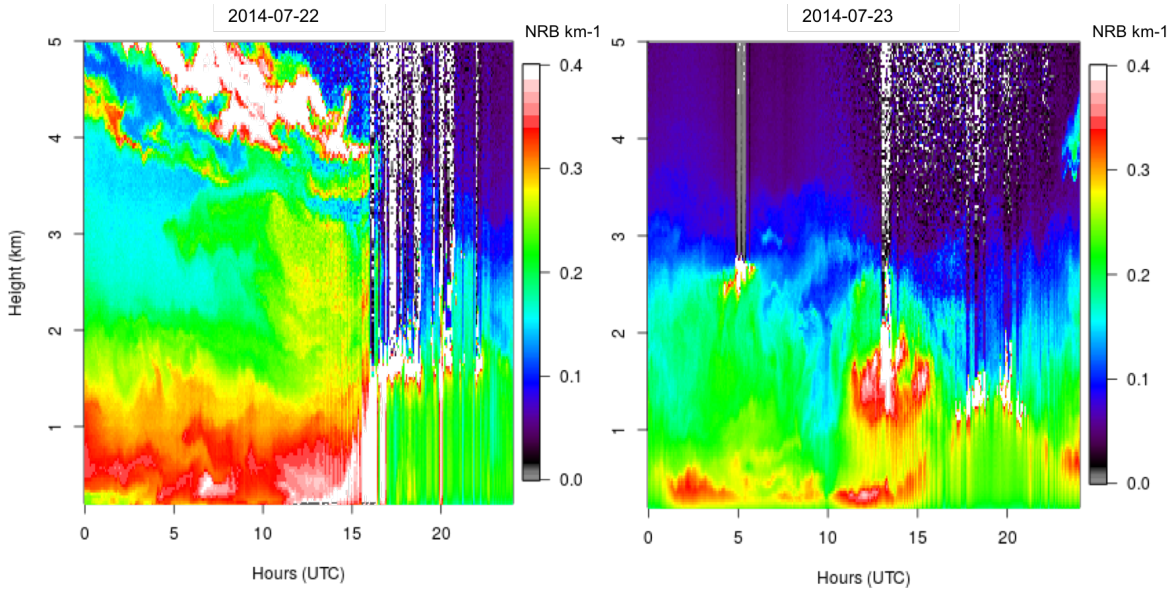

Figure 33. Lidar NRB profiles for July 22 and 23, 2014, detecting large NRB (> 0.3) in the nocturnal RL over Boston.

Using our ACES-STILT framework, we found that Maine and Connecticut often influenced CO_2 enhancements observed at our Boston sampling location in the winter. This was primarily due to emissions from wood burning for heating (Figure 34) and often these emissions include co-pollutants that includes aerosols and toxic air contaminants. Enhancements of CO_2 from New York and Pennsylvania were nearly equally to Massachusetts at night where, the column mean is approximately 0.114 ppm for NY, 0.102 ppm for PA, and 0.111 ppm for MA, emphasizing the impact of regional emission sources in Boston. Studying the air within the nocturnal RL (6 UTC) provides a clear signal of Boston's "nearest neighbors" contribution to air pollution levels in the city.

In the wintertime, signals of regional air pollution are still detected during the daytime but are mixed with larger local signals of air pollution than the summertime, according to our ACES-STILT framework. For example, in February of 2014, CO_2 enhancements originating from NY slightly increased to 0.133 ppm and enhancements slightly decreased for PA to 0.073ppm in comparison to nighttime (Figure 35). In the winter, northern states such as Vermont, Maine, and New Hampshire, show an increase in CO_2 enhancements in Boston, in comparison to July 2014. This result indicates the importance of tracking transboundary air pollution in cities at night, within the nocturnal RL, as emissions source regions may be contributing to pollution levels the next day due to entrainment processes.

Overall, northeastern states contributed to approximately 76.2% of pressure-weighted mean column CO_2 enhancements in Massachusetts within the nocturnal RL at 6 UTC using the ACES-STILT analysis. However, during midday Massachusetts dominates the enhancement (ΔCO_2) signals in Boston. This result further reinforces that regional air pollution is a major

influence in Boston's air quality and that conducting inversion studies should not be limited to the daytime, as the night provides a clearer signal when evaluating the nocturnal RL.

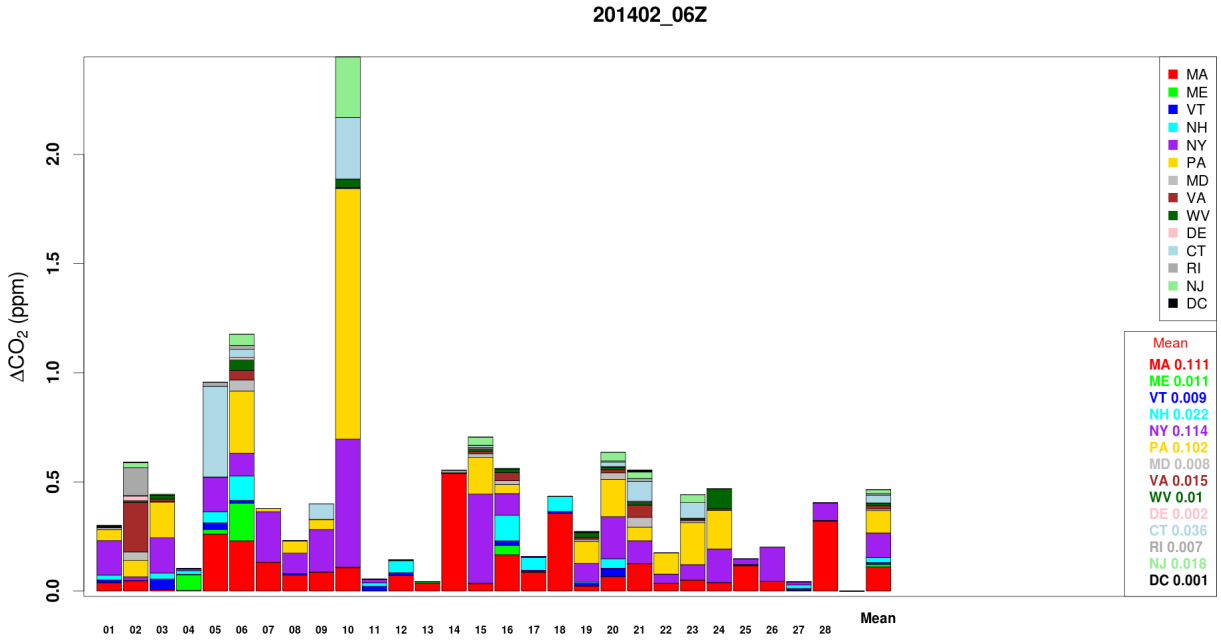

Figure 34. Nighttime mean column CO_2 enhancement (ppm) contributions by state for February 2014 using ACES-STILT starting at 6 UTC at our Boston sampling location.

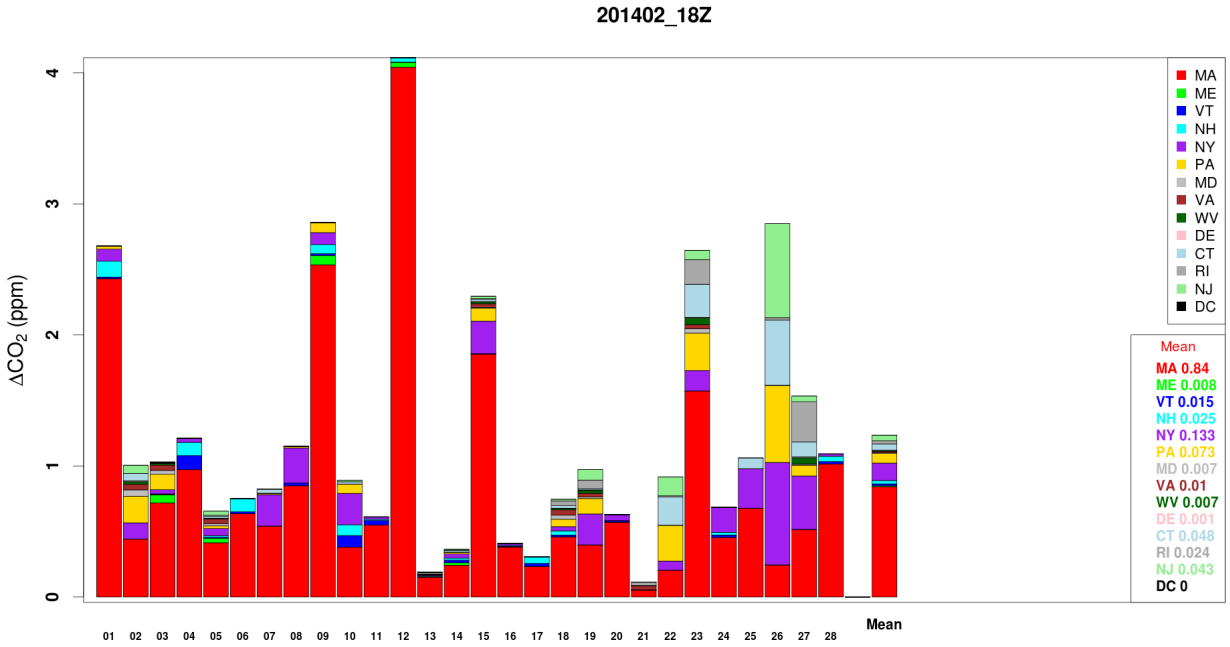

Figure 35. Midday mean column CO_2 enhancement (ppm) contributions by state for February 2014 using ACES-STILT starting at 18 UTC at our Boston sampling location.

We also found that the pressure-weighted mean column CO_2 enhancements from outside of Massachusetts were lowest in the spring (May 2014) and fall (September and November 2014) using our ACES-STILT analysis within the nocturnal RL. Result are shown in Figures 36-38 below. Yet Pennsylvania and New York most consistently showed the largest contributions to mean column CO_2 enhancements at our Boston sampling location. Regional air pollution remains a key contributor to pollution levels in Boston's air at night. Aside from traffic, emissions sources in these sates include oil and gas power plants and coal combustion and thus, co-pollutants such as aerosols and toxic air contaminants may be transported and dispersed over a 72-hour period and identified using CO_2 as a tracer in our ACES-STILT framework. As outside temperatures drop in the fall months, larger contributions from northern states like New Hampshire, Vermont, and Maine are expected. However, our results (Figures 38

and 39) do not detect a significant difference at our Boston sampling location, when using our ACES-STILT methodology.

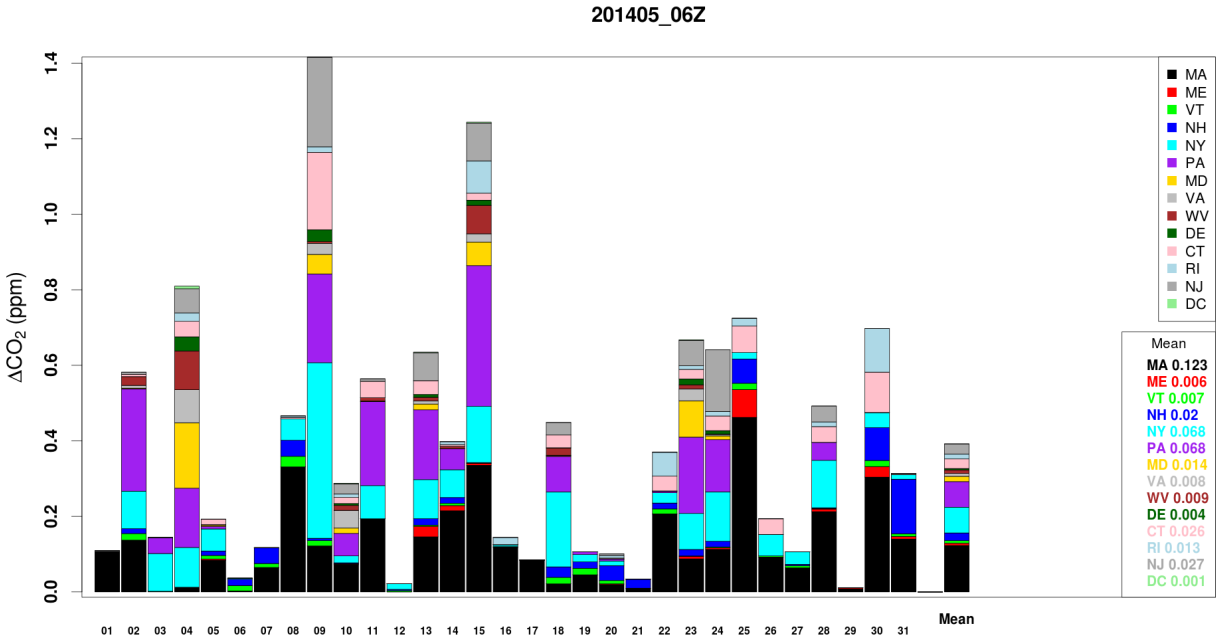

Figure 36. Nighttime mean column CO_2 enhancement (ppm) contributions by state for May 2014 using ACES-STILT staring at 6UTC from our Boston sampling location.

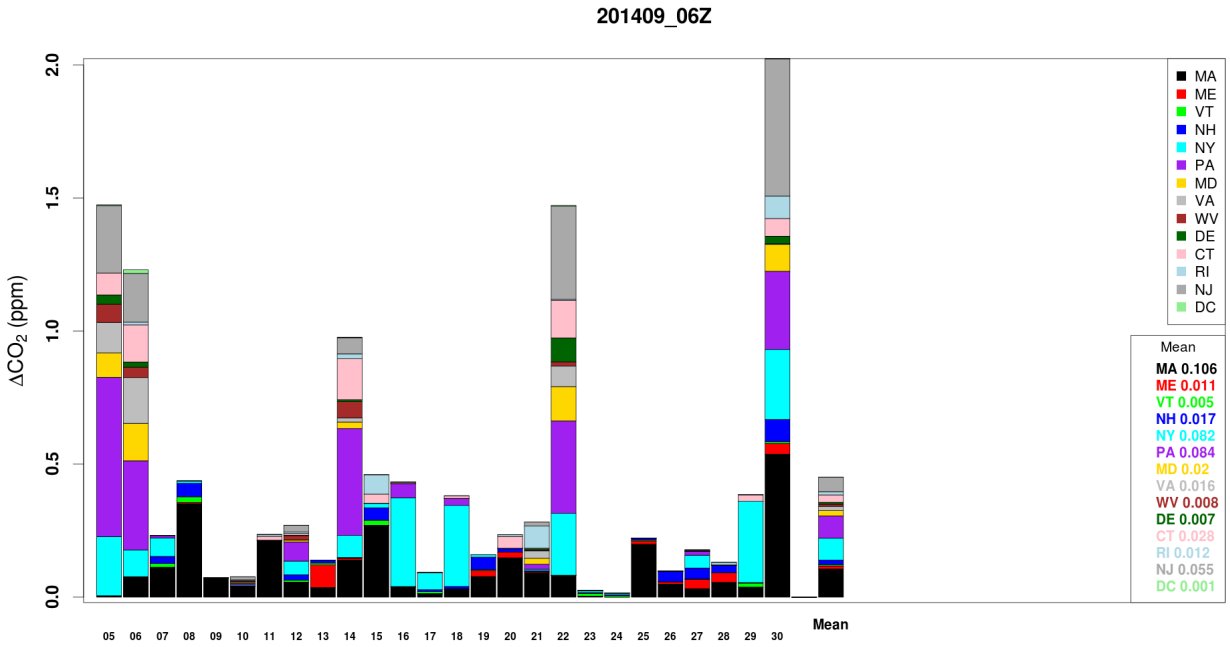

Figure 37. Nighttime mean column CO_2 enhancement (ppm) contributions by state for September 2014 using ACES-STILT starting at 6UTC from our Boston sampling location.

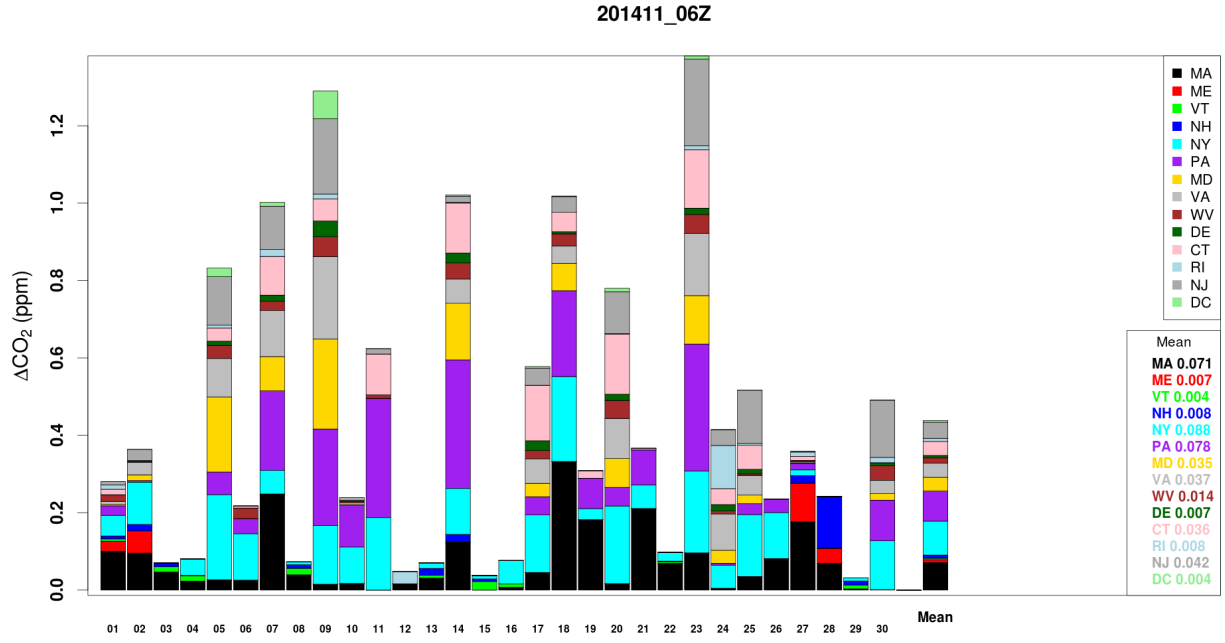

Figure 38. Nighttime mean column CO_2 enhancement (ppm) contributions by state for November 2014 using ACES-STILT staring at 6UTC from our Boston sampling location.

Lastly, CO_2 enhancements estimated from our ACES-STILT framework were compared for four months: February, May, July, September, and October of 2014. Overall, transboundary air pollution from northeastern states had significant influence in the nocturnal RL over Boston (72.6% of total in February; 85.7% of total in July; 62.3% of total in May; 76.5% of total in September; and 83.8% of total in November). The largest CO_2 enhancements occur typically below 2000 meters, which was the average RL height observed by the miniMPL data in Boston. These results highlight the importance of utilizing the RL as a metric for detecting and assessing transboundary air pollution in cities. The highest CO_2 enhancements (~8-10ppm), however, typically occurred below 1000 meters in Boston, especially in the summer and winter months (see Figure 39 below).

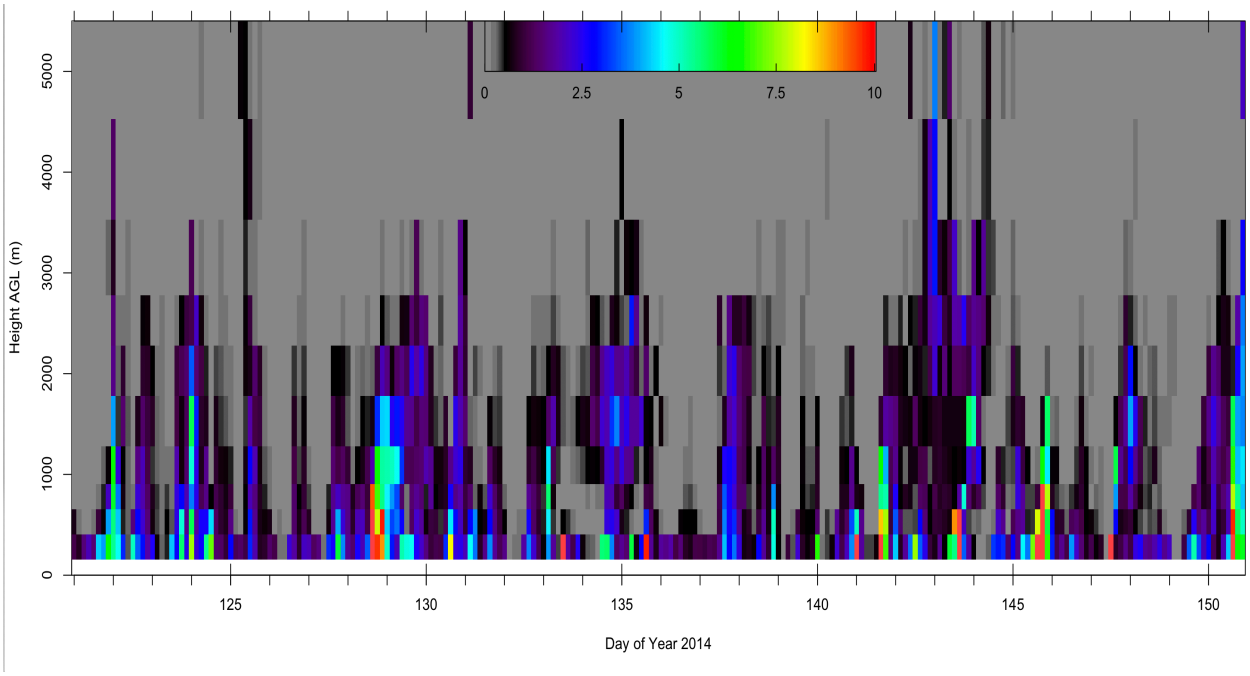

Figure 39. Mean CO_2 enhancements (ranging from 0-10ppm) from ACES-STILT at each receptor location in Boston during a 5-month study period in February, May, July, September, and November of 2014.

Major Findings and Implications

Accurate simulations of PBL heights are essential to the task of forecasting air quality and estimating GHG emissions from atmospheric observations. We have developed the first long-term and continuous record of PBL heights in Boston, MA, using lidar measurements. We compared simulations from five NWP model configurations against miniMPL-retrieved PBL heights for fifteen months. Results showed that the WRF forecast model configurations agreed better with miniMPL observations than the operational (GDAS and NAM) and reanalysis (NARR) products. Additionally, sea breeze conditions were generally not simulated well; agreement improved when data was removed during sea breezes. In the wintertime, the operational and reanalysis products systematically overestimated PBL height in the afternoon. These results emphasize that PBL simulations need to be improved, especially for the low wintertime PBL heights that may cause haze events and public health nuisances.

The lidar was also used to evaluate the performance of two Lagrangian particle dispersion models, estimating CO_2 fluxes in Boston. The time intervals with significant disagreement between the miniMPL-derived and modeled PBL height, especially during periods of low PBL heights, were excellent predictors for CO_2 errors in models. More accurate estimates of PBL heights in meteorological or NWP models, coupled to inversion models, may improve GHG emissions estimates, but careful assessments of the impact of biases and anomalies are required. The *Intergovernmental Panel on Climate Change Task Force on National Greenhouse Gas Inventories (IPCC TFI)* has focused on developing and refining GHG inventories at national scales. But recently, the Paris Agreement and Lima-Paris Action Agenda recognize the critical role of subnational entities, especially cities. A verification system for monitoring rises and reductions of GHG will rely on reducing uncertainties in PBL simulations in atmospheric

transport models at the urban scales. Our compact lidar enables assessment of model performance and provides an objective criterion for excluding days from inversion modeling when the transport simulations are poor.

We also exploited the power of lidar to investigate high levels of aerosol loading within the nocturnal RL, with the aim of tracking transboundary air pollution in Boston. Novel methodology was developed by convolving vertical footprints from the STILT model with the high-resolution CO_2 ACES inventory. By combining vertical NRB profiles from lidar with computed enhancements of CO_2 in the RL by the ACES-STILT framework, over 42 episodes of significant transboundary air pollution were identified in Boston during the five months surveyed (more than 20% of all days). Emission source regions influencing the residual air at night, were identified by computing contributions from each state within the northeastern U.S. Co-emitted air pollutants such as NOx and aerosols can cause adverse effects on public health. The large CO_2 concentrations predicted by our ACES-STILT framework, and potentially associated CO and NOx enhancements, may be measurable in the early morning using new solar-viewing spectrometer now coming into use. The hypothesized link between lidar anomalies, pollutant and CO_2 enhancements, and transboundary pollution will be further investigated in future work. However, our compact lidar has already proven to be an excellent tool in helping detect transboundary air pollution episodes in Boston. *Using lidar to detect and quantify air pollution at night provides an effective means of detecting transboundary air pollution sources that influence cities or states.* As such, our work is critical for regulatory agencies such as the U.S. EPA to enforce the CSAPR's "good neighbor" provisions and track pollution regionally and in states situated hundreds of miles downwind.

References

(1) Lewis, J. R.; Welton, E. J.; Molod, A. M.; Joseph, E. Improved boundary layer depth retrievals from MPLNET. *J. Geophys. Res. Atmos.* **2013,** 118, DOI: 10.1002/jgrd.50570.

(2) Coen, C. M.; Praz, C.; Haefele, A.; Ruffieux, D.; Kaufmann, P.; Calpini, B. Determination and climatology of the planetary boundary layer height above the Swiss plateau by in situ and remote sensing measurements as well as by the COSMO-2 model. *Atmos. Chem. Phys.* **2014**, 14, 13205–13221, DOI: 10.5194/acp14-13205-2014.

(3) Kretschmer, R.; Gerbig, C.; Karstens, U.; Biavati, G.; Vermeulen, A.; Vogel, F.; Hammer, S.; Totsche, K. U. Impact of optimized mixing heights on simulated regional atmospheric transport of CO2. *Atmos. Chem. Phys.* **2014**, 14, 7149–7172, DOI: 10.5194/acp-14-7149-2014.

(4) Ware, J.; Kort, E. A.; DeCola, P.; Duren, R. Aerosol lidar observations of atmospheric mixing in Los Angeles: Climatology and implications for greenhouse gas observations. *J. Geophys. Res. Atmos.* **2016**, 121, 9862–9878, DOI: 10.1002/2016JD024953.

(5) Su, T.; Li, J.; Li, C.; Xiang, P.; Lau, A. K.-H.; Guo, J.; Yang, D.; Miao, Y. An intercomparison of long-term planetary boundary layer heights retrieved from CALIPSO, ground-based lidar, and radiosonde measurements over Hong Kong. *J. Geophys. Res. Atmos.* **2017**, 122, 3929–3943, DOI: 10.1002/2016JD025937.

(6) Sargent, M.; Barrera, Y.; Nehrkorn, T.; Hutyra, L. R.; Gately, C. K.; Jones, T.; McKain, K.; Sweeney, C.; Hegarty, J.; Hardiman, B.; Wofsy, S. C.; Wang, J. A. Anthropogenic and biogenic CO2 fluxes in the Boston urban region. *Proc. Natl. Acad. Sci. U. S. A.* **2018**, 115 (29), 7491−7496, DOI: 10.1073/pnas.1803715115.

(7) Holzworth, G. C. Estimates of mean maximum mixing depths in the contiguous United States. *Mon. Weather Rev*. **1964**, 92, 235–242.

(8) Holzworth, G. C. Mixing depths, wind speeds and air pollution potential for selected locations in the United States. *J. Appl. Meteorol*. **1967**, 6, 1039–1044.

(9) Kaimal, J. C., and J. E. Gaynor. The boulder atmospheric observatory. *J. Clim. Appl. Meteorol.* **1983**, 22, 863–880.

(10) van Ulden, A. P., and J. Wieringa. Atmospheric boundary layer research at Cabauw, *Boundary Layer Meteorol.* **1996**, 78, 39–69.

(11) Spangler, T. C., and R. A. Dirks. Meso-scale variations of the urban mixing height. Boundary Layer Meteorol. **1974**, 6, 423–441.

(12) Melas, D. Sodar estimates of surface heat flux and mixed layer depth compared with direct measurements. *Atmos. Environ*. **1990**, 24A (11), 2847–2853.

(13) Beyrich, F. Mixing height estimation from sodar data—A critical discussion. *Atmos. Environ.* **1997**, 31(23), 3941–3953.

(14) Ecklund, W. L.; Carter, D. A.; Balsley, B. B. A UHF wind profiler for the boundary layer: Brief description and initial results. *J. Atmos. Oceanic Technol*. **1988**, 5, 432–441.

(15) Angevine, W. M.; White, A. B.; Avery, S. K. Boundary layer depth and entrainment zone characterization with a boundary-layer profiler. *Boundary Layer Meteorol*. **1994**, 68, 375–385.

(16) U. S. A. Energy Information Administration. Massachusetts State Energy Profile. https://www.eia.gov/state/?sid=MA (Accessed Nov 7, 2017).

(17) Masri, S.; Kang, C. M.; Koutrakis, P. Composition and sources of fine and coarse particles collected during 2002–2010 in Boston, MA. *J. Air Waste Manag. Assoc*. **2015**, 65 (3), 287–297, DOI: 10.1080/10962247.2014.982307.

(18) Stull, R. B. *An Introduction to Boundary-Layer Meteorology*; Kluwer Academy Publishers: Dordrecht, Netherlands, 1988, pp 14.

(19) Oke, T.R. *Boundary Layer Climate*. Routledge, London, UK, 1990, pp 298.

(20) Klein, P.M. Impacts of Mixing Processes in Nocturnal Atmospheric Boundary Layer on Urban Ozone Concentrations. *Boundary-Layer Meteor*. **2014**, 150, 107-130, DOI: 10.1007/s10546-013-9864-4

(21) Zhao, X. J.; P. S. Zhao; J. Xu; W. Meng; W. W. Pu; F. Dong; D. He; and Q. F. Shi. Analysis of a winter regional haze event and its formation mechanism in the North China Plain. Atmos. Chem. Phys. 2013, 13, 5685-5696. DOI: 10.5194/acp-13-5685-2013

(22) Sun, Y. L.; Wang, Z. F.; Fu, P. Q.; Yang, T.; Jiang, Q.; Dong, H. B.; Li, J.; Jia, J. J. Aerosol composition, sources and processes during wintertime in Beijing, China, Atmos. Chem. Phys., 13, 4577–4592, doi:10.5194/acp-13-4577-2013, 2013.

(23) Han, S.; Bian, H.; Tie, X.; Xie, Y.; Sun, M.; Liu, A. Impact of nocturnal planetary boundary layer on urban air pollutants: Measurements from a 250-m tower over Tianjin. China. J. Hazard. Mater. **2009**,162: 264–269.

(24) Couach, O.; Balin, I.; Jimenez, R.; Ristori, P.; Perego, S.; Kirchner, F.; Simeonov, V.; Calpini, B.; van den Bergh, H. An investigation of ozone and planetary boundary layer dynamics over the complex topography of Grenoble combining measurements and modeling. *Atmos. Chem. Phys.* **2003**, 3, 549-562.

(25) Lemone, M. A.; Tewari, M.; Chen, F.; Dudhia, J. Objectively Determined Fair-Weather CBL Depths in the ARW-WRF Model and Their Comparison to CASES-97 Observations. American Meteorological Society. **2009**, 141, 20. DOI: 10.1175/MWR-D-12-00106.1

(26) Blay-Carreras, E.; Pino, D.; Vilà-Guerau de Arellano, J.; van de Boer, A.; De Coster, O.; Darbieu, C.; Hartogensis, O.; Lohou, F.; Lothon, M.; Pietersen, H. Role of the residual layer and large-scale subsidence on the development and evolution of the convective boundary layer. *Atmos. Chem. Phys.* **2014**, 14, 4515–4530, DOI: 10.5194/acp-14-4515-2014.

(27) Emeis, S.; Schafer, K. Remote sensing methods investigate boundary-layer structures relevant to air pollution in cities. *Bound. Layer Meteorol.* **2006**, 121, 377–385, DOI: 10.1007/s10546-006-9068-2.

(28) Baars, H.; Ansmann, A.; Engelmann, R.; Althausen, D. Continuous monitoring of the boundary-layer top with lidar. *Atmos. Chem. Phys.* **2008**, 8, 7281-7296.

(29) Gan, C-., M.; Wu, Y.; Bomidi, L. M.; Gross, B.; Moshary, F. Application of active optical sensors to probe the vertical structure of the urban boundary layer and assess anomalies in air quality model PM2.5 forecasts. *Proc. SPIE 8182, Lidar Technologies, Techniques, and Measurements for Atmospheric Remote Sensing* VII, *81820P (7 October 2011)*, DOI: 10.1117/12.898360.

(30) Melfi, S. H.; Spinhirne, J. D.; Chou, S. H.; Palm, S. P. Lidar observations of vertically organized convection in the planetary boundary layer over the ocean. *J. Appl. Meteorol. Climatol*. **1985**, 24(8), 806–821.

(31) Cheng, Z. Y; Jing, X. Denoising differential column image motion lidar signal using singular value decomposition. Applied Optics and Photonics. 2017, DOI: 10.1117/12.2285201.

(32) Barlow, J. F. Progress in observing and modelling the urban boundary layer. *Urban Clim.* **2014**, 10, 2160, DOI: 10.1016/j.uclim.2014.03.01.1.

(33) Davis, K. J.; Gamage, N.; Hagelberg, C. R.; Kiemle, C.; Lenschow, D. H.; Sullivan, P. P. An objective method for deriving atmospheric structure from airborne lidar observations. *J. Atmos. Oceanic Technol.* **2000**, 17, 1455–1468, DOI: 0.1175/1520-0426(2000)017<1455:AOMFDA>2.0.CO;2.

(34) Brooks, I. M. Finding boundary layer top: Application of a wavelet covariance transform to lidar backscatter profiles. *J. Atmos. Oceanic Technol.* **2003**, 20, 1092–1105, DOI: 10.1175/1520-0426(2003)020<1092:FBLTAO>2.0.CO;2.

(35) Seaman, N. L. Meteorological modeling for air-quality assessments. *Atmos. Environ*. **2000**, 34, 2231-2259.

(36) Banks, R. F.; Tiana-Alsina, J.; Rocadenbosch, F.; Baldasano, B. M. Performance Evaluation of the Boundary-Layer Height from Lidar and the Weather Research and Forecasting Model at an Urban Coastal Site in the North-East Iberian Peninsula*. Boundary-Layer Meteorology*. **2015**, 157, 265–292, DOI: 10.1007/s10546-015-0056-2.

(37) Banks, R. F., and Baldasano, J. M. Impact of WRF model PBL schemes on air quality simulations over Catalonia, Spain. *Science of the Total Environment.* **2016**, 572, 98–113, DOI: 10.1016/j.scitotenv.2016.07.167.

(38) Hegarty, J. D.; Lewis, J.; McGrath-Spangler, E. L.; Henderson, J.; Scarino, A. J.; DeCola, P.; Ferrare, R.; Hicks, M.; Adams-Selin, R. D.; Welton, E. J. Analysis of the Planetary Boundary Layer Height during DISCOVER-AQ Baltimore–Washington, D.C., with Lidar and High-Resolution WRF Model. *J. Appl. Meteor. Climatol.* **2018**, 57, 2679 – 2695, DOI: 10.1175/JAMC-D-18-0014.1.

(39) Borge, R.; Alexandrov, V.; del Vas, J. J.; Lumbreras, J.; Rodríguez, E. A comprehensive sensitivity analysis of the WRF model for air quality applications over the Iberian Peninsula. *Atmospheric Environment*. **2008**, 42, 8560–8574, DOI: 10.1016/j.atmosenv.2008.08.032.

(40) Pichelli, E.; Ferretti, R.; Cacciani, M.; Siani, A. M.; Ciardini, V.; Di Iorio, T. The role of urban boundary layer investigated with high-resolution models and ground-based observations in Rome area: a step towards understanding parameterization potentialities. *Atmos. Meas. Tech*. **2014**, 7, 315–332, DOI: 10.5194/amt-7-315-2014.

(41) Lauvaux, T.; Miles, N. L.; Deng, A.; Richardson, S. J.; Cambaliza, M. O.; Davis, K. J.; Gaudet, B.; Gurney, K. R.; Huang, J.; O'Keefe, D.; et al. High-resolution atmospheric inversion of urban CO2 emissions during the dormant season of the Indianapolis Flux Experiment (INFLUX). *J. Geophys. Res. Atmos.* **2016**, 121, 5213–5236, DOI: 10.1002/2015JD024473.

(42) Deng, A.; Lauvaux, T.; Davis, K. J.; Gaudet, B. J.; Miles, N.; Richardson, S. J.; Wu, K.; Sarmiento, D. P.; Hardesty, R. M.; Bonin, T. A.; et al. Toward reduced transport errors in a high resolution urban CO2 inversion system. *Elem. Sci. Anth*. **2017**, 5, DOI: 10.1525/elementa.133.

(43) Skamarock, W. C.; Klemp, J. B. A time-split nonhydrostatic atmospheric model for weather research and forecasting applications. *J. Comput. Phys.* **2008**, 227, 3465–3485, DOI: 10.1016/j.jcp.2007.01.037.

(44) Powers, J. G.; Klemp, J. B.; Skamarock, W. C.; Davis, C. A.; Dudhia, J.; Gill, D. O.; Coen, J. L.; Gochis, D. J.; Ahmadov, R.; Peckham, S. E.; et al. The Weather Research and Forecasting (WRF) Model: Overview, system efforts, and future directions. *Bull. Amer. Meteor. Soc.* **2017**, 98, 1717–1737, DOI: 10.1175/BAMS-D-15-00308.1.

(45) McKain, K.; Down, A.; Raciti, S. M.; Budney, J.; Hutyra, L. R.; Floerchinger, C.; Herndon, S.; Nehrkorn, T.; Zahniser, M. S.; Jackson, R. B.; et al. Methane emissions from natural gas infrastructure and use in the urban region of Boston, Massachusetts. *Proc. Natl. Acad. Sci. U. S. A.* **2015**, 112, 1941−1946, DOI: 10.1073/pnas.1416261112.

(46) Jiménez, P. A.; Dudhia, J. On the Ability of the WRF Model to Reproduce the Surface Wind Direction Over Complex Terrain. *J. Appl. Meteor. Climatol.* **2013**, 52, 1610–1617, DOI: 10.1175/JAMC-D-12-0266.1.

(47) Nehrkorn, T.; Henderson, J.; Leidner, M.; Mountain, M.; Eluszkiewicz, J.; McKain, K.; Wofsy, S. C. WRF simulations of the urban circulation in the Salt Lake City area for CO_2 modeling. *J. Appl. Meteor. Clim.* **2013**, 52, 323-340, DOI: 10.1175/JAMC-D-12-061.1.

(48) Mesinger, F.; DiMego, G.; Kalnay, E.; Mitchell, K.; Shafran, P. C.; Ebisuzaki, W.; Jovic, D.; Woollen, J.; Rogers, E.; Berbery, E. H.; et al. North American Regional Reanalysis. *Bull. Amer. Meteor. Soc.* **2006**, 87, 343–360, DOI: 10.1175/BAMS-87-3-343.

(49) Janjic, Z. I. A nonhydrostatic model based on a new approach. *Meteor. Atmos. Phys.* **2003**, 82, 271–285, DOI: 10.1007/s00703-001-0587-6.

(50) Kleist, D. T.; Parrish, D. F.; Derber, J. C.; Treadon, R.; Wu, W. S.; Lord, S. Introduction of the GSI into the NCEP Global Data Assimilation System. *Wea. Forecasting*. **2009**, 24, 1691–1705, DOI: 10.1175/2009WAF2222201.1.

(51) Nehrkorn, T.; Eluszkiewicz, J.; Wofsy, S. C.; Lin, J. C.; Gerbig, C.; Longo, M.; Freitas, S. Coupled weather research and forecasting-stochastic time-inverted Lagrangian transport (WRF-STILT) model. *Meteorol. Atmos. Phys*. **2010**, 107 (1), 51-64, DOI: 10.1007/s00703-010-0068-x.

(52) Gately, C. K.; Hutyra, L. R. Large uncertainties in urban-scale carbon emissions.

J. Geophys. Res. Atmos. **2017**, 122 (11), 11242–11260, DOI: 10.1002/2017JD027359.

(53) Han, B.; Zhao, C. L.; Lü, S. H.; Wang, X. A diagnostic analysis on the effect of the residual layer in convective boundary layer development near Mongolia using 20th century reanalysis data. *Adv. Atmos. Sci*. **2015**, 32 (6), 807–820, DOI: 10.1007/s00376-014-4164-6.

(54) Hicks, B. B.; O'Dell, D. L.; Eash, N. S.; Sauer, T. J. Nocturnal intermittency in surface CO2 concentrations in sub-Saharan Africa. *Agricultural and Forest Meteorology*. **2015**, 200, 129–134, DOI: 10.1016/j.agrformet.2014.09.007.

(55) Karipot, A.; Leclerc, M. Y.; Zhang, G.; Martin, T.; Starr, G.; Hollinger, D.; McCaughey, J. H.; Hendrey, G. R. Nocturnal CO2exchange over a tall forest canopy associated with intermittent low-level jet activity. *Theor. Appl. Climatol*. **2006**, 85, 243–248.

(56) Venzac, H.; Sellegri, K.; Villani, P.; Picard, D.; Laj, P. Seasonal variation of aerosol size distributions in the free troposphere and residual layer at the puy de Dˆome station, France. Atmos. Chem. Phys. **2009**, 9, 1465–1478.

(57) Stensrud, D. J. Elevated residual layers and their influence on surface boundary-layer evolution. *J. Int. Atmos. Sci*. **1993**, 50 (14), 2284- 2293.

(58) Fochesatto, J. G. Evidence of dynamical coupling between the residual layer and the developing convective boundary layer. *Boundary-Layer Meteorology*. **2001**, 99, 451-464. DOI: 10.1023/A:1018935129006.

(59) Henne, S.; Klausen, J.; Junkermann, W.; Kariuki, J. M.; Aseyo, J. O.; Buchmann, B. Representativeness and climatology of carbon monoxide and ozone at the global GAW station Mt. Kenya in equatorial Africa. *Atmos. Chem. Phys*. **2008**, 8, 3119–3139.

(60) Kolev, N. I.; Savov, P. B.; Kaprielov, B. K.; Grigorieva, V. N.; Kolev, I. N. Influence of the boundary layer development on the ozone concentration over an urban area. *International Journal of Remote Sensing*. **2008**, 29 (7), 1877–1902.

(61) Lee, S-. M; Fernando, H. J. S.; Princevac, M.; Zajic, D.; Sinesi, M.; McCulley, J. L.; Anderson J. Transport and Diffusion of Ozone in the Nocturnal and Morning Planetary Boundary Layer of the Phoenix Valley. *Environmental Fluid Mechanics*. **2003**, 3, 331–362.

(62) Hu, X-. M.; Doughty, D. C.; Sanchez, K. J.; Joseph, E.; Fuentes, J. D. Ozone variability in the atmospheric boundary layer in Maryland and its implications for vertical transport model. *Atmos Environ.* **2012**, 46, 354–364.

(63) Hu, X-. M.; Klein, P.; Xue, M.; Zhang, F.; Doughty, D.; Forkel, R.; Joseph, E.; Fuentes, J. D. Impact of the vertical mixing induced by low-level jets on boundary layer ozone concentration. *Atmos. Environ*. **2013**, 70, 123–130.

(64) Curci, G.; Ferrero, L.; Tuccella, P.; Barnaba, F.; Angelini, F.; Bolzacchini, E.; Carbone, C.; Denier van der Gon, H. A. C.; Facchini, M. C.; Gobbi, G. P.; Kuenen, J. P. P.; Landi, T. C.; Perrino, C.; Perrone, M. G.; Sangiorgi, G.; Stocchi, P. How much is particulate matter near the ground influenced by upper-level processes within and above the PBL? A summertime case study in Milan (Italy) evidences the distinctive role of nitrate. *Atmos. Chem. Phys.* **2015**, 15, 2629–2649.

(65) Olofson, K. F. G.; Andersson, P. U.; Hallquist, M.; Ljungström, E.; Tang, L.; Chen, D.; Pettersson, J. B. C. Urban aerosol evolution and particle formation during wintertime temperature inversions. *Atmospheric Environment*. **2008**, 43, 340–346, DOI: 10.1016/j.atmosenv.2008.09.080.

(66) Wehner, B.; Siebert, H.; Ansmann, A.; Ditas, F.; Seifert, P.; Stratmann, F.; Wiedensohler, A.; Apituley, A.; Shaw, R. A.; Manninen, H. E.; Kulmala, M. Observations of turbulence-induced new particle formation in the residual layer. *Atmos. Chem. Phys.* **2010**, 10, 4319–4330, DOI: 10.5194/acp-10-4319-2010.

(67) Arellano J. V-. G.; Gioli, B.; Miglietta, F.; Jonker, H. J. J; Baltink. H. K.; Hutjes, R. W. A.; Holtslag, A. A. M. Entrainment process of carbon dioxide in the atmospheric boundary layer. *J. Geophys. Res.* **2004**, 109 (D18110), DOI: 10.1029/2004JD004725.

(68) Donnell, E. A; Fish, D. J.; Dicks, E. M. Mechanisms for pollutant transport between the boundary layer and the free troposphere. *J. Geophys. Res*. **2001**, 106 (D8), 7847-7856.

(69) Lin, J. C.; Gerbig, C.; Wofsy, S. C.; Andrews, A. E.; Daube, B. C.; Davis, K. J.; Grainger, C. A. A near-field tool for simulating the upstream influence of atmospheric observations: The stochastic time-inverted Lagrangian transport model (STILT). *J. Geophys. Res*. **2003**, 108 (D16), 4493, DOI: 10.1029/2002JD003161.

(70) Chen, J.; Viatte, C.; Hedelius, J. K.; Jones, T.; Franklin, J. E.; Parker, H.; Gottlieb, E. W; Wennberg, P. O.; Dubey, M. K.; Wofsy, S. C. Differential column measurements using compact solar-tracking spectrometers. *Atmos. Chem. Phys*. **2016**, 16, 8479–8498, DOI: 10.5194/acp-16-8479-2016.

(71) Hase, F.; Frey M.; Blumenstock, T.; Groß, J.; Kiel, M.; Kohlhepp, R.; Tsidu, M. G.; Schäfer, K.; Sha, M. K.; Orphal, J. Application of portable FTIR spectrometers for detecting greenhouse gas emissions of the major city Berlin. **2015**, *Atmos. Meas. Tech.*, 8, 3059–3068, DOI: 10.5194/amt-8-3059-2015.

Appendix

Chapter 3

Figures and Tables

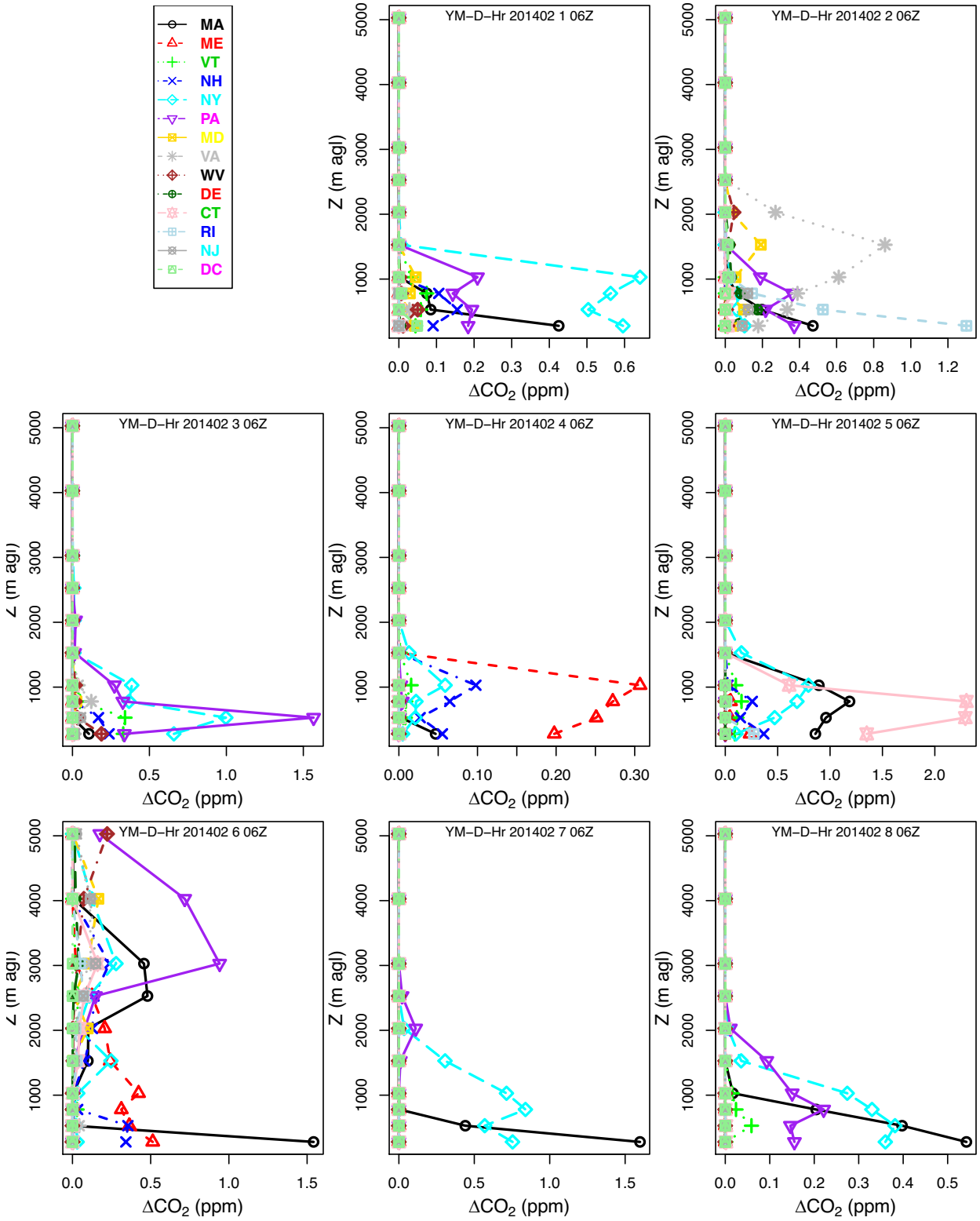

Figure A1. February 2014 ACES-STILT derived CO_2 enhancements at each receptor height, starting at 6 UTC (within the nocturnal RL and above the nocturnal PBL) in Boston.

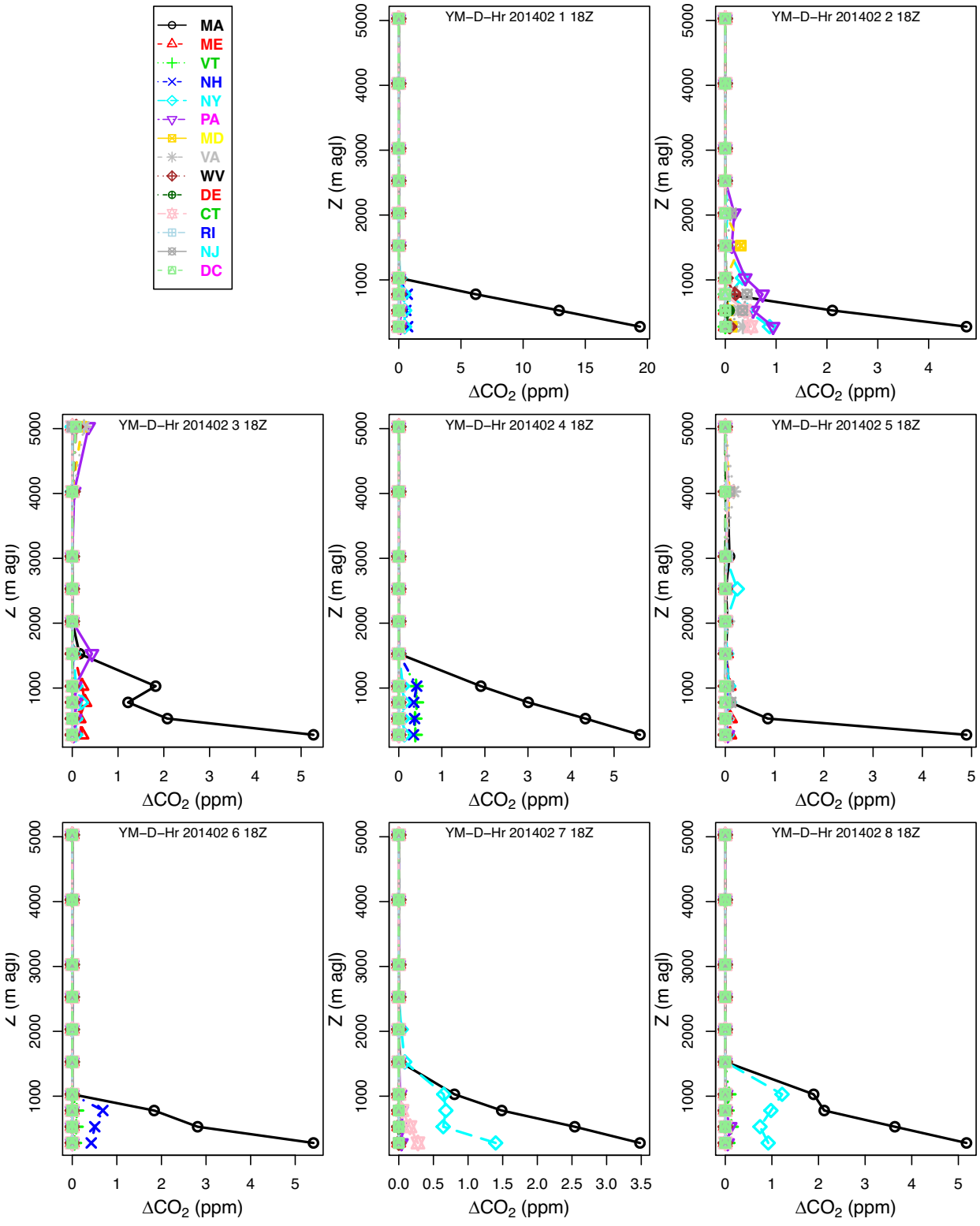

Figure A2. February 2014 ACES-STILT derived CO_2 enhancements at each receptor height, starting at 18 UTC (well-mixed PBL conditions) in Boston.

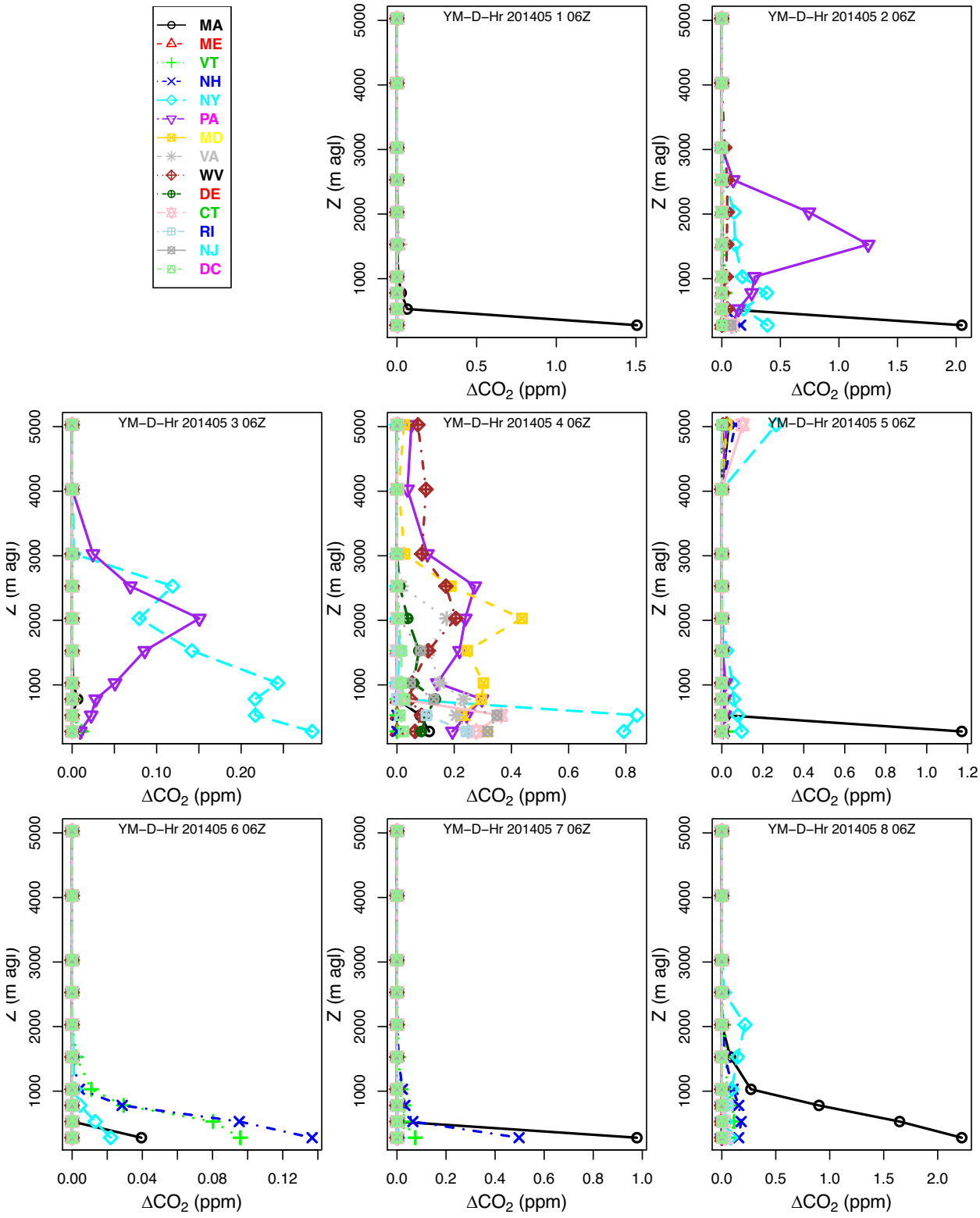

Figure A3. May 2014 ACES-STILT derived CO_2 enhancements at each receptor height, starting at 6 UTC (within the nocturnal RL and above the nocturnal PBL) in Boston.

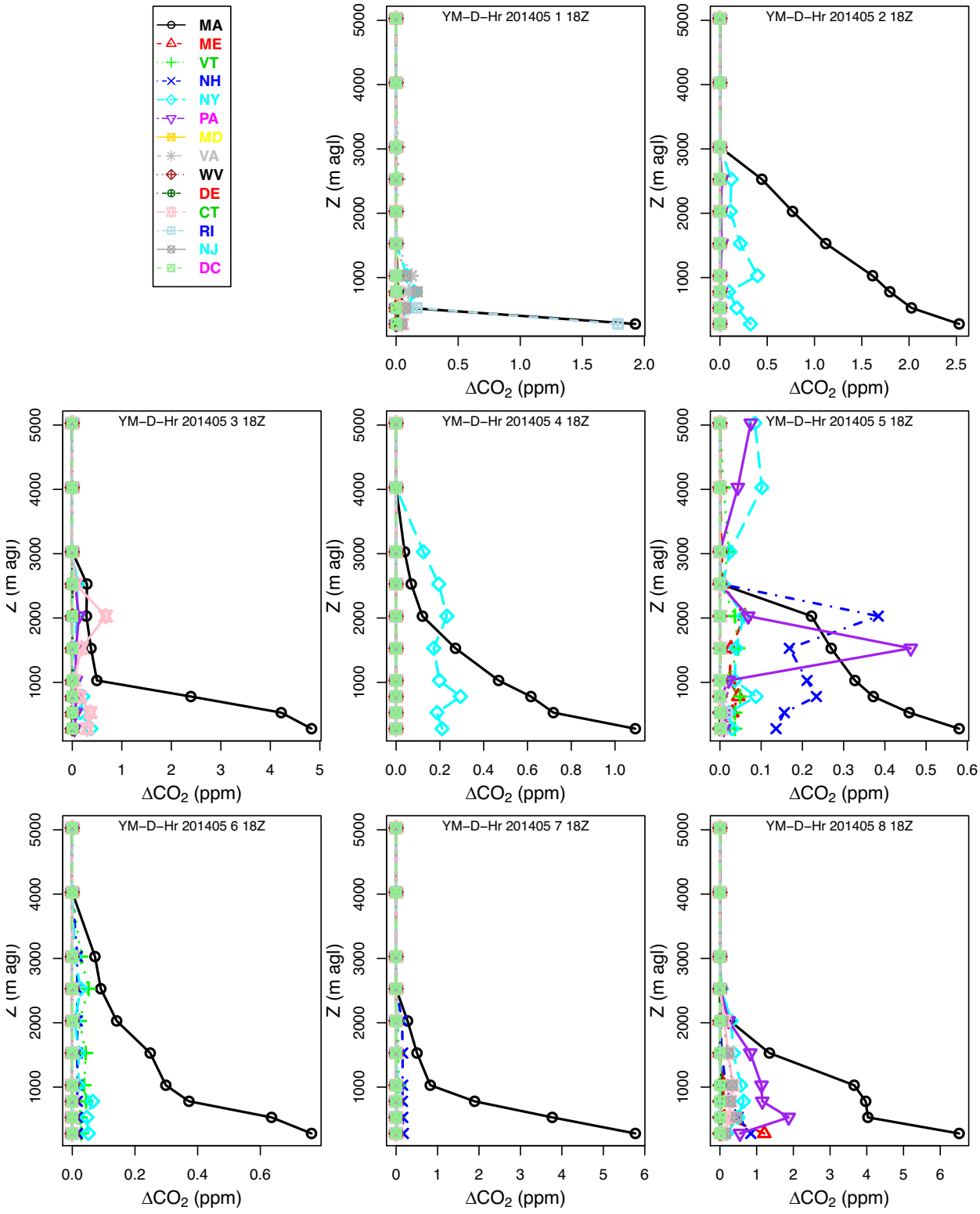

Figure A4. May 2014 ACES-STILT derived CO_2 enhancements at each receptor height, starting at 18 UTC (well-mixed PBL conditions) in Boston.

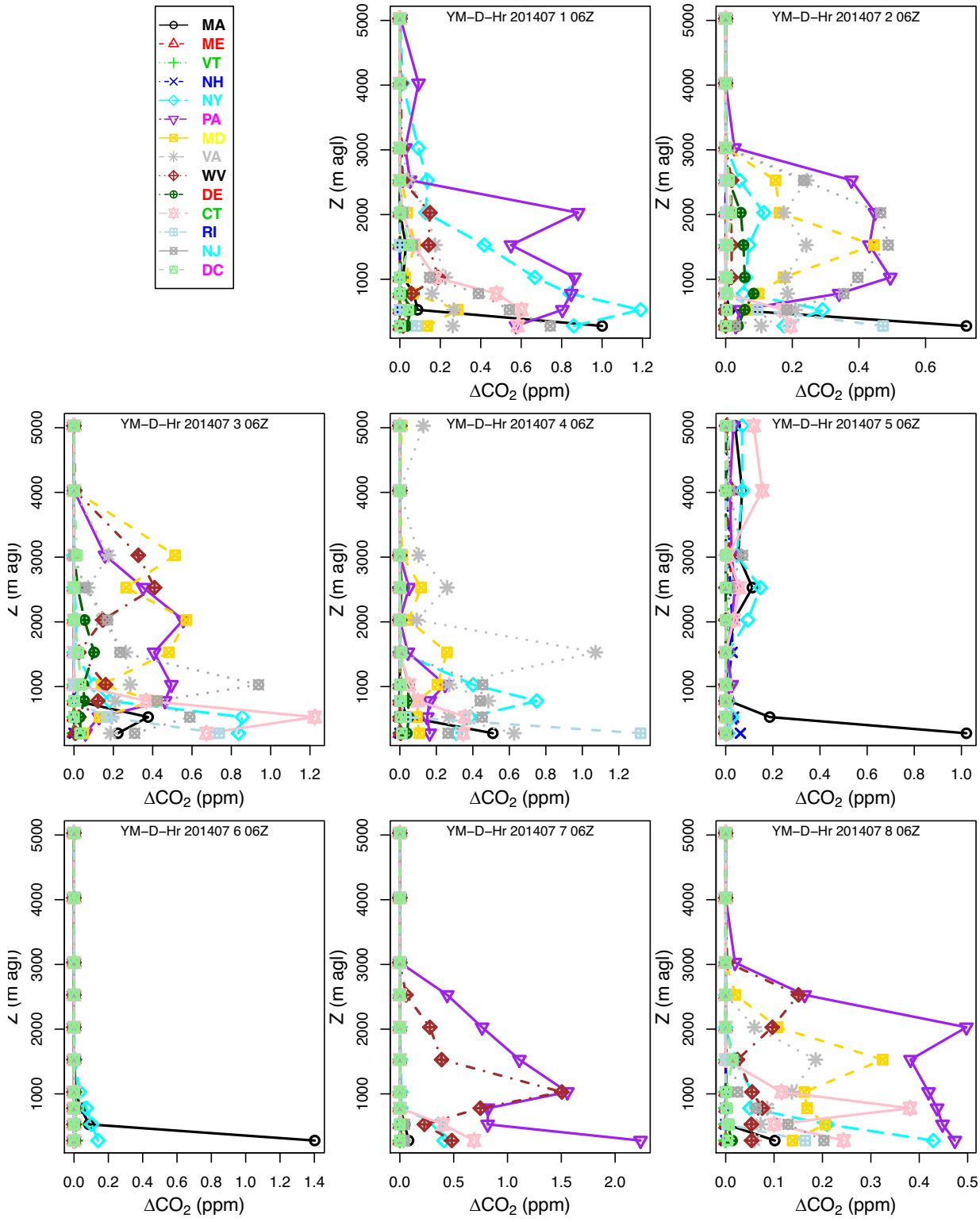

Figure A5. July 2014 ACES-STILT derived CO_2 enhancements at each receptor height, starting at 6 UTC (within the nocturnal RL and above the nocturnal PBL) in Boston.

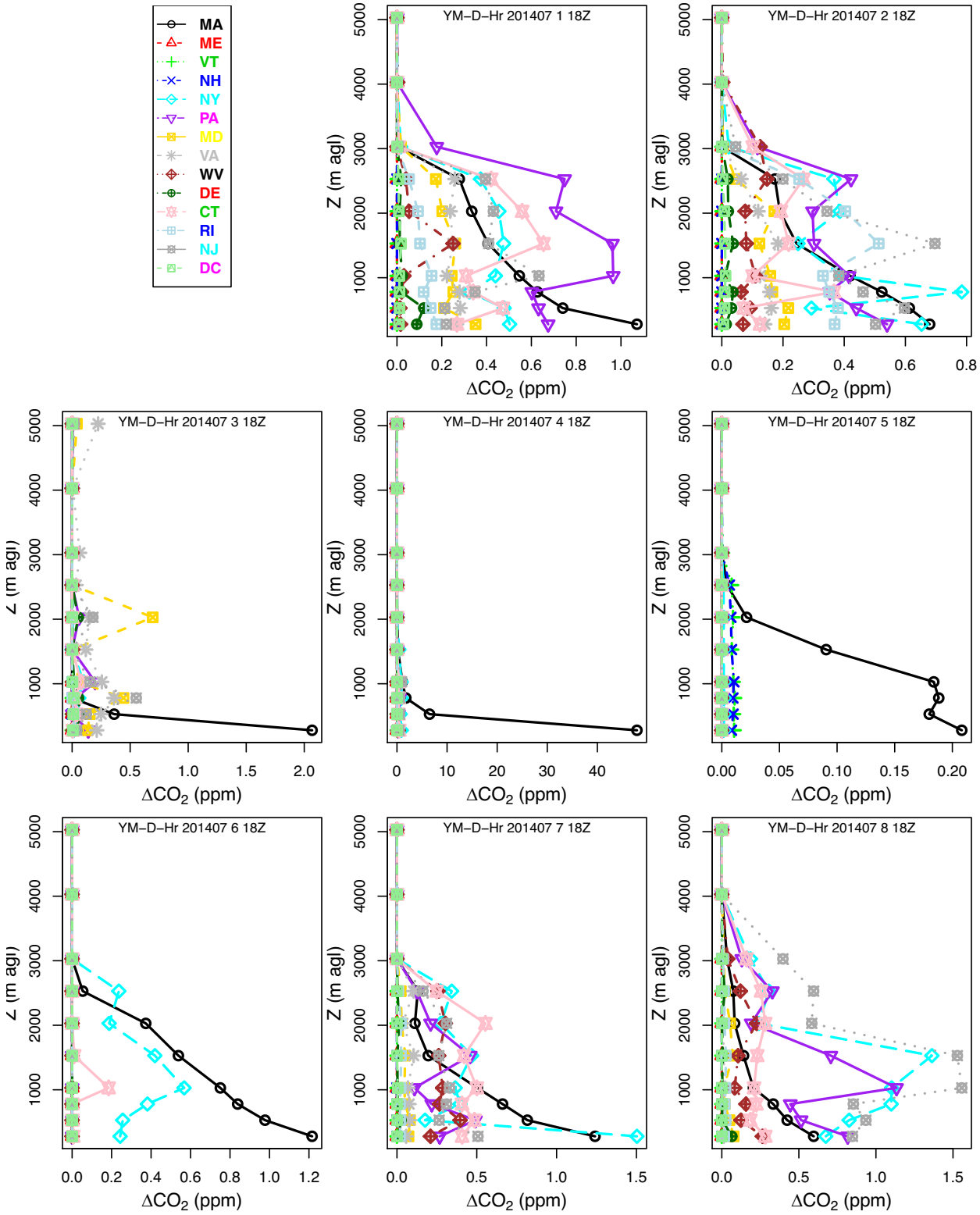

Figure A6. July 2014 ACES-STILT derived CO_2 enhancements at each receptor height, starting at 18 UTC (well-mixed PBL conditions) in Boston.

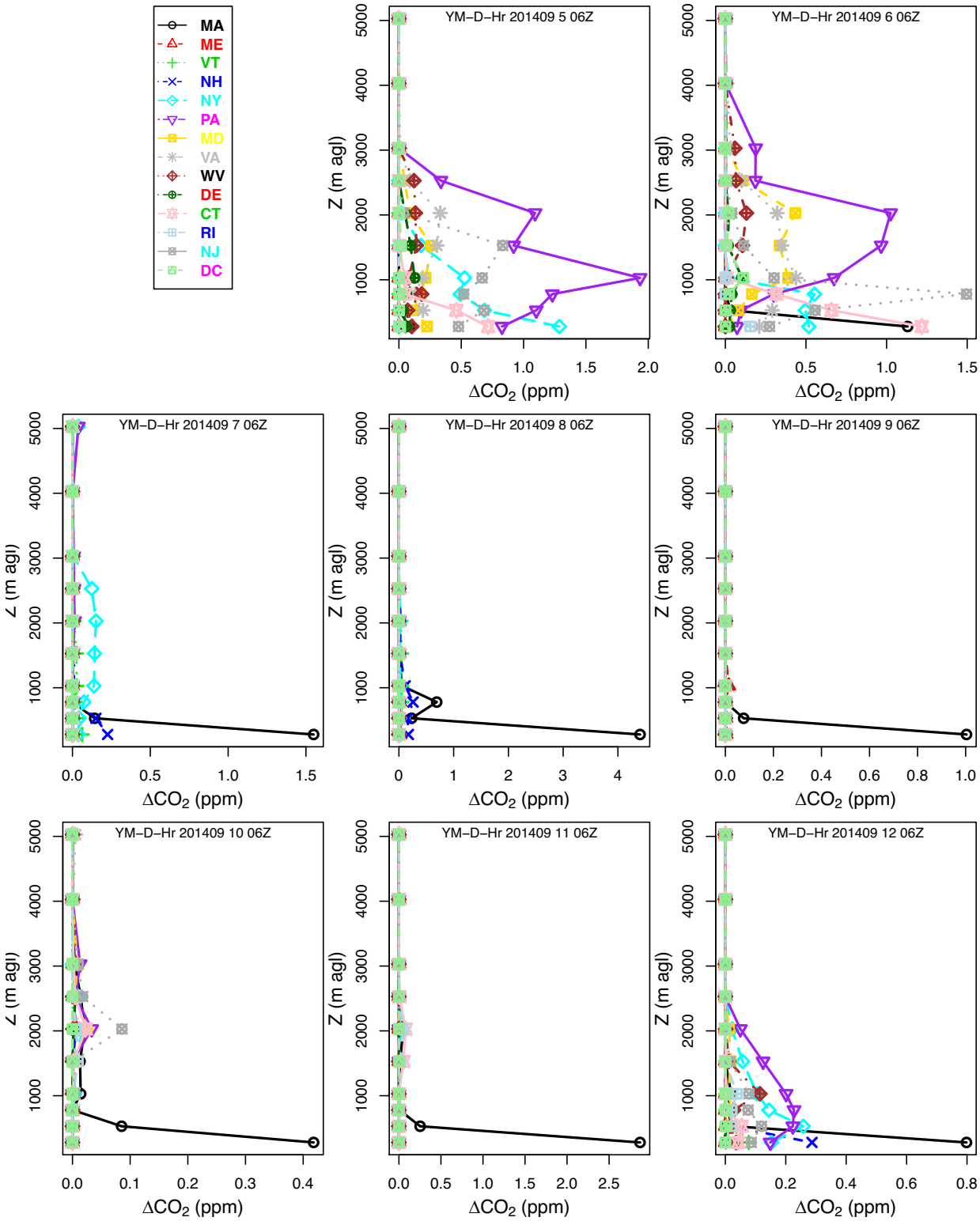

Figure A7. September 2014 ACES-STILT derived CO_2 enhancements at each receptor height, starting at 6 UTC (within the nocturnal RL and above the nocturnal PBL) in Boston.

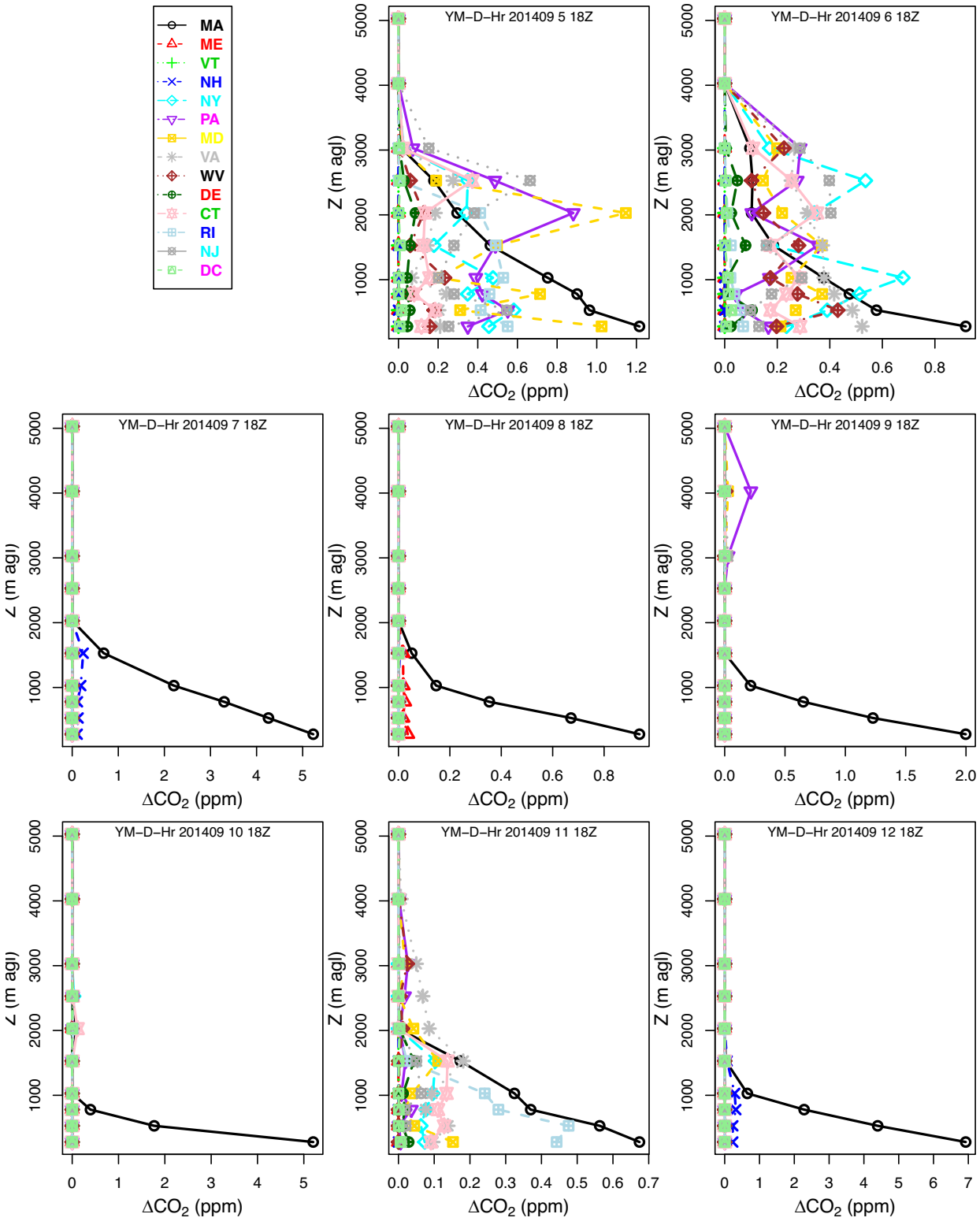

Figure A8. July 2014 ACES-STILT derived CO_2 enhancements at each receptor height, starting at 18 UTC (well-mixed PBL conditions) in Boston.

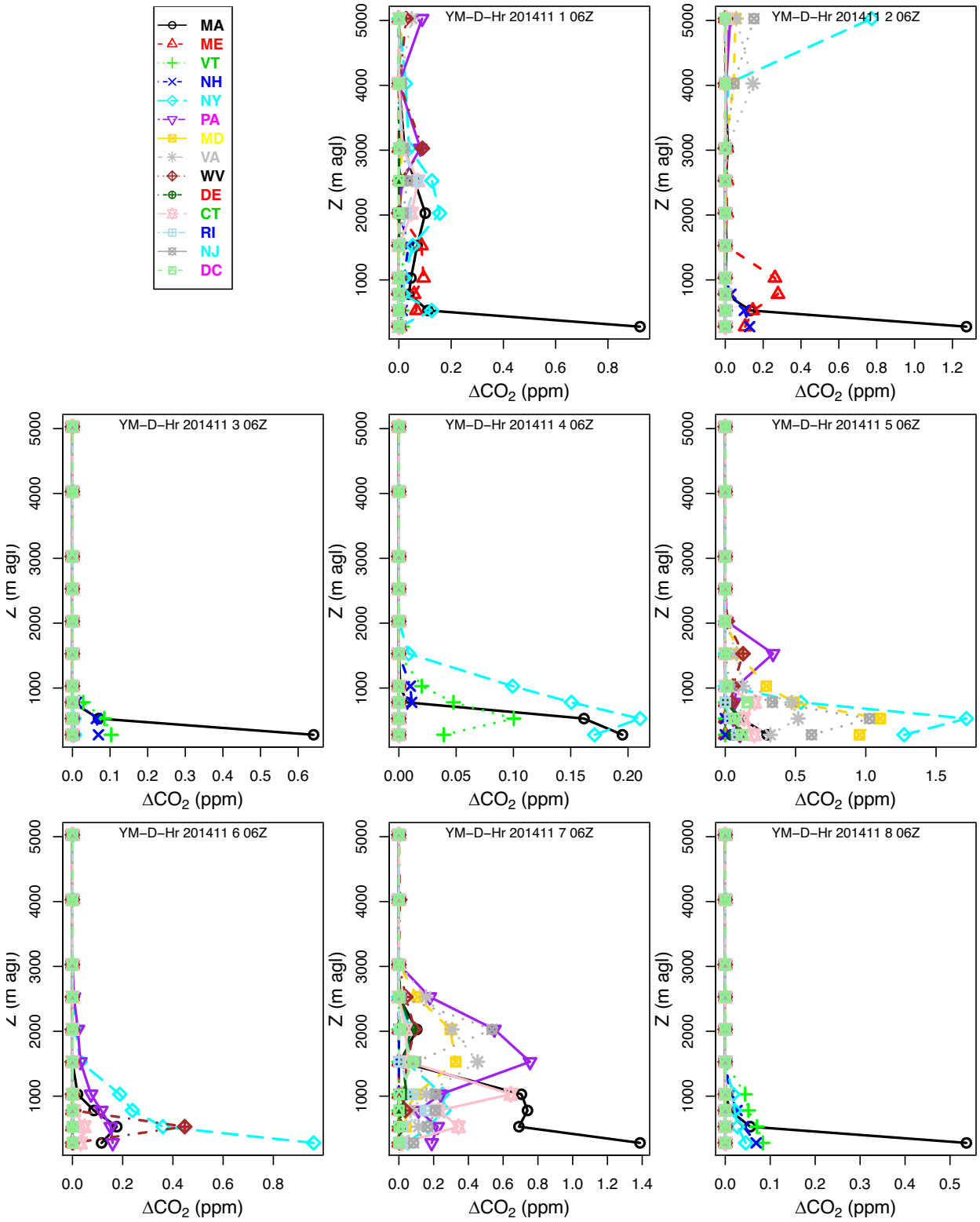

Figure A9. November 2014 ACES-STILT derived CO_2 enhancements at each receptor height, starting at 6 UTC (within the nocturnal RL and above the nocturnal PBL) in Boston.

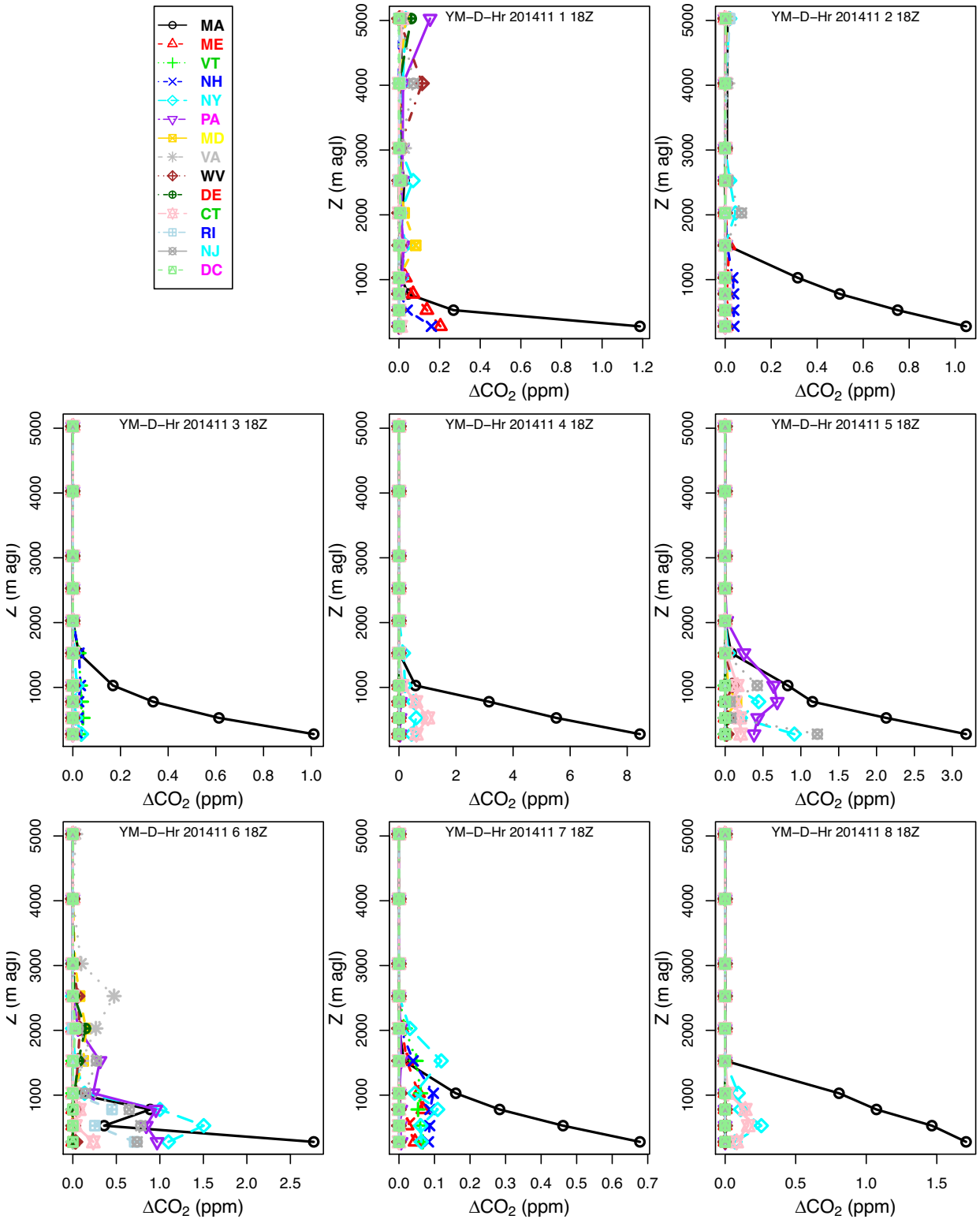

Figure A10. November 2014 ACES-STILT derived CO_2 enhancements at each receptor height, starting at 18 UTC (well-mixed PBL conditions) in Boston.

Spring 2014 ACES-STILT Atmospheric Column Average of CO_2 Enhancements (ppm) by State in Northeastern U.S.

ACES –STILT, 72 hours backwards in time starting at 6UTC

Date	NRB	MA	ME	VT	NH	NY	PA	MD	VA	WV	DE	CT	RI	NJ	DC
May 11	>0.3	1.94e-01	0.00	0.00	0.00	8.78e-02	2.22e-01	8.79e-04	7.79e-04	8.80e-03	0.00	4.35e-02	0.00	6.70e03	0.00
May 12	>0.3	1.07e-04	0.00	3.26e-03	3.27e-03	1.52e-02	0.00	0.00	0.00	0.00	0.00	0.00	0.00	0.00	0.00
May 13	>0.3	1.46e-01	2.79e-02	2.90e-03	1.72e-02	1.03e-01	1.85e-01	1.52e-02	8.37e-03	9.32e-03	7.69e-03	3.65e-02	1.22e04	7.37e-02	1.68e-03
May 21	>0.3	8.70e-03	6.90e-04	4.35e-04	2.39e-02	0.00	0.00	0.00	0.00	0.00	0.00	0.00	0.00	0.00	0.00
May 22	>0.3	2.06e-01	3.00e-04	1.31e-04	1.55e-02	2.75e0-2	3.44e-03	0.00	0.00	1.33e-03	0.00	3.91e-02	6.29e-02	9.75e-04	0.00
May 26	>0.3	9.23e-02	7.37e-08	3.10e-03	1.46e-04	5.65e-02	0.00	0.00	0.00	0.00	0.00	4.16e-02	0.00	0.00	0.00
May 27	>0.3	6.38e-02	0.00	5.85e-03	3.13e-03	3.35e-02	0.00	0.00	0.00	0.00	0.00	0.00	0.00	0.00	0.00

Table A1. Spring 2014 transboundary air pollution episodes detected with lidar NRB > 0.3, with CO_2 enhancement influence at the Boston sampling location by State.

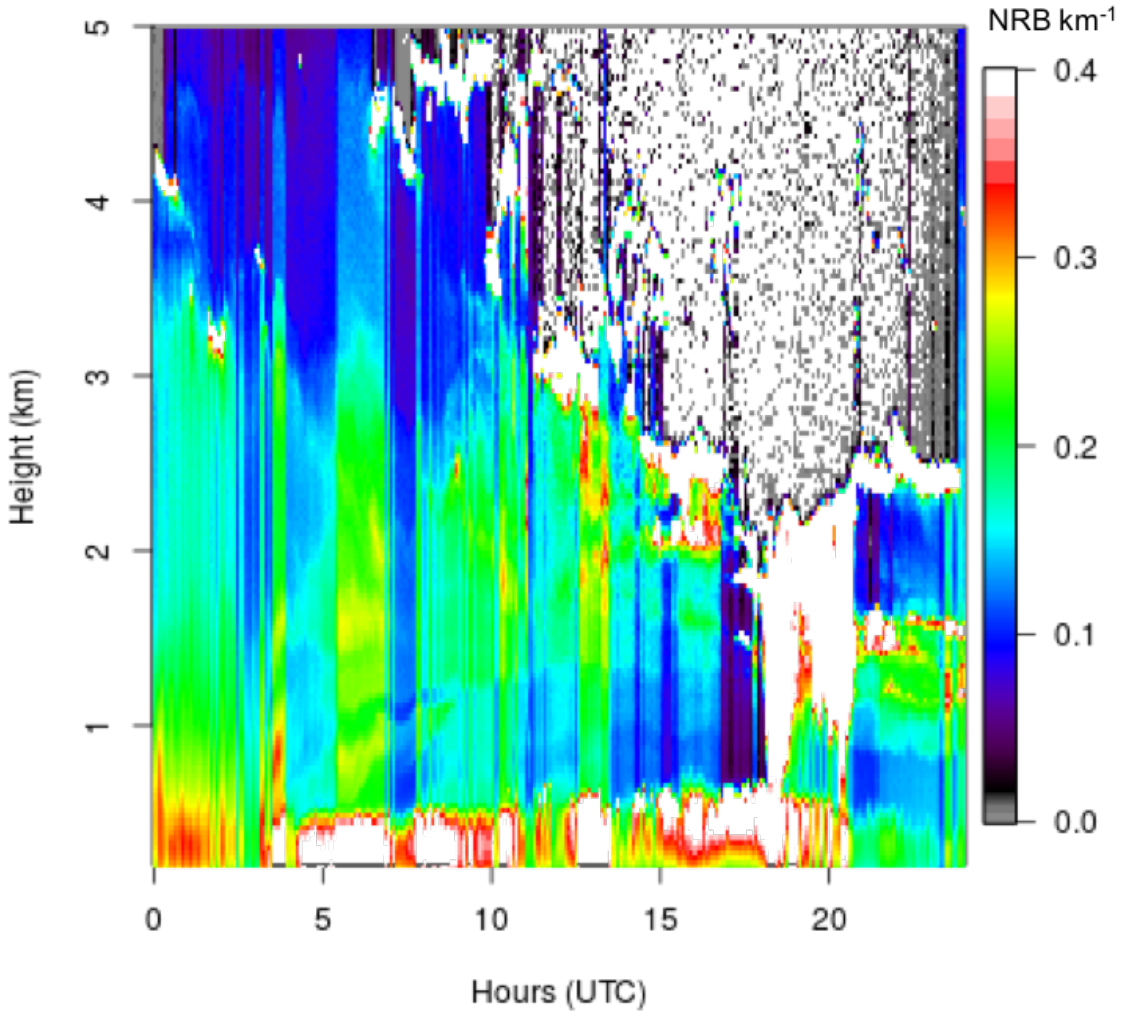

Figure A11. Lidar NRB enhancements (> 0.3) detected in nocturnal RL (6 UTC) in Boston.

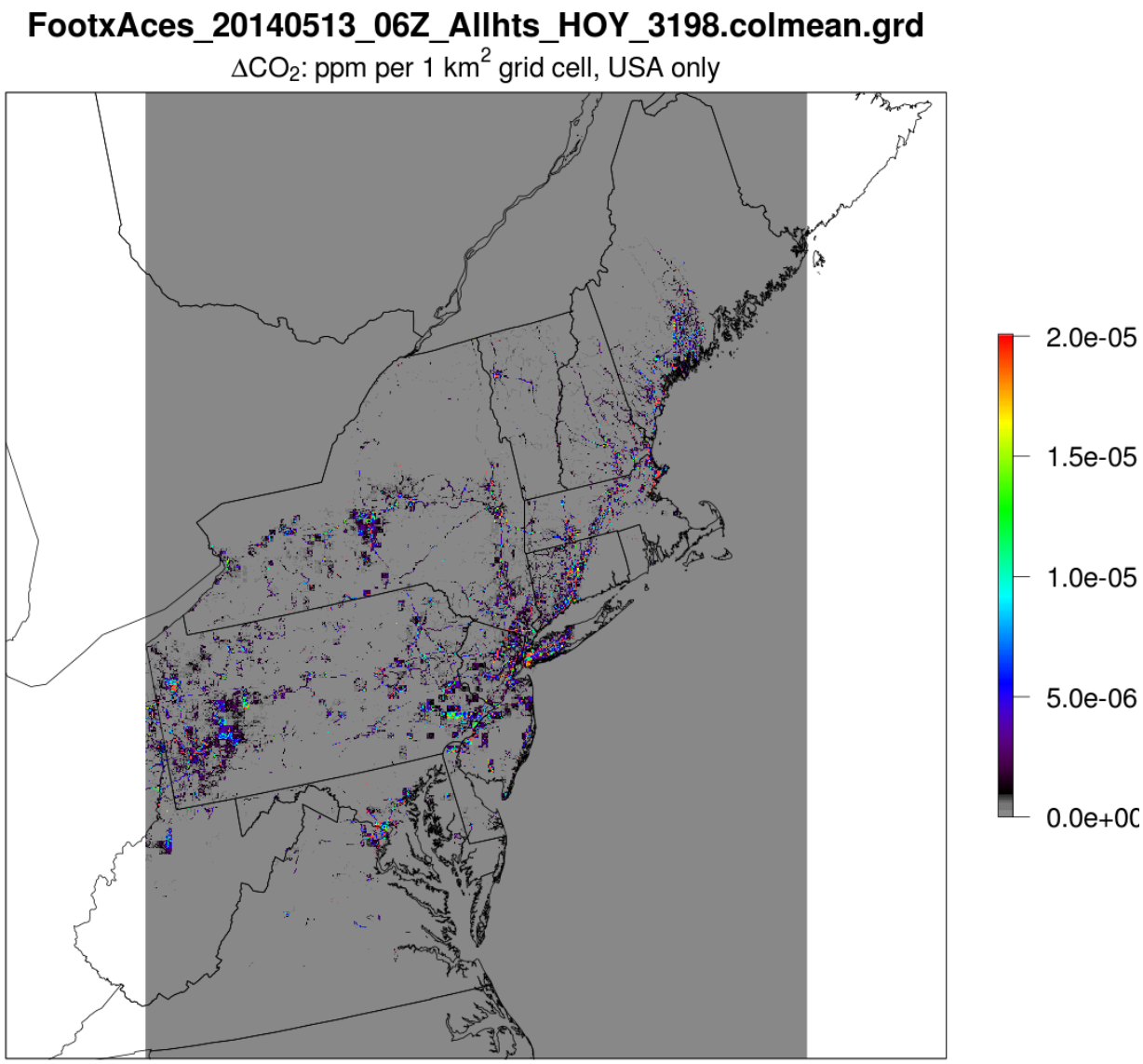

Figure A12. Mean vertical CO_2 enhancements (ppm) from the ACES-STILT convolution for May 13, 2014, 72 hours backwards starting at 6 UTC (within the nocturnal RL).

Summer 2014 ACES-STILT Atmospheric Column Average of CO_2 Enhancements (ppm) by State in Northeastern U.S.

ACES –STILT 72 hours backwards in time starting at 6UTC

Date	NRB	MA	ME	VT	NH	NY	PA	MD	VA	WV	DE	CT	RI	NJ	DC
Jul 1	>0.3	8.03e-02	0.00	2.64e-05	1.74e-05	3.20e-01	3.81e-01	4.58e-02	1.01e-01	5.68e-02	7.22e-03	1.27e-01	5.53e-03	1.26e-01	8.12e-03
Jul 2	>0.3	4.84e-02	0.00	0.00	0.00	6.07e-02	1.97e-01	1.04e-01	1.13e-01	6.81e-03	2.69e-02	2.40e-02	3.70e-02	1.89e-01	4.09e-03
Jul 17	>0.3	7.84e-02	0.00	7.03e-03	1.02e-02	3.66e-01	1.40e-01	4.93e-03	4.20e-03	3.13e-03	9.58e-03	1.12e-01	9.40e-04	2.17e-01	6.82e-05
Jul 18	>0.3	5.47e-03	0.00	4.10e-03	4.45e-03	2.20e-01	2.84e-04	0.00	0.00	0.00	0.00	3.92e-09	0.00	0.00	0.00
Jul 22	>0.3	4.26e-01	4.99e-05	1.13e-02	1.21e-02	2.42e-01	1.03e-01	1.45e-02	3.4e-02	1.24e-02	3.83e-03	4.12e-01	8.88e-02	4.29e-02	1.08e-03
Jul 23	>0.3	8.92e-02	0.00	0.00	6.53e-09	3.06e-01	3.70e-01	1.94e-01	1.11e-01	2.37e-02	1.62e-02	1.49e-01	1.00e-02	1.75e-01	4.00e-03
Jul 24	>0.3	2.68e-01	0.00	1.10e-02	4.56e-03	9.85e-02	1.95e-01	4.84e-05	3.95e-03	4.93e-02	2.00e-05	1.97e-02	9.06e-07	2.31e-03	5.34e-05
Jul 25	>0.3	4.69e-02	1.29e-07	3.09e-02	6.41e-02	1.88e-03	0.00	0.00	0.00	0.00	4.29e-04	0.00	0.00	0.00	0.00
Jul 26	>0.3	6.00e-02	1.13e-04	7.93e-04	1.12e-03	3.96e-01	2.97e-06	0.00	0.00	0.00	0.00	6.32e-02	4.91e-04	3.92e-03	0.00
Jul 27	>0.3	1.51e-02	0.00	5.29e-07	0.00	2.55e-01	4.50e-01	5.83e-02	6.74e-02	4.48e-02	2.70e-02	5.43e-02	1.28e-02	1.65e-01	2.00e-03

Table A2. Summer 2014 transboundary air pollution episodes detected with lidar NRB > 0.3, for the month of July, with CO_2 enhancement influence at the Boston sampling location by State.

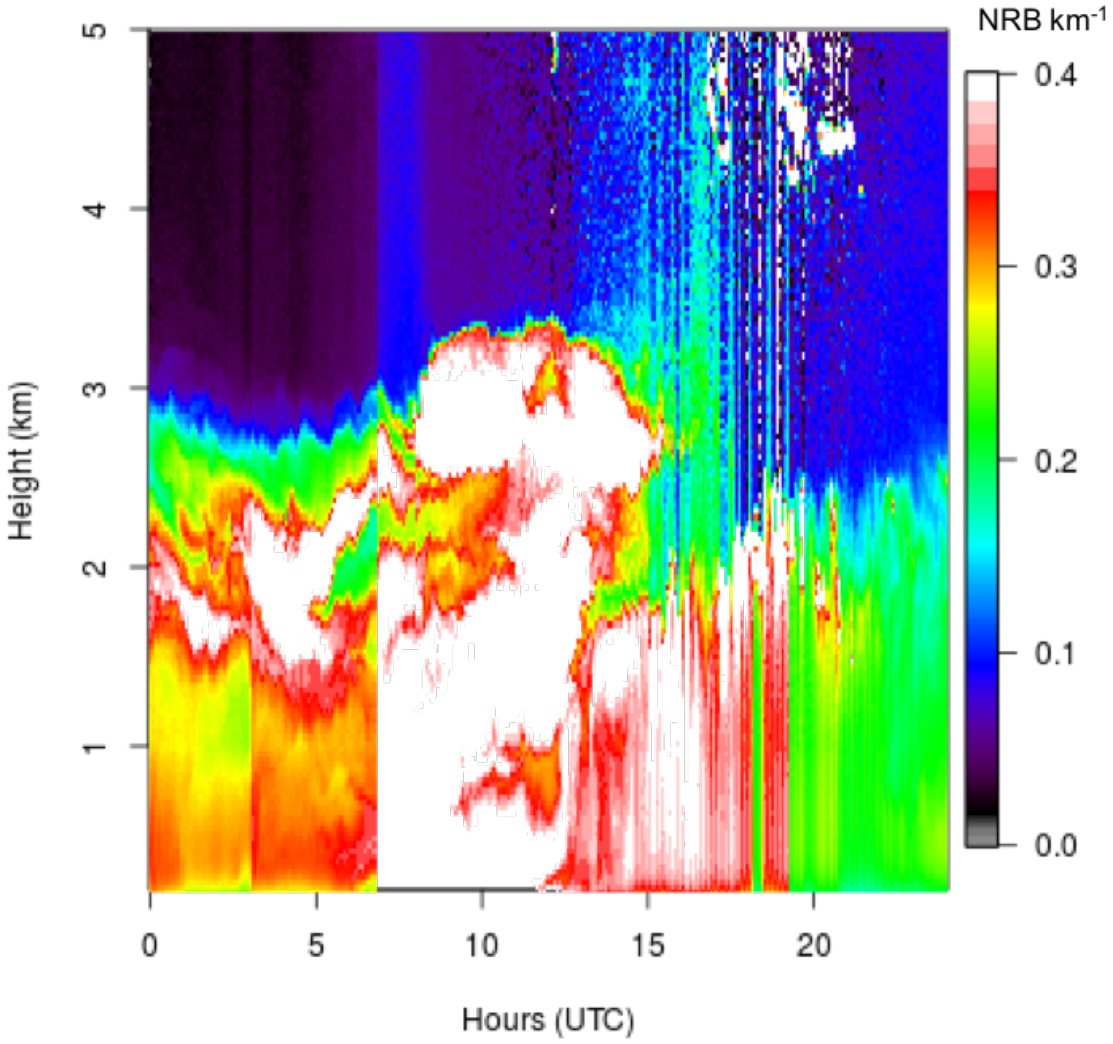

Figure A13. Large lidar NRB enhancements (> 0.3) detected in nocturnal RL (6 UTC) in Boston on July 26, 2014.

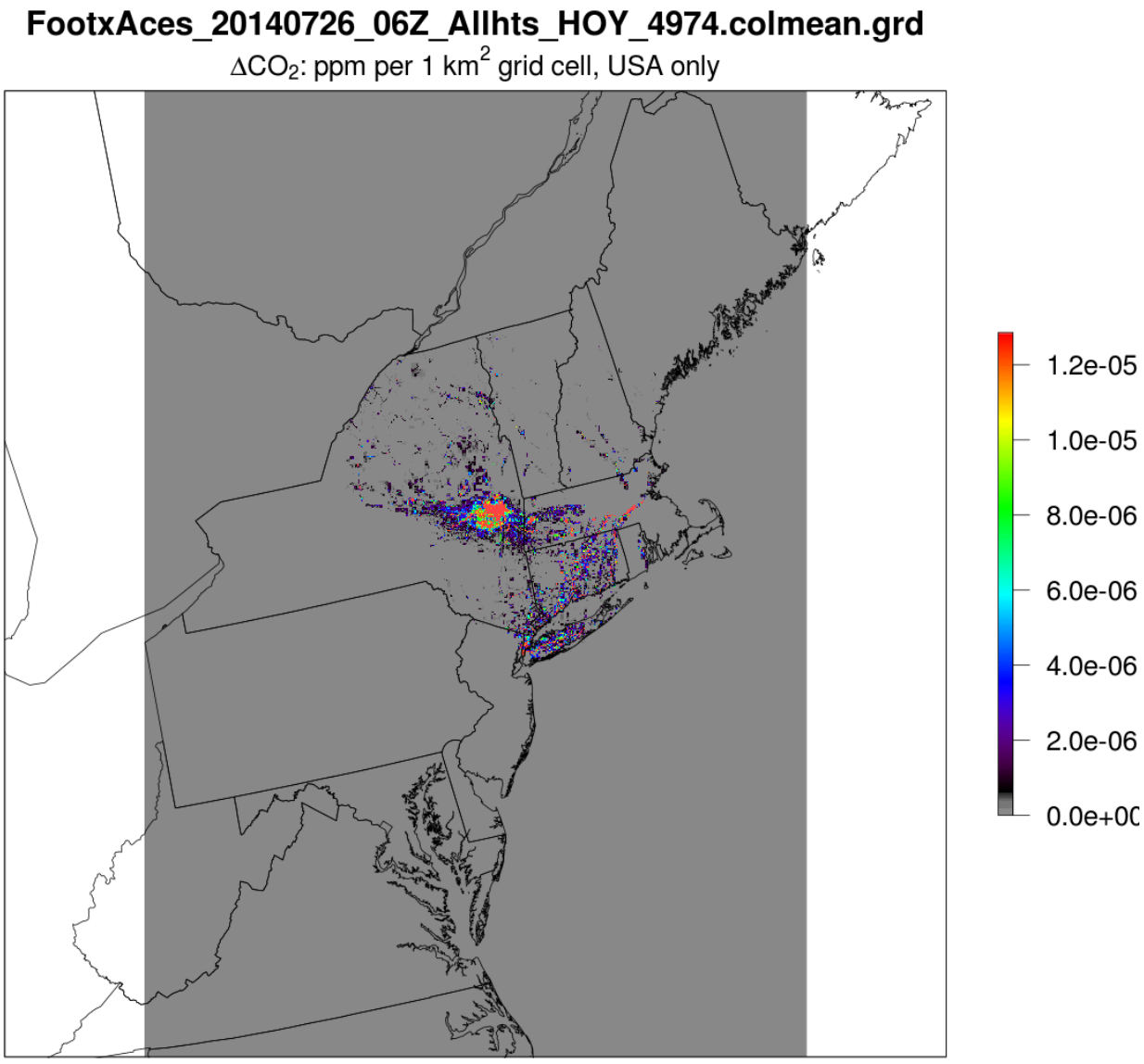

Figure A14. Mean vertical CO_2 enhancements (ppm) from the ACES-STILT convolution for July 26, 2014, 72 hours backwards starting at 6 UTC (within the nocturnal RL).

Fall 2014 ACES-STILT Atmospheric Column Average of CO_2 Enhancements (ppm) by State in Northeastern U.S.

ACES –STILT 72 hours backwards in time starting at 6UTC

Date	NRB	MA	ME	VT	NH	NY	PA	MD	VA	WV	DE	CT	RI	NJ	DC
Sep 8	>0.3	3.51e-01	4.73e-03	2.14e-02	5.10e-02	8.40e-03	0.00	0.00	0.00	0.00	0.00	0.00	0.00	0.00	0.00
Sep 12	>0.3	5.62e-02	1.97e-06	7.61e-03	2.00e-02	5.15e-02	7.225e-02	6.63e-03	1.006e-03	1.611e-02	9.28e-04	6.72e-03	5.71e-03	2.57e-02	1.92e-05
Sep 15	>0.3	2.70e-01	3.19e-06	1.87e-02	4.68e-02	1.64e-02	8.18e-04	0.00	3.82e-05	7.46e-05	0.00	3.39e-02	7.31e-02	0.00	0.00
Sep 17	>0.3	1.37e-02	0.00	7.38e-03	6.33e-02	6.64e-04	0.00	0.00	0.00	0.00	0.00	0.00	0.00	0.00	0.00
Sep 18	>0.3	2.96e-02	0.00	1.58e-03	8.98e-03	3.05e-01	2.63e-02	0.00	0.00	0.00	0.00	9.31e-03	4.61e-04	0.00	0.00
Sep 19	>0.3	7.75e-02	2.28e-02	3.19e-03	4.68e-02	9.00e-03	0.00	0.00	0.00	0.00	0.00	0.00	0.00	0.00	0.00
Sep 22	>0.3	8.22e-02	0.00	0.00	0.00	2.32e-01	3.47e-01	1.29e-01	7.75e-02	1.55e-02	8.99e-02	1.41e-01	3.7e-03	3.49e-01	3.16e-03
Sep 23	>0.3	3.9e-03	0.00	9.83e-03	3.50e-03	7.68e-03	0.00	0.00	0.00	0.00	0.00	0.00	0.00	0.00	0.00
Sep 24	>0.3	0.00	5.53e-06	5.20e-03	3.86e-03	6.17e-03	0.00	0.00	0.00	0.00	0.00	0.00	0.00	0.00	0.00
Nov 8	>0.3	3.95e-02	0.00	1.66e-02	9.50e-03	7.30e-03	0.00	0.00	0.00	0.00	0.00	0.00	0.00	0.00	0.00
Nov 9	>0.3	1.50e-02	0.00	0.00	0.00	1.52e-01	2.49e-01	2.32e-01	2.13e-01	5.11e-02	4.09e-02	5.70e-02	1.27e-02	1.94e-01	7.17e-02
Nov 15	>0.3	0.00	0.00	2.22e-02	6.66e-03	8.81e-03	0.00	0.00	0.00	0.00	0.00	0.00	0.00	0.00	0.00
Nov 19	>0.3	1.82e-01	0.00	0.00	0.00	2.83e-02	7.83e-02	0.00	0.00	1.90e-04	0.00	1.95e-02	0.00	5.18e-05	0.00
Nov 20	>0.3	1.67e-02	0.00	0.00	0.00	2.00e-01	4.78e-02	7.48e-02	1.03e-02	4.65e-02	1.61e-02	1.55e-01	1.12e-03	1.08e-01	9.07e-03
Nov 21	>0.3	2.11e-01	0.00	0.00	0.00	6.09e-02	9.03e-02	0.00	0.00	2.26e-04	0.00	4.21e-03	0.00	1.25e-06	0.00
Nov 22	>0.3	6.90e-02	0.00	4.16e-03	1.76e-03	2.16e-02	7.03e-04	0.00	0.00	3.19e-07	0.00	0.00	0.00	0.00	0.00
Nov 23	>0.3	9.63e-02	0.00	0.00	0.00	2.11e-01	3.28e-01	1.25e-01	1.61e-01	4.88e-02	1.61e-02	1.51e-01	1.00e-02	2.24e-01	8.39e-03
Nov 24	>0.3	4.62e-03	0.00	0.00	0.00	5.99e-02	4.66e-03	3.36e-02	9.40e-02	7.86e-03	1.63e-02	4.12e-02	1.11e-01	4.02e-02	1.07e-03
Nov 21	>0.3	3.50e-02	0.00	0.00	0.00	1.60e-02	2.8e-02	2.22e-02	5.05e-02	4.03e-03	1.20e-02	6.20e-02	4.82e-03	1.23e-01	6.11e-04
Nov 29	>0.3	3.21e-03	0.00	9.79e-03	1.04e-02	7.74e-03	0.00	0.00	0.00	0.00	0.00	0.00	0.00	0.00	0.00

Table A3. Fall 2014 transboundary air pollution episodes detected with lidar NRB > 0.3, with CO_2 enhancement influence at the Boston sampling location by State.

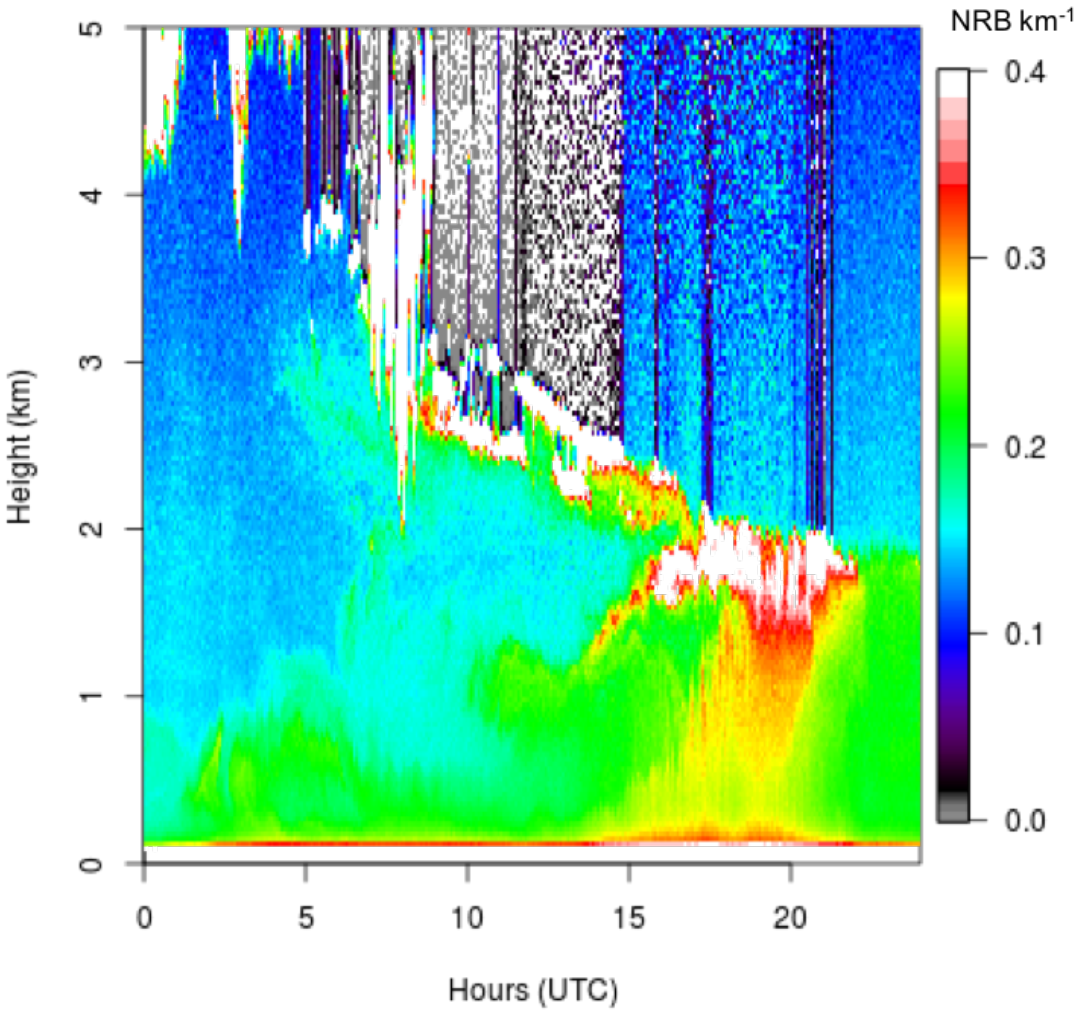

Figure A15. Large lidar NRB enhancements (> 0.3) detected in nocturnal RL (6 UTC) in Boston on November 9, 2014.

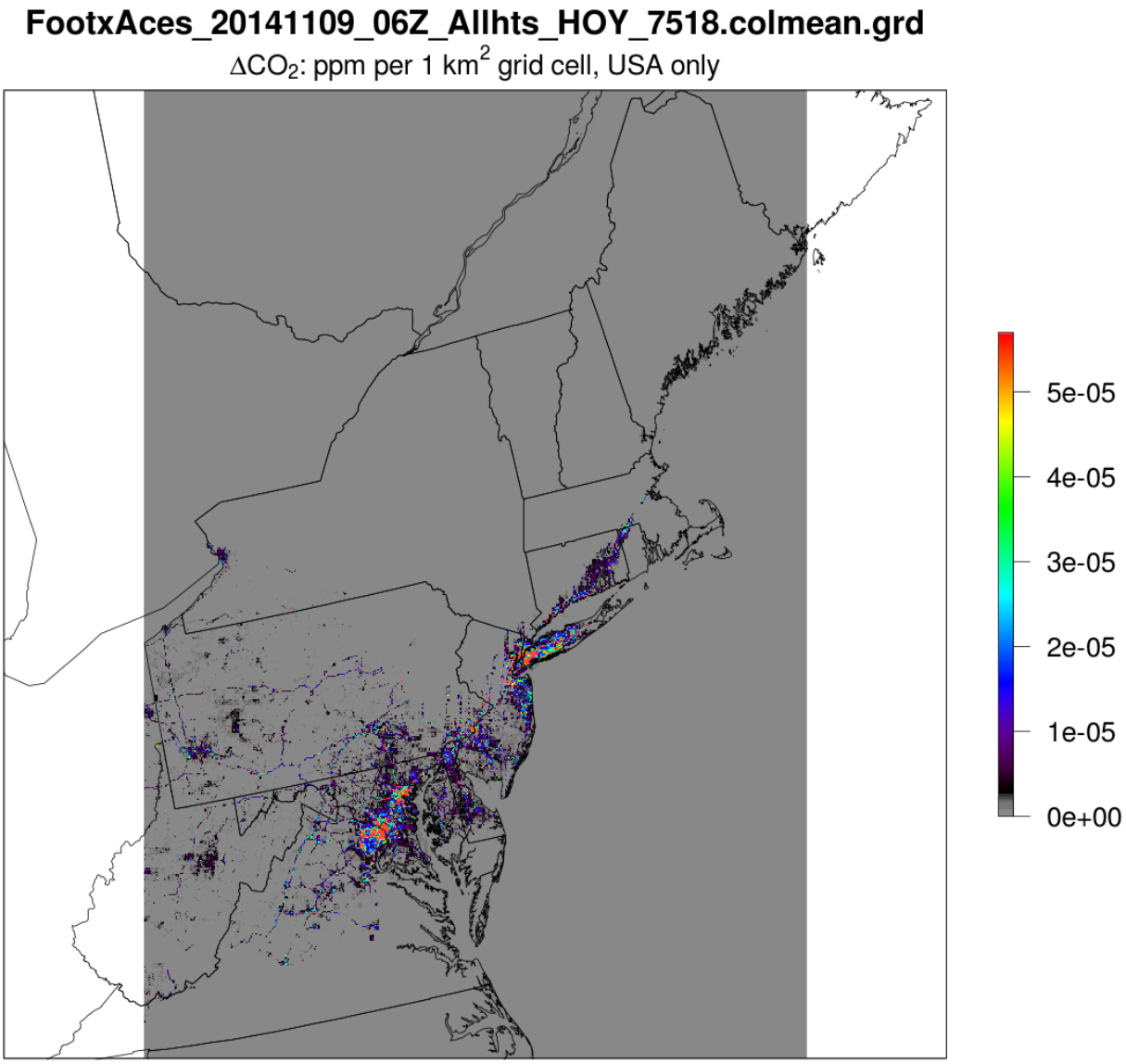

Figure A16. Mean vertical CO_2 enhancements (ppm) from the ACES-STILT convolution for November 9, 2014, 72 hours backwards starting at 6 UTC (within the nocturnal RL).

Page intentionally left blank